INVESTIGATION OF THE DYNAMICAL, MACROPHYSICAL AND RADIATIVE PROPERTIES OF HIGH CLOUDS COMBINING SATELLITE OBSERVATIONS AND CLIMATE MODEL SIMULATIONS

A Dissertation

by

YUE LI

Submitted to the Office of Graduate Studies of
Texas A&M University
in partial fulfillment of the requirements for the degree of

DOCTOR OF PHILOSOPHY

December 2011

Major Subject: Atmospheric Sciences

INVESTIGATION OF THE DYNAMICAL, MACROPHYSICAL AND RADIATIVE PROPERTIES OF HIGH CLOUDS COMBINING SATELLITE OBSERVATIONS AND CLIMATE MODEL SIMULATIONS

A Dissertation

by

YUE LI

Submitted to the Office of Graduate Studies of
Texas A&M University
in partial fulfillment of the requirements for the degree of

DOCTOR OF PHILOSOPHY

Approved by:

Co-Chairs of Committee,	Ping Yang
	Gerald R. North
Committee Members,	Shaima L. Nasiri
	Faming Liang
	Andrew Dessler
Head of Department,	Kenneth Bowman

December 2011

Major Subject: Atmospheric Sciences

ABSTRACT

Investigation of the Dynamical, Macrophysical and Radiative Properties of High Clouds Combining Satellite Observations and Climate Model Simulations. (December 2011)

Yue Li, B.S., Nanjing University; M.S., Stony Brook University

Co-Chairs of Advisory Committee: Dr. Ping Yang
Dr. Gerald R. North

This dissertation investigates three topics concerning high clouds: 1) convectively coupled equatorial wave (CCEW) signals derived from cloud top temperature (CTT) and cirrus optical thickness retrieved from satellite observations; 2) investigation of the physical mechanism governing the fixed anvil temperature (FAT) hypothesis and test of FAT hypothesis with CTT measurements; and 3) the intercomparison of cloud fraction and radiative effects between satellite-based observations and reanalysis product and simulations from general circulation models (GCMs).

A wealth of information on CCEWs is derived from Aqua/MODIS cloud-top properties. We apply space-time spectral analysis on more than 6 years of CTT and isolate various modes of CCEWs including Kelvin, $n = 1$ equatorial Rossby, mixed Rossby-gravity, $n = 0$ eastward inertio-gravity waves, and the Madden-Julian oscillation. The successful application of the same method to cirrus cloud optical thickness confirms robust convective signals at upper troposphere.

Consistent with the physical governing mechanism of the FAT hypothesis, the peak clear-sky diabatic subsidence, convergence and cloud fraction are located at roughly the

same level (200 hPa), which is fundamentally determined by the rapid decrease of water vapor concentration above this level. The geographical maxima of cloud fraction agree well with that of water vapor, clear-sky cooling rates, diabatic subsidence and convergence at 200 hPa. An analysis of the response of the tropical mean CTT anomaly time series to sea surface temperature indicates that a possible negative relationship is present. In addition, we suggest interpreting the FAT hypothesis, and the more recent proportionately higher anvil temperature (PHAT) hypothesis, by using the temperature at the maximum cloud detrainment level instead of the CTT.

Simulations of cloud fraction and radiative properties using two versions of the NCAR CAM models indicate that an overall improvement is observed in CAM5 compared to CAM3. However, an apparent bias in CAM5 shortwave (SW) cloud radiative forcing (CRF) simulation is shown in boreal winter southern midlatitude. This bias is primarily due to the underestimation of fraction-weighted SW CRF related to both high and middle top clouds. Additionally, apparent compensation errors are observed in models.

ACKNOWLEDGEMENTS

I am deeply indebted to my advisor, Dr. Ping Yang. This dissertation would not have been possible without his continuous support and inspiration. I benefited a lot from his knowledge, his enthusiasm in research and the many opportunities he provided throughout my studies at Texas A&M University.

I am also grateful to my co-advisor, Dr. Gerald R. North, for his constant encouragement and guidance. I especially thank him for his willingness to spend time discussing my research and sharing his invaluable experience. I wish to thank Drs. Andrew Dessler, Bryan Baum, Shaima Nasiri and Faming Liang, for their support and constructive comments on my research.

I would like to extend my gratitude to my former and current group members and all people who have helped me during my graduate studies, especially Drs. Gang Hong, Shouguo Ding, Zhibo Zhang and Yu Xie. I also thank Bingqi Yi and Yuan Wang for many helpful discussions on research.

Finally, I would like to thank my family for their love and support. This dissertation is dedicated to my love in my life, my wife Qing and our daughter Kaylee.

TABLE OF CONTENTS

CHAPTER Page

LIST OF FIGURES

FIGURE Page

FIGURE Page

FIGURE Page

CHAPTER I

INTRODUCTION

Cloud systems constitute one of the greatest uncertainties in projecting climate changes. Clouds vary in their macrophysical, microphysical, optical, and radiative properties, primarily due to varying altitudes, compositions, areal coverages and thicknesses, hence exerting various impacts on the weather and climate systems. For instance, although both classified as high clouds (ice clouds) in the International Satellite Cloud Climatology Project (ISCCP; Schiffer and Rossow 1983; Rossow and Schiffer 1991, 1999), deep convective clouds and thin cirrus clouds exhibit apparently different properties. In the tropics, deep convective clouds account for the majority of rainfall. By contrast, thin cirrus is generally non-precipitating. In terms of energy budget, deep convective clouds strongly reduce incoming shortwave (SW) radiation and simultaneously block outgoing longwave (LW) radiation (OLR), and the net radiative effect at the top of the atmosphere (TOA) is not significant (Ramanathan et al. 1989; Harrison et al. 1990). For cirrus, the LW trapping effect can overwhelm the SW cooling effect due to its thin optical property, which induces net warming to the earth-atmosphere system (Minnis et al. 1999; Ponater et al. 2002; Meyer et al. 2002). Moreover, these two types of clouds are usually not independent from each other, since convective blowoff forms one of the major sources for generating cirrus.

This dissertation follows the style of *Journal of the Atmospheric Sciences*.

Even though it has been long realized the important roles of high clouds, due to their high altitude and complex structures, there still exist great uncertainties with our understanding of these clouds. High clouds are frequently located in the upper troposphere (above 10 km), and cirrus originating from convective blowoff in the tropics can go up into the lower stratosphere. The high altitude made observations before the satellite era difficult and unreliable. Additionally, due to extremely low temperatures, the particles inside high clouds are generally in the form of ice crystals, which are normally irregular in shape (Heymsfield et al. 1990; Heymsfield et al. 2002; Nasiri et al. 2002; Chepfer et al. 2005). This variability brings great complexities in the computation of ice crystal single scattering properties and introduces additional uncertainties to the radiative transfer calculations involving high clouds (Takano and Liou 1995; Wendisch et al. 2007; Yang and Liou 1998; Yang and Fu 2009).

To facilitate the study of high clouds, ISCCP classifies high clouds based on cloud top height and optical properties:

$$High\ Clouds = Clouds\ (P_c < 440\ hPa) \begin{cases} Cirrus\ (\tau < 3.6) \\ Cirrostratus\ (3.6 < \tau < 23), \\ Deep\ Convection\ (\tau > 23) \end{cases} \tag{1.1}$$

where P_c is cloud top pressure, and τ is optical thickness. This definition has been widely used and in the following context, we will adopt this definition as well.

1.1 Convectively coupled equatorial waves (CCEWs)

Deep convections occur frequently in the tropics. Tropical convection systems are often observed to be coupled with propagating disturbances that move eastward or

westward parallel to the equator. These disturbances, known as the equatorially trapped waves, are usually along the equator or within the intertropical convergence zone (ITCZ). Rigorous mathematical solutions for the equatorially trapped waves first published in the classic paper by Matsuno (1966), who derived the shallow water equations on an equatorial β-plane from the primitive dynamic equations. The solutions to the shallow water equations correspond to dispersion relations of various modes of equatorially trapped wave. However, observational evidence can be traced back to the identification of easterly waves by Dunn (1940) and Riehl (1948). Also in the 1960s, studies conducted using balloon-measured winds uncovered dry (free) wave modes in the lower stratosphere (Yanai and Maruyama 1966; Wallace and Kousky 1968). Subsequent studies using global satellite measurements detected both westward and eastward propagating disturbances along the equator in cloudiness (e.g., Chang 1970; Yanai and Murakami 1970; Wallace and Chang 1972). The Madden-Julian oscillation (MJO; Madden and Julian 1971, 1972) was revealed at about the same time, which was found to consist of an envelop of deep convections and move eastward with periods of 30-90 days. Spectral analysis was then widely used in studies of these waves (Zangvil and Yanai 1980; Takayabu 1994). Wheeler and Kiladis (1999) built on the work of Takayabu (1994) and applied space-time spectral analysis on about 18 years of twice daily satellite-observed OLR data and successfully isolated various components of the equatorially trapped wave modes, including the Kelvin, $n = 1$ equatorial Rossby, mixed Rossby-gravity (MRG), $n = 0$ eastward inertio-gravity (IG), $n = 1$ westward inertio-gravity (WIG), and $n = 2$ WIG waves. These modes are consistent with the dispersion

relations derived from shallow water theory. In addition, the MJO and tropical-depression type disturbances were identified in the spectrum. They also found that equivalent depths of these waves are in the range of 12-50m, shallower than those of dry equatorial waves. Wheeler and Kiladis (1999) explained this with the interaction between convection and dynamics, and named them convectively coupled equatorial waves (CCEWs), to be distinguished from dry waves which move much faster. Similar results were obtained using satellite measured tropical rainfall (Cho et al. 2004). A more recent study conducted by Lin et al. (2006) using eight years of daily precipitation simulated by 14 climate models reported half of the models have robust CCEWs. For a detailed description of the history on the study of equatorially trapped waves and characteristics of various CCEWs, refer to Kiladis et al. (2009).

It is advantageous to use current satellite observations, such as the Moderate Resolution Imaging Spectroradiometer (MODIS), to study CCEWs. Modern satellite retrieval products provide both high-resolution temporal and spatial observations, which enable detailed study on the initiation, development, and decay of CCEWs. And, a wealth of information derived from satellite observations, such as temperature, water vapor, cloud and aerosol properties makes in-depth research on the interactions between CCEWs and other important meteorological parameters possible.

1.2 Cloud feedback and the Fixed Anvil Temperature (FAT) hypothesis

The energy of sunlight concentrates in the SW bands between 0.4 μm and 0.7 μm, which warms the earth surface and the atmosphere. Conversely, the earth surface

radiates away energy primarily in the LW bands. The incoming solar radiation and outgoing infrared radiation are approximately in balance at the TOA. The earth energy budget is altered by the presence of clouds, and the change due to clouds is known as the cloud radiative forcing (CRF). The magnitude of CRF depends on various parameters, such as cloud optical thickness, water path and effective particle size. Clouds change the earth energy budget in different manners in the SW and LW spectrum. The SW CRF is dominated by the reflection of sunlight, which introduces a cooling effect. Conversely, clouds block LW radiation emitted by the earth surface from escaping to space, hence exerting a warming impact (LW CRF). Since the late 1980's, that global averaged CRF has been known to be negative from the Earth Radiation Budget Experiment (ERBE) observations (Ramanathan et al. 1989; Harrison et al. 1990). The mathematical form of CRF is defined as:

$$\begin{aligned} LWCRF &= OLR_{clr} - OLR_{cloudy} \\ SWCRF &= NetSW_{cloudy} - NetSW_{clr} \end{aligned} \tag{1.2}$$

where subscripts *clr* stands for clear-sky, *cloudy* denotes the condition when cloud is present, and *NetSW* is the net incoming SW radiation. The sign convention is that fluxes are positive pointing upward and downward for OLR and *NetSW*, respectively.

Compared to the increase of global radiative forcing with a doubling of CO_2 (about 4 W m^{-2}), much of warming is due to the feedback processes (Randall et al. 2007; Dessler 2010), among which cloud feedback is the most uncertain. The cloud feedback is defined as the change of cloud radiative effect as climate warms. Numerous studies have been done to narrow the uncertainty of cloud feedback (Cess et al. 1990, 1996; Bony et

al. 2004). Soden and Held (2006) estimated cloud feedback in Intergovernmental Panel on Climate Change (IPCC) Fourth Assessment Report (AR4) models and reported a large spread between 0.14 and 1.18 W m^{-2} K^{-1}, caused primarily by the uncertainty of both sign and magnitude of the SW component. Comparatively, the LW cloud feedback across models appears to be systematically positive with smaller spread. Dessler (2010) investigated short-term cloud feedback with satellite observed broadband fluxes at TOA from year 2000 to 2010 and concluded that both LW and SW components are likely to be positive. However, considering the relative short time that satellite observations have been available, there still exist great uncertainties in quantifying cloud feedback. Moreover, observed climate variations in the past decades, primarily controlled by the El Niño-Southern Oscillation (ENSO), are not analogous to a warming climate due to increase of greenhouse gases.

One of the uncertainties in the LW cloud feedback is the variation of cloud temperature as climate warms, which is closely associated with the energy radiating away from the earth-atmosphere system. Hartmann and Larson (2002) proposed the fixed anvil temperature (FAT) hypothesis, which states that, as the climate warms, the tropical convective anvil cloud temperature should remain fixed. Observational evidence to support the FAT hypothesis are found in Xu et al. (2005, 2007) and Eitzen et al. (2009), who analyzed cloud top temperature (CTT) variations related to tropical convective cloud objects with various sizes from the Tropical Rainfall Measuring Mission (TRMM) /Clouds and the Earth's Radiant Energy Systems (CERES) data during the 1998 El Niño event, and concluded that the CTT variations were small as the

sea surface temperature (SST) changes. They also emphasized that large-scale dynamics plays a more important role when cloud objects are grouped as a function of SST. Conversely, Chae and Sherwood (2010) examined the heights of deep convection systems over the West Pacific regions using the Multiangle Imaging Spectroradiometer (MISR) observations and found variations between boreal summer and winter seasons, which indicated a seasonal variation of 5 K in CTT. In contrast to early numerical studies conducted by Tompkins and Craig (1999), who suggested an increase of tropical anvil cloud temperature with SST, simulations conducted by Kuang and Hartmann (2007) utilized a cloud-resolving model (CRM) to test the hypothesis and demonstrated lack of sensitivity of tropical CTT to increase of SST and greenhouse gas concentrations. Kuang and Hartmann (2007) also pointed out that the resolution of the 3D CRM in Tompkins and Craig (1999) was very coarse (~1 km) in the upper troposphere, which may have significant impact on accurately quantifying anvil temperature changes. Taking into account both the important implications and uncertainties related to the hypothesis, observational tests of the FAT hypothesis using high-resolution satellite observations are highly desirable.

1.3 Clouds in satellite observations and GCM simulations

To better quantify the cloud feedback, it is necessary to have a better understanding of cloud properties, including macrophysical, microphysical, optical, and radiative properties. Satellite observations provide an unprecedented opportunity to investigate cloud properties from a global scale. Intercomparison between satellite observations and

GCM estimates is needed to assess the capability of current GCMs on simulating clouds so that predictions for future climate can be made more objectively (Del Genio et al. 1996; Kiehl et al. 1998; Klein and Jakob 1999; Norris and Weaver 2001; Webb et al. 2001; Randall et al. 2003). Additionally, it is known that compensation errors are common in simulating clouds by models (Lin and Zhang 2004; Zhang et al. 2005). Therefore, to extend the comparison to various types of clouds can advance the parameterization of cloud processes and reduce biases in GCMs. Weare et al. (1996) reported that global averages of model high cloudiness in the Atmospheric Model Intercomparison Projects (AMIP I) were twice more than satellite measurements. They attributed the differences to excessive high thin clouds in the models. Weare (2004) evaluated low, middle and high clouds in AMIP II models against satellite observations and showed that most models simulated moderately well the spatial, seasonal and interannual variability of cloud albedo.

The attempt to compare different cloud types is facilitated by the development of cloud simulators, for instance, the ISCCP simulator (Klein and Jakob 1999; Webb et al. 2001). Lin and Zhang (2004) compared ERBE, ISCCP observations and the Community Atmosphere Model, version 2 (CAM2) simulations utilizing the ISCCP simulator and concluded that the model overestimated high thin, high thick, and low thick clouds while it underestimated middle and low clouds. Their study showed that multiple cloud biases compensate to produce reasonable cloud forcing. Zhang et al. (2005) compared simulations from 10 GCMs with satellite observations and reported that the majority of models overestimated high clouds.

1.4 Descriptions of chapters of the dissertation

This dissertation is organized into three major chapters, each devoted to address a particular issue that has been briefly introduced above.

In Chapter II, we present our results identifying CCEWs in MODIS observed cloud top properties. In Chapter III, we will first explore vertical profiles and spatial distributions of clear-sky diabatic heating, convergence, subsidence, and cloud fraction, and then test the FAT hypothesis by investigating the relationship between CTT variations and SST. In Chapter IV, we compare cloud fraction and radiative effects in two generations of the CAM models and evaluate them against MODIS and a reanalysis product. Different types of clouds, in particular high clouds, are studied separately. Potential factors causing the differences will be discussed.

CHAPTER II

EXPLORATION OF THE MODIS CLOUD-TOP PROPERTY PRODUCTS FOR THE INVESTIGATION OF EQUATORIAL WAVE SYSTEM*

2.1 Background

The Moderate Resolution Imaging Spectroradiometer (MODIS) sensors (King et al. 1992, 2003; Platnick et al. 2003) onboard the National Aeronautics and Space Administration (NASA) Earth Observing System (EOS) Terra and Aqua platforms began to collect data in February 2000 and July 2002, respectively. The MODIS instrument has 36 spectral bands with nadir spatial resolutions of 250 m (two bands), 500 m (five bands) and 1000 m (29 bands). MODIS observes the entire earth within approximately two days at a scan rate of 20.3 rpm in the cross-track direction. Several algorithms have been developed to infer cloud properties from MODIS observations (King et al. 1992; Platnick et al. 2003; Minnis et al. 1995, 1998). The recently released MODIS collection 5 (King et al. 2006) level-3 data provide gridded cloud properties on a daily, 8-day and monthly basis at a global 1° longitude by 1° latitude resolution. The intent of this chapter is to illustrate that the MODIS cloud-top retrieval products can be used to detect various equatorial wave signals.

---

*Reprinted with permission from "Exploration of the MODIS cloud-top property products for the investigation of equatorial wave system", by Li, Y., G. R. North, P. Yang, and B. A. Baum, 2010. *J. Appl. Meteor. Climatol.*, 49, 2050-2057.

Tropical convection (TC) systems play an important role in regulating the global hydrological cycle and energy budget. These TC systems are often organized in terms of equatorial waves (Takayabu 1994; Wheeler and Kiladis 1999, hereafter quoted as WK99). Equatorial wave theory begins with separation of the primitive dynamic equations into horizontal shallow water equations and the vertical propagation equation (Matsuno 1966). On an equatorial beta plane, different solutions to the linearized shallow water equations, for a resting basic state, correspond to the dispersion relations for a variety of equatorial waves. Satellite observations provide an unprecedented opportunity to study equatorial waves from a global perspective. Chang (1970) identified westward moving equatorial wave disturbances over tropical oceans from satellite images. Other observational studies reported both westward and eastward propagating disturbances (Yanai and Murakami 1970; Reed and Recker 1971; Wallace and Chang 1972). WK99 conducted space-time spectral analysis on nearly 18 years of outgoing longwave radiation (OLR) data observed by the National Oceanic and Atmospheric Administration (NOAA) polar orbiting satellites and isolated various equatorial wave modes, including the Madden-Julian oscillation (MJO), Kelvin, n = 1 equatorial Rossby (ER), mixed Rossby-Gravity (MRG), and inertio-gravity (IG) waves. It should be emphasized that the MJO mode is not in agreement with any dispersion relation. Cho et al. (2004) applied spectral analysis to the Tropical Rainfall Measuring Mission satellite (TRMM) measured precipitation data and reported similar results. The focus of this chapter is on the analysis of TC systems from cloud-top properties rather than from OLR, which WK99 used as a proxy for clouds. Under clear or partially cloudy

conditions, underlying surfaces may contaminate the cloud signal in OLR. From a remote sensing perspective when clouds are present, the magnitude of OLR is closely related to cloud-top temperature.

By using cloud products from a polar-orbiting imager such as MODIS to investigate various tropical waves, this work can be extended easily to cloud products based on heritage sensors such as the Advanced Very High Resolution Imager (AVHRR; Heidinger and Pavolonis 2009) and the High Resolution Radiometer Sounder (HIRS; Wylie et al. 2005). Cloud products from these two sensors would extend the cloud product series back in time to about 1980.

2.2 Data and methodology

The MODIS-Aqua daily cloud-top temperature (CTT) gridded product is analyzed from mid-July 2002 to early January 2009 between 15°N and 15°S. The CTT is retrieved both day and night, and combined to get a daily average. Low values of CTT usually denote high clouds, which are prevalent over the tropics (Liou 1986; Rossow and Schiffer 1999; Wylie et al. 2005; Dessler and Yang 2003), and the fraction of deep convective clouds is about 15% of the total tropical high clouds (Hong et al. 2007). Cloud-top pressure (CTP) is inferred by the CO_2 slicing technique for clouds at pressures below about 700 hPa (Menzel et al. 2008; Wylie and Menzel 1999), and the CTT is determined subsequently through comparison with gridded profiles from the National Centers for Environmental Prediction (NCEP) Global Data Assimilation System (GDAS) meteorological product (Derber et al. 1991). For low-level clouds, the infrared

window 11-μm channel temperature is used to infer the CTT (Platnick et al. 2003). From the MODIS data, the CTT is not provided under clear-sky conditions, or under conditions when a cloud is below a detectable limit (visible optical thickness of approximately 0.3). However, the spectral analysis requires data continuity with no gaps. One solution is to average over a large area, but spatial resolution would be reduced and averaging cannot eliminate all missing data. In this study, a neighbor filling method is used to estimate the missing data. Measurements within 1˚ latitude/longitude in each direction from the missing data points are examined and the available data averaged to fill the gaps. This process is repeated until all missing points have been filled. As missing data account for only about 2 percent of the selected spatial range and period, this filling procedure is not expected to introduce significant biases in the subsequent studies. We note that the OLR data used in WK99 were also interpolated to remove missing values (Liebmann and Smith 1996).

In addition, the MODIS-Aqua gridded daily cirrus cloud optical thickness is investigated from September 2002 to September 2008. The cirrus clouds are generally located at the top of cloud layers at altitudes above 10 km. The dissipation of tropical deep convective cloud constitutes an important source for thin cirrus (Jensen et al. 1996). The cirrus optical thickness used in this study is inferred from operational MODIS cirrus reflectance based on MODIS band 26 at 1.38-mm (Gao et al. 2004; Meyer et al. 2007). This band is located near a strong water vapor absorption line; the signal tends to attenuate well above the surface in the tropics so that there is no contribution from low-

level water clouds or aerosols. Thus the cirrus optical thickness inferred from this band is useful for spectral analysis of the high clouds.

The WK99 spectral analysis methodology is followed herein with a brief summary of the procedure. The data are divided into successive 96-day segments with 50 overlapping days. Equatorial waves are either symmetric or antisymmetric about the equator. Hence, for each segment, symmetric and antisymmetric components are separately computed with respect to the equator as defined below:

$$\begin{aligned} CTT^{S}(\Phi) &= [CTT(\Phi) + CTT(-\Phi)]/2 \\ CTT^{A}(\Phi) &= [CTT(\Phi) - CTT(-\Phi)]/2 \end{aligned} \tag{2.1}$$

where superscript S stands for symmetric component, A denotes antisymmetric component, and Φ is latitude. Note that the original value is equal to the sum of both components.

Complex Fourier transform is performed in longitude and in time to obtain the wavenumber-frequency spectra of both the components, and the power is averaged over all segments. A background spectrum is computed by averaging the mean symmetric and antisymmetric components, and then by smoothing many times. The spectral peaks are isolated by dividing each raw spectrum with the smoothed background spectrum.

2.3 Results

Fig. 2.1 shows the Hovmöller diagram for the 2005 raw daily CTT averaged between 15°N and 15°S. Cold anomalies are observed in three distinct regions: central Africa (10°E-40°E); the Indian Ocean and the warm pool western Pacific through central

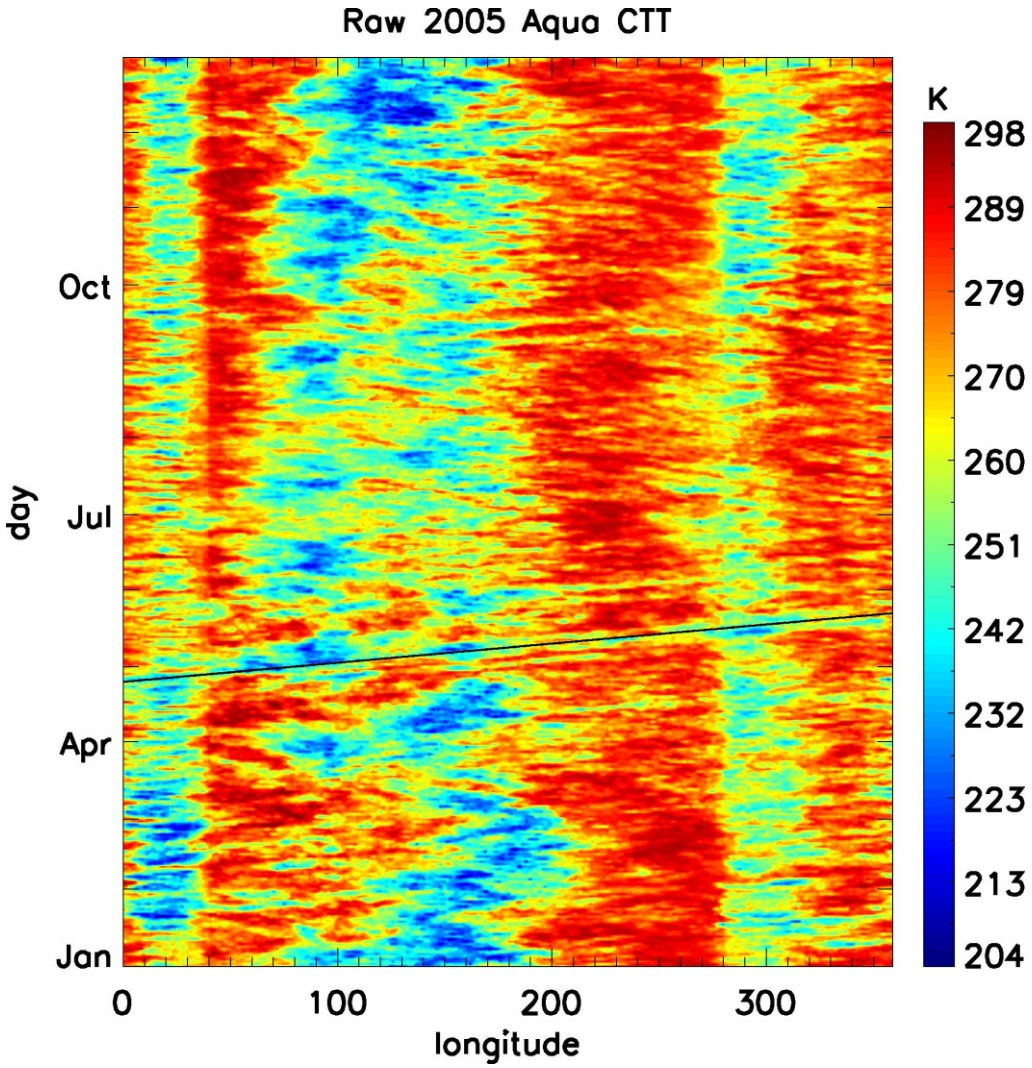

Fig. 2.1 Hovmöller Diagram of raw CTT averaged between 15°N and 15°S of year 2005 from MODIS Aqua data. The thick line corresponds to phase speed 15 m s^{-1}.

Pacific (80°E to 200°E); and South America (280°E to 320°E). High clouds are dominant over these regions (Hong et al. 2007). Cold anomalies over the Indian-Pacific region are stronger during the boreal winter than during the boreal summer. A cluster of convectively coupled Kelvin pulses propagates eastward around the tropics at a speed approximately 15 m s^{-1}, as illustrated by the thick line in Fig. 2.1. Westward moving wave features are also evident, particularly in the Indian-Pacific region. For instance, a cold anomaly originates around 180°E in early January and propagates westward to 140°E. Several oscillating eastward-westward propagating disturbances, indicating a mixture of different types of waves, are observed in this region from January to May.

Further insight is gained through the use of empirical orthogonal function (EOF) analysis, as shown in Fig. 2.2, which decomposes the space-time field into a space component and a time component. Since the extended EOF (EEOF) analysis incorporates time-lagged information, it is useful for studying wave generation and propagation (Weare and Nasstrom 1982; Hannachi et al. 2007; Roundy and Schreck 2009). A longitude-lag-day cross section of EEOF 5 of the CTT averaged between 5°N and 5°S is presented in Fig. 2.2(a). Except EEOF 1, other leading EEOFs have similar patterns, but we chose EEOF 5 because it has the most pronounced trend. Seasonal cycles are first calculated by averaging over the years. Subsequently, anomalies are obtained by subtracting the seasonal cycle, and the EEOF is applied. A clear eastward moving disturbance originates in the Indian Ocean and decays at the dateline with an average phase speed of approximately 7 m s^{-1}. This indicates a MJO signal (Knutson and Weickmann 1987; Madden and Julian 1994). There is also an implication that the MJO

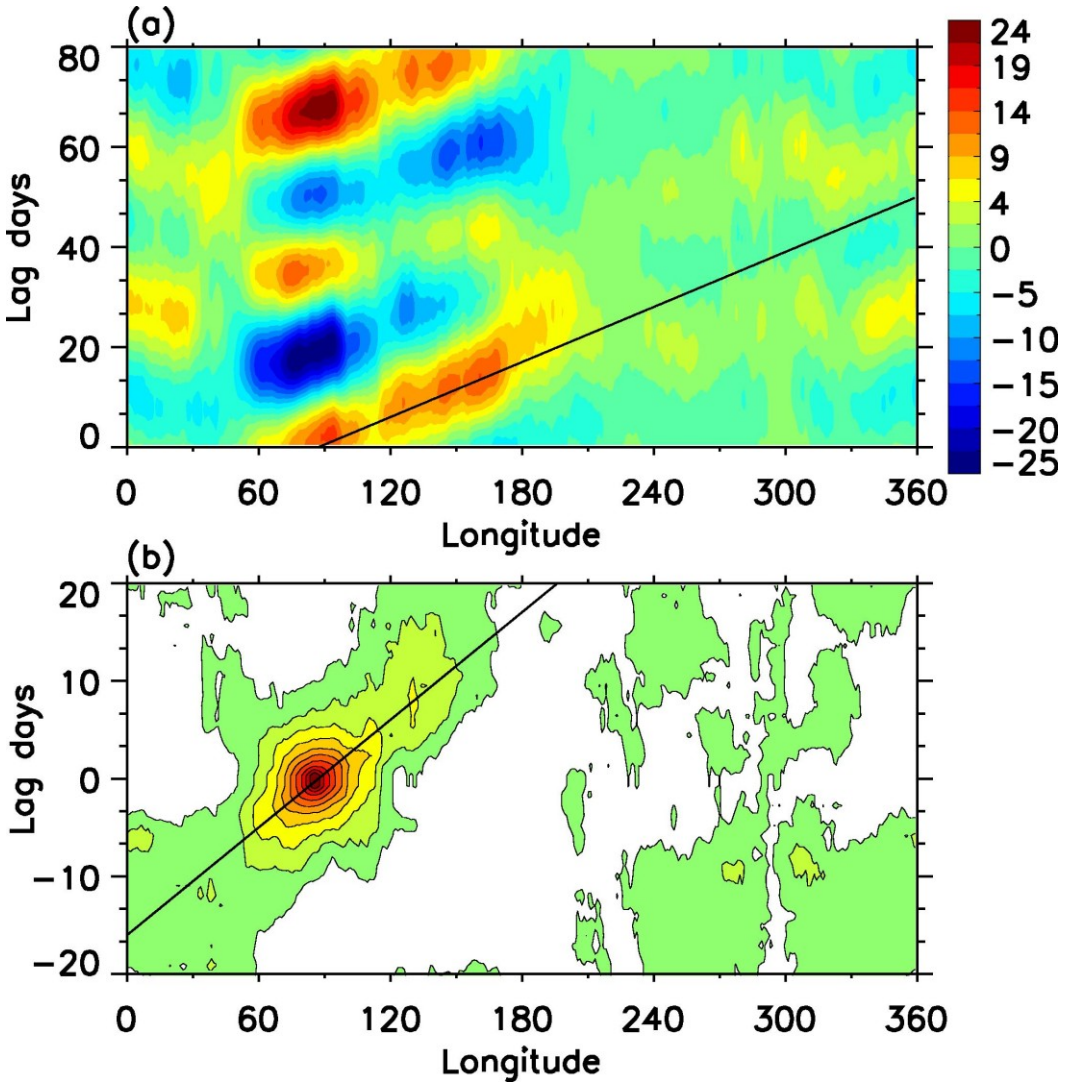

Fig. 2.2 (a) Longitude-lagday cross section of EEOF 5 of CTT averaged between 5°N and 5°S. Units are arbitrary. (b) Lag correlation of the CTT anomaly averaged between 5°N and 5°S with respect to itself at 85°E. Shading starts at 0 and increases an interval of 0.1. The thick line corresponds to phase speed 7 m s^{-1} in each figure.

breaks into two weak waves that continue to propagate eastward after passing the dateline. Lin et al. (2006) used the time lag correlation to track MJO propagation and compared the observations with climate model simulations. Fig. 2.2(b) shows the lag correlation of CTT anomaly averaged between 5°N and 5°S with respect to itself at 85°E. The observation indicates a distinct eastward propagating MJO signal.

Fig. 2.3(a) shows the autocorrelation for CTT averaged over a western Pacific warm pool region (155°E to 165°E, and 15°N to 15°S) as a function of time lag. Autocorrelation for 1200 lag days (approximately half of the data time series) is computed and the values for the first 500 lag days are plotted. A 1-2-1 filter is smoothed 20 times to remove noise, and the value at 0 lag is fixed at 1. In the first few lag days, the autocorrelation decreases quickly to zero due to the weakening of the self-memory effect. A further increase in the lag days increases the autocorrelation, exhibiting an oscillating pattern. This can be explained by the passage of various equatorial waves that cause the fluctuation of cloudiness, inducing the oscillation. The power spectrum of the autocorrelation series reveals many distinct peaks (Fig. 2.3(b)). The most prominent peak corresponds to a period around 360 days and is associated with the annual cycle. The second and third peaks are both located in the 40-80 day period range, consistent with the period of the MJO. The equatorial wave activity is weaker in the eastern Pacific (240°E to 250°E, 15°N to 15°S), Fig. 2.3(c), than in the western Pacific region. The oscillation period is longer and the oscillation magnitudes are smaller than their counterparts in Fig. 2.3(a). The first peak in the power spectrum in Fig. 2.3(d) suggests the annual variation. The most distinct peak corresponds to a period of 125 days and is

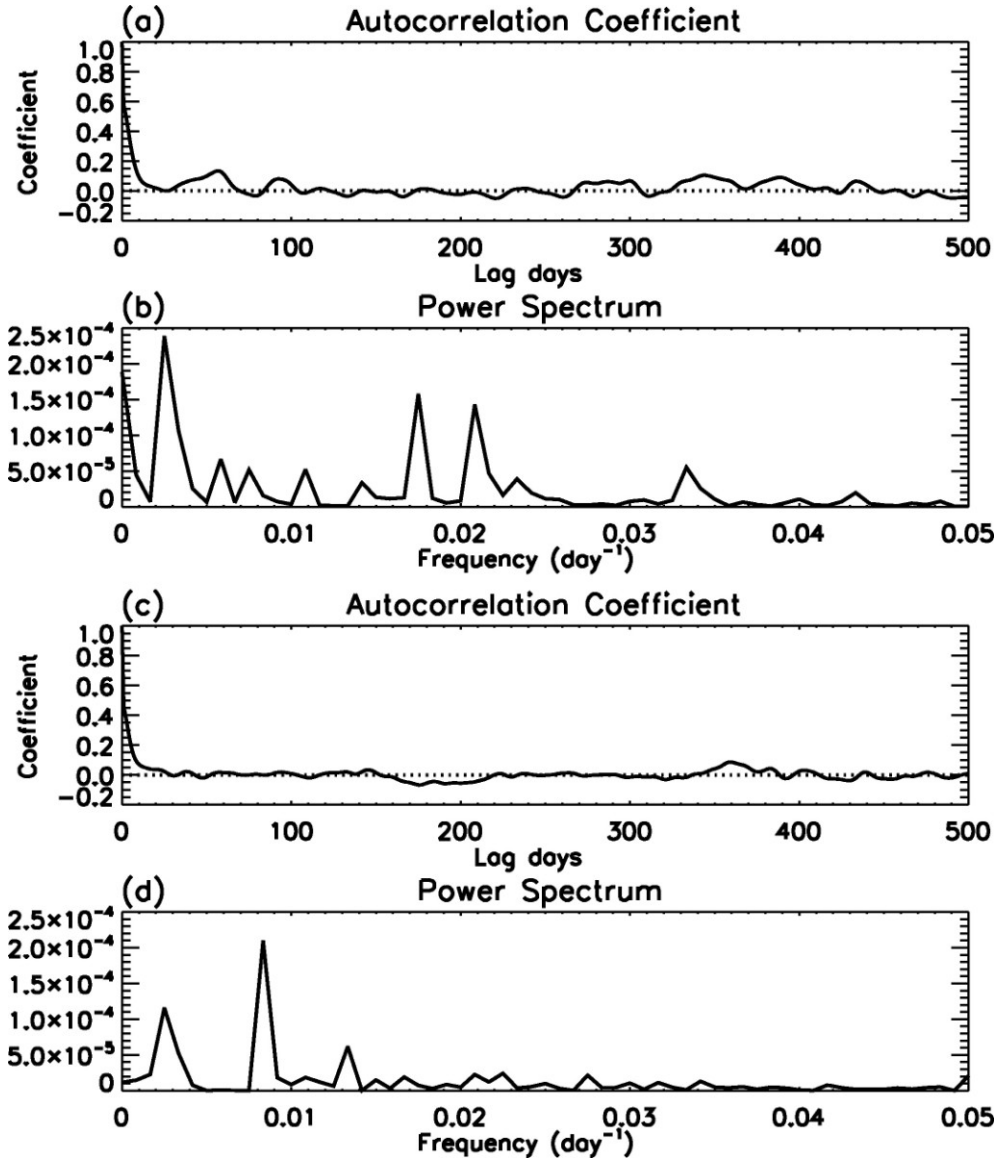

Fig. 2.3 (a) Autocorrelation of CTT averaged over the region 155°E to 165°E, 15°N to 15°S. 1-2-1 smoothing is applied 20 times. The first value is not smoothed. (b) Power spectrum of autocorrelation in (a). Units are arbitrary. (c) Same as (a) but averaged over 240°E to 250°E, 15°N to 15°S. (d) Power spectrum of (c).

likely due to aliases. The spectral peak corresponding to the MJO is not as prominent as in Fig. 2.3(b), indicating the weakening of the MJO signal in the eastern Pacific over the time period of the MODIS data set.

Fig. 2.4 shows the space-time power spectrum of the symmetric and antisymmetric components. The contours are the logarithm of the power summed over 15°N to 15°S. Since each data length for spectral analysis is 96 days, frequencies less than 1/96 cycles per day (cpd) are not plotted. An erroneous peak is detected around negative wavenumber 14, a period of 2.3 days in both the components. This may be associated with the number of swaths that MODIS-Aqua observes each day, similar to the erroneous peaks pointed out in WK99. Successive peaks along the belt of about a 2.3-day period are also spurious and possibly related to the satellite orbit. In the computation of the background spectrum and isolation of spectral peaks discussed later, the negative wavenumber 14 peak will be removed but the remaining 2.3-day belt will be kept. Some prominent features can be identified, especially for the symmetric component. One distinct feature is the dominance of a spectral peak in eastward wavenumber 1-4 at low frequencies over the westward component that is related to the strong eastward propagating MJO (Zhang 2005; Lin et al. 2006). Other strong spectral peaks, namely the "ridges" of individual curves, can be identified visually, particularly Kelvin, n = 1 ER, MRG, and n = 0 eastward IG (EIG) wave dispersion curves, and are more clearly shown in Fig. 2.5.

Various equatorial wave modes are obtained by dividing the mean symmetric and antisymmetric components to the background spectrum, respectively (Fig. 2.5). The

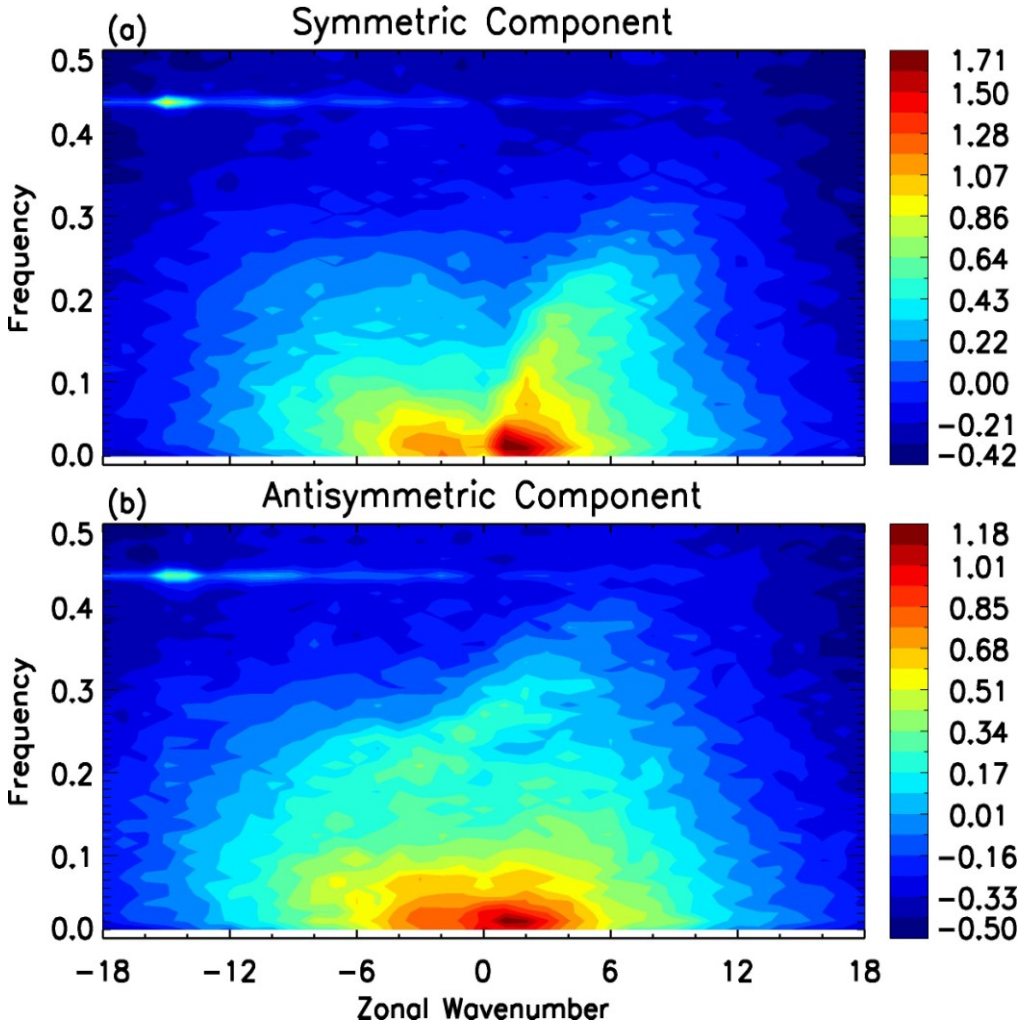

Fig. 2.4 Zonal wavenumber-frequency power spectrums of the (a) symmetric and (b) antisymmetric components of MODIS Aqua CTT. For each component, the power is summed over 15°N-15°S, and the base-10 logarithm is taken.

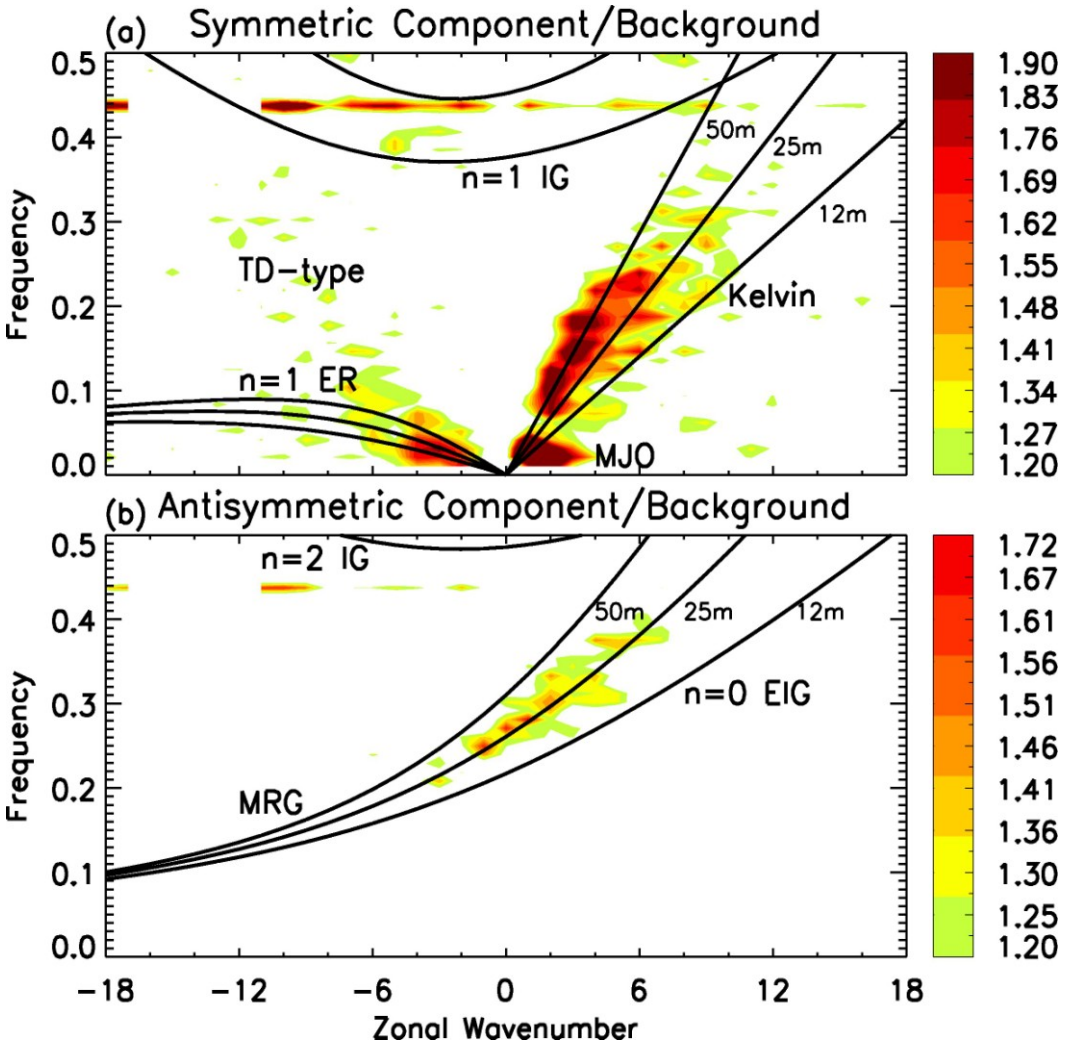

Fig. 2.5 (a) The mean symmetric and (b) antisymmetric component power spectrum divided by the background spectrum. The background power is smoothed by a 1-2-1 filter many times. An erroneous peak near negative wavenumber 14 is not plotted.

background spectrum is obtained by averaging the mean symmetric and antisymmetric parts and both wavenumber and frequency are smoothed numerous times with a 1-2-1 filter. The number of smoothing times in wavenumber is 5 at frequencies less than 0.1 and 40 at frequencies larger than 0.4 increasing in two different steps, whereas it is applied 10 times throughout in the frequency spectrum. Superimposed curves correspond to dispersion relations of various equatorial waves with motionless basic state and three equivalent thicknesses 12 m, 25 m and 50 m. In WK99, ratios larger than 1.1 are considered statistically significant. As the span of data in this study is shorter, 1.2 is adopted as the significance threshold. Consistent with WK99, 25 m is the optimal equivalent thickness. The phase speed of this equivalent depth is slower than that of the free waves in the equatorial stratosphere, and WK99 explained this in terms of the interaction between convection and dynamics. The exception is the equatorial Kelvin wave, where the spectral peaks are seen along the equivalent depth of 50 m for wavenumber 1-4. However, with increasing wavenumber, the equivalent depth of 25 m appears to be a better match. This phenomenon is also observed in WK99. Kelvin, $n = 1$ ER, MRG, and $n = 0$ EIG waves clearly stand out above the background. The MJO signal of eastward wavenumber 1-4, period 30-100 days, is well separated from the Kelvin wave in the symmetric component.

Also of interest is a wave associated with tropical depressions (TD) that may be observed in the westward wavenumber of the symmetric component. The TD-type waves, also known as easterly waves, are important in the genesis and formation of tropical cyclones (Dunn 1940; Riehl 1948). Weak $n = 1$ IG waves are present in the

symmetric component. However, it should be emphasized that the signals along the 2.3-day belt may be contaminated by the satellite orbit instead of indicating the IG signal. This will be explored further in future research with a longer time series of cloud products.

Overshooting tropical convection systems can penetrate to very high altitudes, even above the tropopause, generating cirrus clouds through convective blowoff and indirectly altering the upper-level temperature and moisture fields. This dynamic process links the equatorial waves and high cirrus clouds. Fig. 2.6 shows the power spectrum for various equatorial waves after applying spectral analysis to cirrus optical thickness. Since missing data occupy a much larger portion than in the CTT (about 27.8%), some noise may be expected to be introduced after filling the gaps. Accordingly, the significance threshold is reduced to 1.1. Fig. 2.6 indicates that equatorial wave modes clearly stand out from the background, confirming that convective signals in equatorial regions are pronounced in high cirrus. However, all wave signals, except MJO in the symmetric component, are weaker with respect to the background compared to those in Fig. 2.5. The MJO signal is also observed in the antisymmetric part. Eguchi and Shiotani (2004) examined the tropical upper tropospheric water vapor and cirrus clouds associated with MJO and reported that cirrus clouds are closely related to high humidity and cold anomaly due to the convective center. Fujiwara et al. (2009) investigated the cirrus variations over tropical western Pacific in the tropical tropopause layer using lidar radiosonde data and revealed that equatorial waves play a major role in generating and dissipating cirrus clouds. Our results are consistent with these studies. The relatively

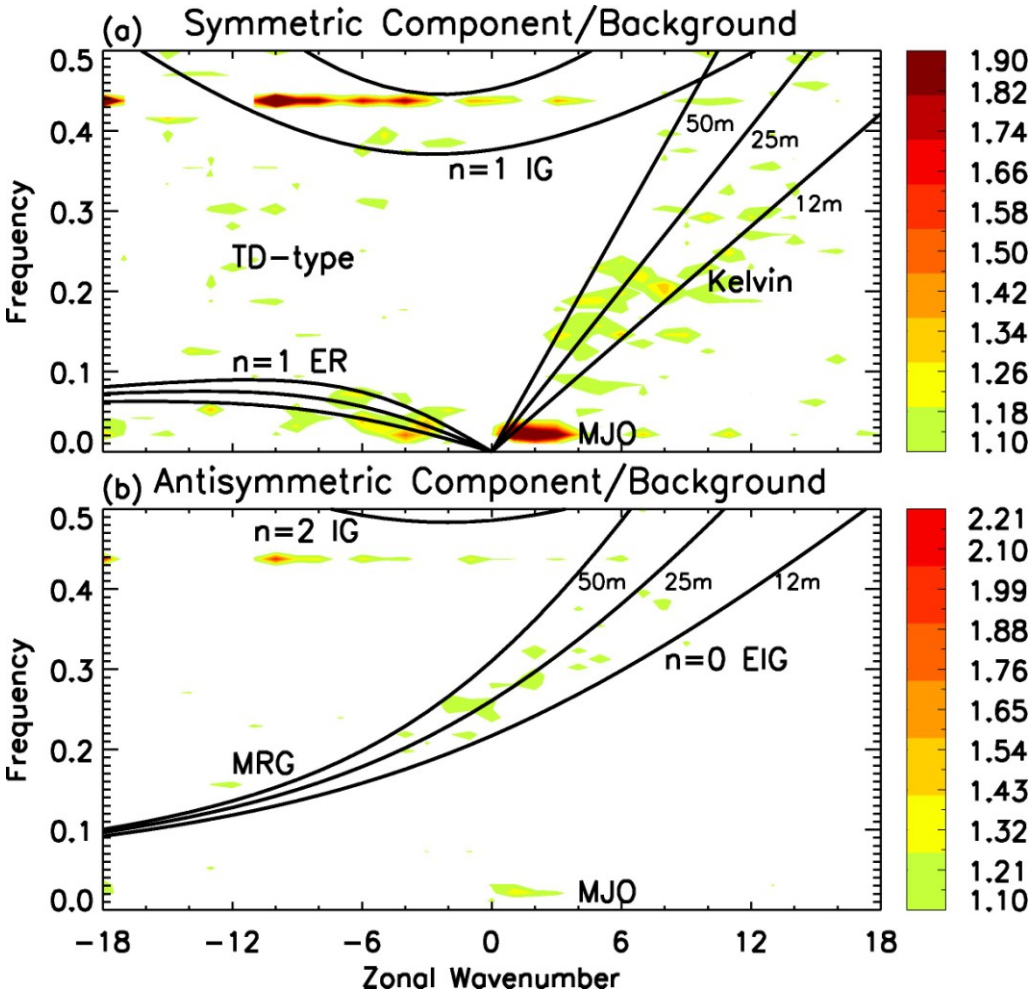

Fig. 2.6 Same as Fig. 2.5 except using cirrus optical depth.

weak signal in the power spectrum suggests that a portion of cirrus may be formed in situ, but this may be due in part to the large portion of missing data.

2.4 Summary and discussion

To illustrate the wealth of information that the MODIS cloud retrieval products provide about atmospheric dynamical phenomena, more than six years of MODIS cloud-top properties from the Aqua platform, specifically cloud-top temperature and cirrus optical thickness, are used to study equatorial wave properties. A space-time spectral analysis is conducted based on the Level 3 daily product. Various equatorial wave modes are identified, such as Kelvin wave, $n = 1$ equatorial Rossby and MRG waves, $n = 0$ EIG and $n = 1$ IG waves, and the MJO waves. Also found are waves associated with tropical depressions. A cluster of convectively coupled Kelvin wave pulses is found to move at a phase speed of approximately 15 m s^{-1} around the globe, whereas the MJO is slower (about 7 m s^{-1}) and more confined to the Indian-Pacific region. Consistent with previous findings, an equivalent depth of 25 m is optimal for these convectively coupled equatorial waves. Perhaps because of spatial gaps in MODIS coverage in the tropics for a single day, some spurious peaks are present, raising the issue that interpretation must be carefully made. Further studies using other MODIS gridded products will be necessary to answer the question. Roundy and Frank (2004) analyzed the daily total column precipitable water (PW) datasets from the NASA Water Vapor Project and demonstrated that a zonal phase shift between the OLR and PW anomalies is related to equatorial waves. The answer to whether or not the equatorial wave signals can be

detected in the MODIS water vapor product may contribute to a better understanding of the interaction of different phenomena inherent in the development and propagation of various equatorial waves. More continuous MODIS observations are needed to study interannual to decadal oscillations of the atmosphere, such as the quasi-biennial oscillation (QBO) (Baldwin et al. 2001). It would also be useful to extend the MODIS analysis to the longer-term decadal cloud products available from the Advanced Very High Resolution Radiometer (AVHRR) (Heidinger and Pavolonis 2009). Our effort demonstrates that MODIS cloud products are valuable in the study of the tropical dynamics of the atmosphere. The use of cloud products rather than OLR as a proxy for cloud cover suggests that more detailed analyses can be explored to take advantage of vertical cloud structures. The study on the relationship between cirrus clouds and equatorial waves is important to understand upper-level cloud behaviors and provides insights to better represent cirrus clouds in climate models. Furthermore, the cloud and water vapor products from MODIS can be used to improve the understanding of the phenomena associated with atmospheric dynamics, with no regional limits, due the high spatial resolution and global coverage provided by various polar-orbiting satellite imagers.

CHAPTER III

TEST OF THE FIXED ANVIL TEMPERATURE HYPOTHESIS

3.1 Background

Deep convection systems occur frequently in tropics. These systems strongly reflect solar radiation, which can induce a cooling effect on the earth; but, on the other hand, the systems can impose a warming effect on the atmosphere by trapping infrared radiation from the earth's surface and emitting to space at the very low temperatures of the high, cold cloud tops. Satellite observations indicate that the signs of these two effects are opposite and strongly cancel each other at the top of the atmosphere (Ramanathan et al. 1989; Harrison et al. 1990). The overall effect on the earth-atmosphere system is that tropical convective systems tend to cool the earth surface and heat the atmosphere.

Hartmann and Larson (2002) proposed that the tropical convective anvil cloud temperature should remain stable during climate change, and the proposal is known as the fixed anvil temperature (FAT) hypothesis. The hypothesis is based on the fact that the clear-sky radiative cooling rate decreases significantly above 200 hPa (Hartmann et al. 2001a) primarily due to a rapid reduction in water vapor, which is the major emitter in the upper troposphere. Since saturation vapor pressure depends only on temperature, known from the Clausius-Clapeyron equation, the decrease of the clear-sky radiative cooling rate is closely associated with air temperature. Mass conservation requires that the rapid decrease in cooling in clear skies must be balanced by subsidence warming through a strong convergence, which implies a strong divergence from nearby cloudy

regions (Folkins and Weinstock 2002; Minschwaner and Dessler 2004). Hence, the suggestion is that the temperature at the detrainment level of tropical convection is fixed.

The FAT hypothesis is interpreted to mean the tropical convective cloud top temperature (CTT) should remain approximately constant as the climate warms (Xu et al. 2005, 2007; Eitzen et al. 2009; Zelinka and Hartmann 2010, hereafter ZH10). The FAT hypothesis has important implications for cloud-climate interactions, in particular, the longwave cloud feedback process (ZH10). However, the hypothesis is still under debate, even though various studies have been conducted by using both satellite observations and numerical simulations (Xu et al. 2005, 2007; Eitzen et al. 2009; Kuang and Hartmann 2007; Chae and Sherwood 2010).

More recently, ZH10 modified the FAT hypothesis and proposed the proportionately higher anvil temperature (PHAT) hypothesis, which takes into account the slight increase of static stability in a warming climate, by analyzing the Intergovernmental Panel on Climate Change Fourth Assessment Report (AR4) model output. PHAT assumes that high cloud temperature follows upper tropospheric convergence-weighted temperature, which best explains the slight increase of high cloud temperature in climate simulations of 21st-century warming.

In this chapter, we show that the FAT hypothesis provides a solid theoretical background to diagnose the peak convective cloud detrainment level using clear-sky energy and mass budget. The maxima in the spatial distributions of upper tropospheric water vapor agree well with that of clear-sky radiative cooling rates, diabatic subsidence, convergence, and cloud fraction at the peak cloud level (roughly 200 hPa). Additionally,

CTT retrievals from the Moderate Resolution Imaging Spectroradiometer (MODIS) are used to investigate the response of convective CTT to SST variations.

3.2. Data

3.2.1. Moderate Resolution Imaging Spectroradiometer (MODIS)

The MODIS-Aqua Collection 5 (King et al. 2006) Level 3 gridded data binned with a resolution of 1° longitude by 1° latitude are used in this study. We use six years of tropical (30°N-30°S) daily mean cloud fraction, cloud optical thickness (τ), cloud top pressure (P_c), and CTT from September 2002 to August 2008. Cloud fraction is derived as the ratio of the number of pixels flagged as cloudy to the total number, and τ is retrieved using a bispectral technique (Nakajima and King, 1990). Pre-computed static lookup libraries (King et al. 1997) are used in conjunction with observations to simultaneously infer τ and cloud effective particle size. As τ is retrieved using reflected solar radiation, only daytime cloud properties are used. P_c is retrieved from a CO_2 slicing technique (Menzel et al. 2008; Wylie and Menzel 1999) utilizing the strong CO_2 absorption features centered at wavelengths near 15 μm. The MODIS instrument observes radiance from spectral bands around 13.3 μm, 13.6 μm, 13.9 μm, and 14.2 μm and the ratios between the different pairs are used to retrieve P_c. CTTs for upper-level clouds are derived by comparing the P_c with meteorological profiles from the National Centers for Environmental Prediction (NCEP) Global Data Assimilation System (GDAS) (Derber et al. 1991). When the P_c is larger than 700 hPa, the brightness temperature at the 11 μm infrared band is used to infer CTT (Platnick et al. 2003).

3.2.2 ECMWF interim reanalysis

The SST data from the European Center for Medium-Range Weather Forecasts (ECMWF) interim reanalysis are available for public use at a 1.5° by 1.5° horizontal resolution and a 6-h interval. We derive daily averages for the same period as the MODIS cloud product, and adopt monthly mean atmospheric profiles of temperature (T), specific humidity (R), and ozone mixing ratio at 37 pressure levels from 1000 hPa to 1 hPa for each horizontal grid including 15 levels at the upper atmosphere between 1 hPa and 200 hPa. For better comparison purposes, MODIS cloud data are interpolated to the same horizontal resolution as data from the ECMWF interim reanalysis.

3.3 Methodology

We follow the same approach as ZH10 and compute vertical profiles and geographical distributions of clear-sky radiative cooling rates (Q_R), diabatic subsidence (ω), and diabatic convergence (*conv*). The clear-sky Q_R is calculated using the Fu-Liou radiative transfer model (Fu and Liou 1992, 1993) with monthly mean atmospheric profiles from December 2002 to August 2008 as input. The same parameters (M. D. Zelinka, personal communication) are used as in ZH10 except we use here a fixed solar zenith angle of 60° to approximate a diurnal mean value for a 12 hour solar day (Liou and Gebhart 1982; Yang et al. 2007).

By assuming that clear-sky diabatic warming is exactly balanced by radiative cooling, one can calculate diabatic subsidence

$$\omega = \frac{Q_R}{\lambda} \quad . \tag{3.1}$$

λ is the static stability and defined as

$$\lambda = \frac{\kappa T}{p} - \frac{\partial T}{\partial p} \quad , \tag{3.2}$$

where $\kappa = R_d / C_p$, R_d is dry air gas constant, C_p is specific heat of air at constant pressure, and p is atmospheric pressure.

According to the mass continuity equation, horizontal convergence *conv* is computed by

$$conv = -\nabla_H \bullet \mathrm{U} = \frac{\partial \omega}{\partial p} \quad . \tag{3.3}$$

In addition, CTT variations related to individual high cloud types for boreal winter and summer are analyzed. Here, boreal winter denotes December from the previous year and January and February (DJF) from the current year, and summer includes June, July, and August (JJA). We separately study the CTT variations for deep convection, thin cirrus, cirrostratus, and all high clouds. Tropical convection is one of the major sources for generating upper-level thin cirrus (Jensen et al. 1996; Li et al. 2010); however, we do not attempt to distinguish cirrus generated by convection from those formed in-situ. Kubar et al. (2007) and Zelinka and Hartmann (2009) suggested that thick anvil clouds detrain from deep convection and have optical thicknesses between 4 and 32. The ISCCP cirrostratus and deep convection categories can reasonably represent thick anvil clouds with the latter cloud type tending to be more associated with convective cores.

To assess the quantitative relationship between convective CTT and SST, a linear regression analysis is performed on the time series of anomalies for all months between September 2002 and August 2008. The standard error σ for the regression slope is used to estimate the uncertainty.

3.4. Results

3.4.1 Clear-sky cooling rates, diabatic subsidence, convergence, and cloud fraction

Fig. 3.1 shows the tropical mean temperature and specific humidity profiles. Tropical temperatures decrease monotonically as pressure decreases up to 100 hPa, but above this altitude an inversion is observed. Specific humidity decreases exponentially with altitude to the cold-point tropopause and stays approximately constant in the displayed pressure range.

Tropical mean profiles of clear-sky shortwave (SW), longwave (LW), and net radiative cooling rates Q_R, calculated by the Fu-Liou model, are shown in Fig. 3.2. The SW warming effect is more robust at low levels, but the magnitude gradually declines with altitude below 100 hPa and then exhibits a sharp increase. Similar to the results reported by Kubar et al. (2007) for individual Pacific basins, the LW Q_R is roughly constant at 2 K day^{-1} up to a pressure of 300 hPa, after which it drops off dramatically and reaches a minimum around 100 hPa, above which carbon dioxide is the predominant emitter. Both SW and LW Q_R between 200 hPa and 700 hPa are dominated by water vapor, but above 200 hPa the water vapor concentration decreases rapidly.

The net Q_R is the combined effect of SW and LW cooling rates and a rapid decrease is seen above 250 hPa. Unlike ZH10, the net clear-sky Q_R at pressure ranges between 700 hPa and 300 hPa are not constant, mainly due to the varying magnitude of SW Q_R with altitude. The lack of agreement is probably caused by using different approaches of treating the solar zenith angle in the radiative transfer calculation.

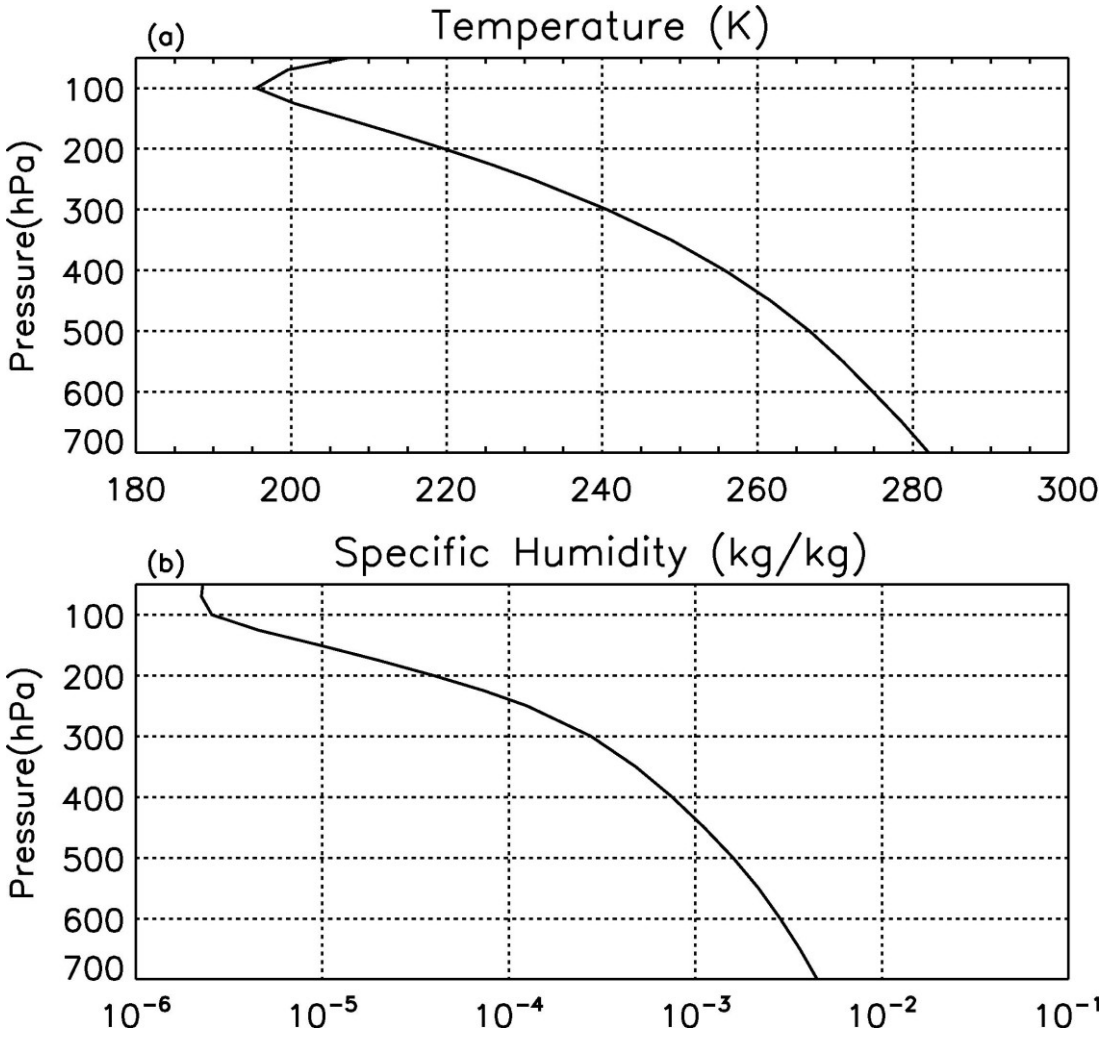

Fig. 3.1 Tropical mean (30ºN-30ºS) (a) temperature and (b) specific humidity profiles from ECMWF interim reanalysis averaged between December 2002 and August 2008.

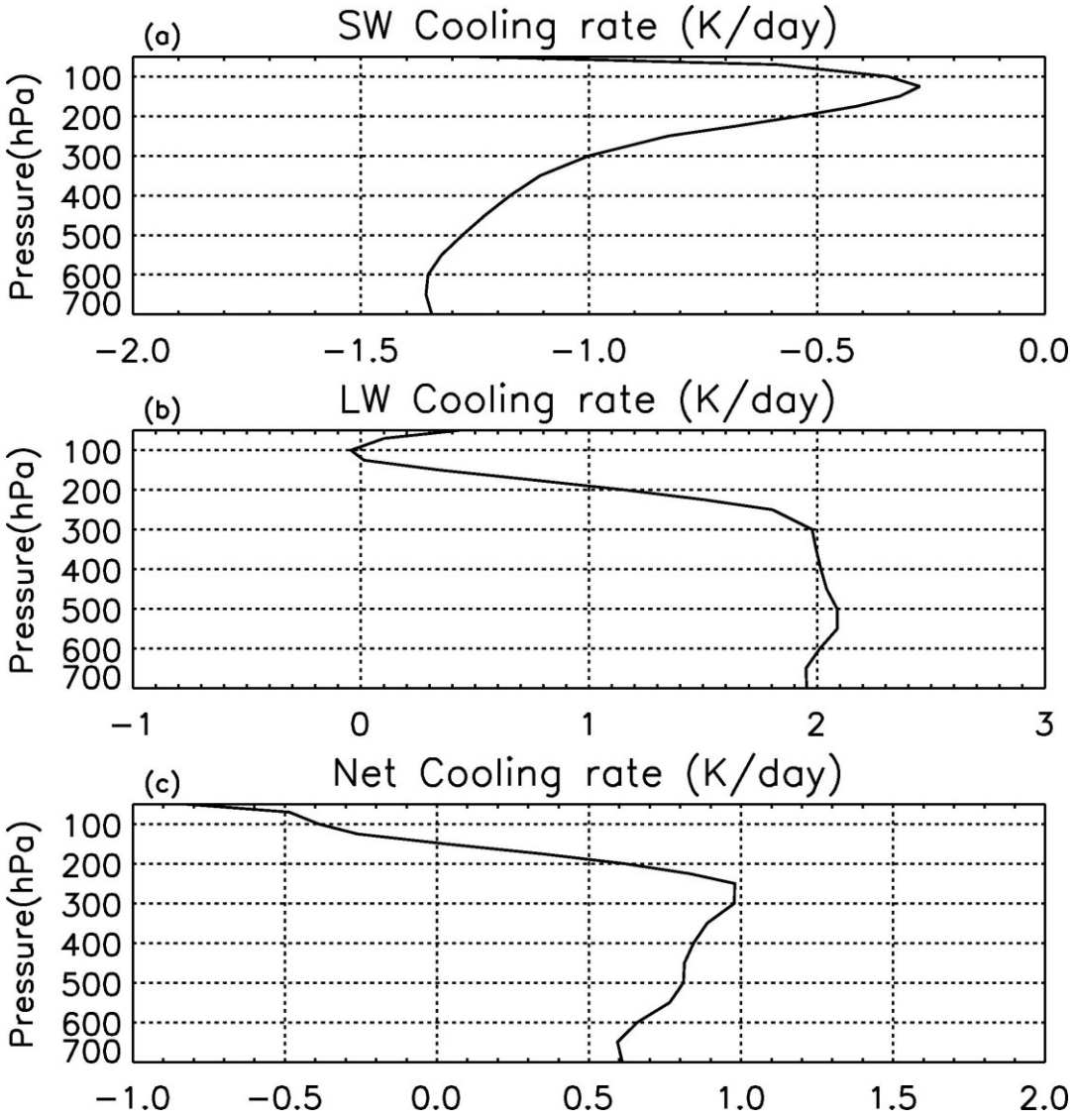

Fig. 3.2 Tropical mean profiles for (a) shortwave (SW), (b) longwave (LW), and (c) net clear-sky radiative cooling rates.

Fig. 3.3a demonstrates that the static stability λ is roughly constant below 300 hPa and increases rapidly above, determined by the competition between the ratio of temperature to pressure and the lapse rate. The diabatic subsidence ω (Fig. 3.3b) computed by equation (3.1) gradually increases with altitude from 600 to 200 hPa. Above ~200 hPa, ω decreases sharply to 0. Overall, downward motion dominates between 700 hPa and 150 hPa. Diabatic convergence *conv* (Fig. 3.3c) exhibits a positive peak slightly above the diabatic ω peak, where the derivative of ω with respect to pressure is greatest. Notice that the varying magnitudes of ω and *conv* at altitudes below 300 hPa are primarily caused by variations in the net Q_R.

In Fig. 3.4 we plot the temporal mean spatial distributions of specific humidity and clear-sky Q_R at 200 hPa, where sharp transitions of physical properties between nearby layers occur. A considerable amount of water vapor (Fig. 3.4a) is observed over central Africa, the tropical Indian and western Pacific Oceans, and tropical South America. The upper troposphere over the tropical eastern Pacific is significantly drier compared to the western Pacific. The geographical distributions of SW, LW, and net Q_R (Fig. 3.4 b-d) agree well with that of specific humidity. Note in Fig. 3.4b, the values are negative, which corresponds to warming.

The distribution of static stability λ (Fig. 3.5a) is roughly zonally homogeneous and fundamentally determined by the temperature distribution. It is observed that λ tends to decrease toward the equator, showing that the tropical atmosphere is less stable compared to higher latitudes at this level. The peaks for clear-sky diabatic ω and *conv* are located around the same regions as specific humidity and Q_R (Fig. 3.5b and c).

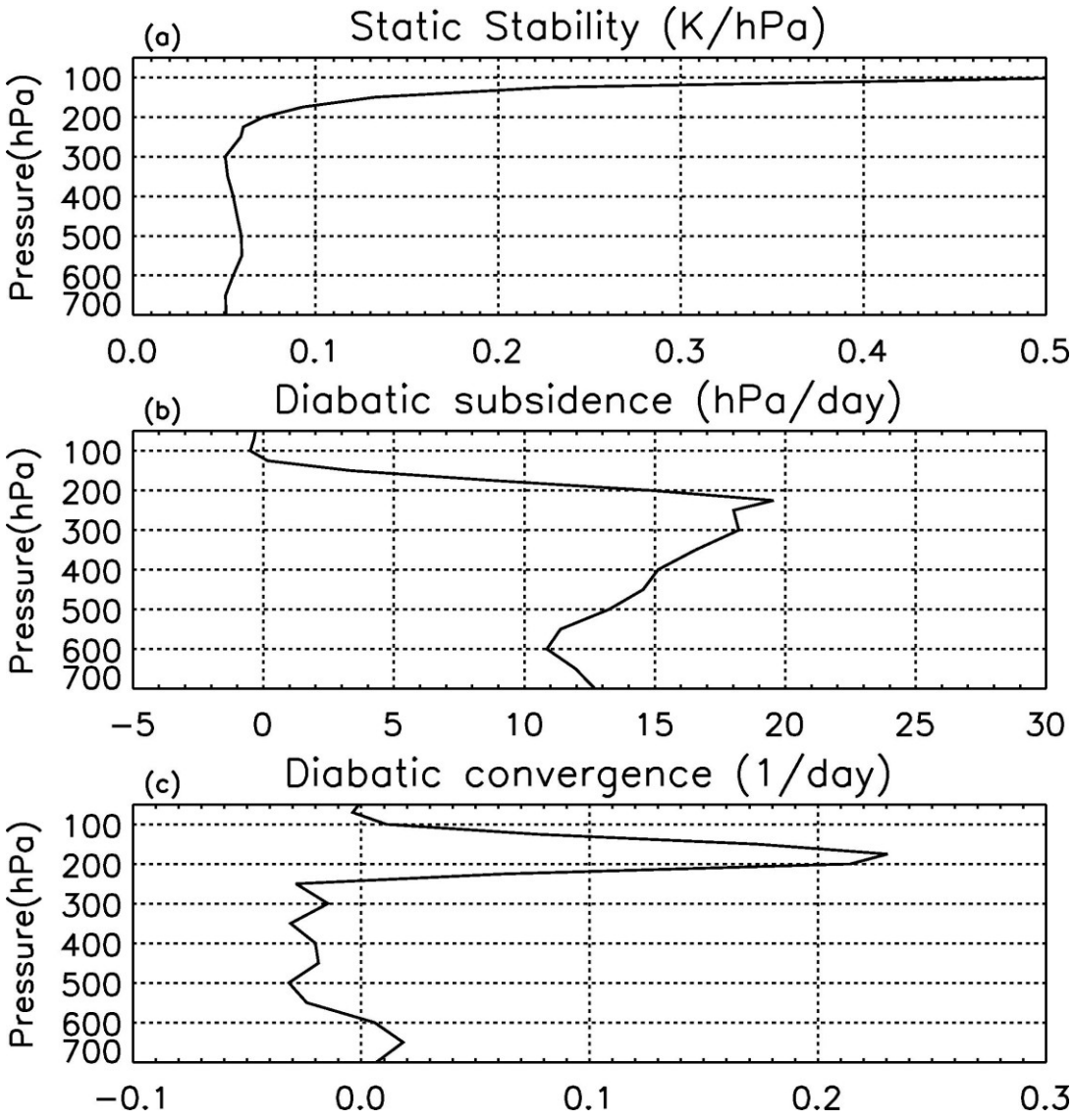

Fig. 3.3 Tropical mean profiles for clear-sky (a) static stability, (b) diabatic subsidence, and (c) diabatic convergence.

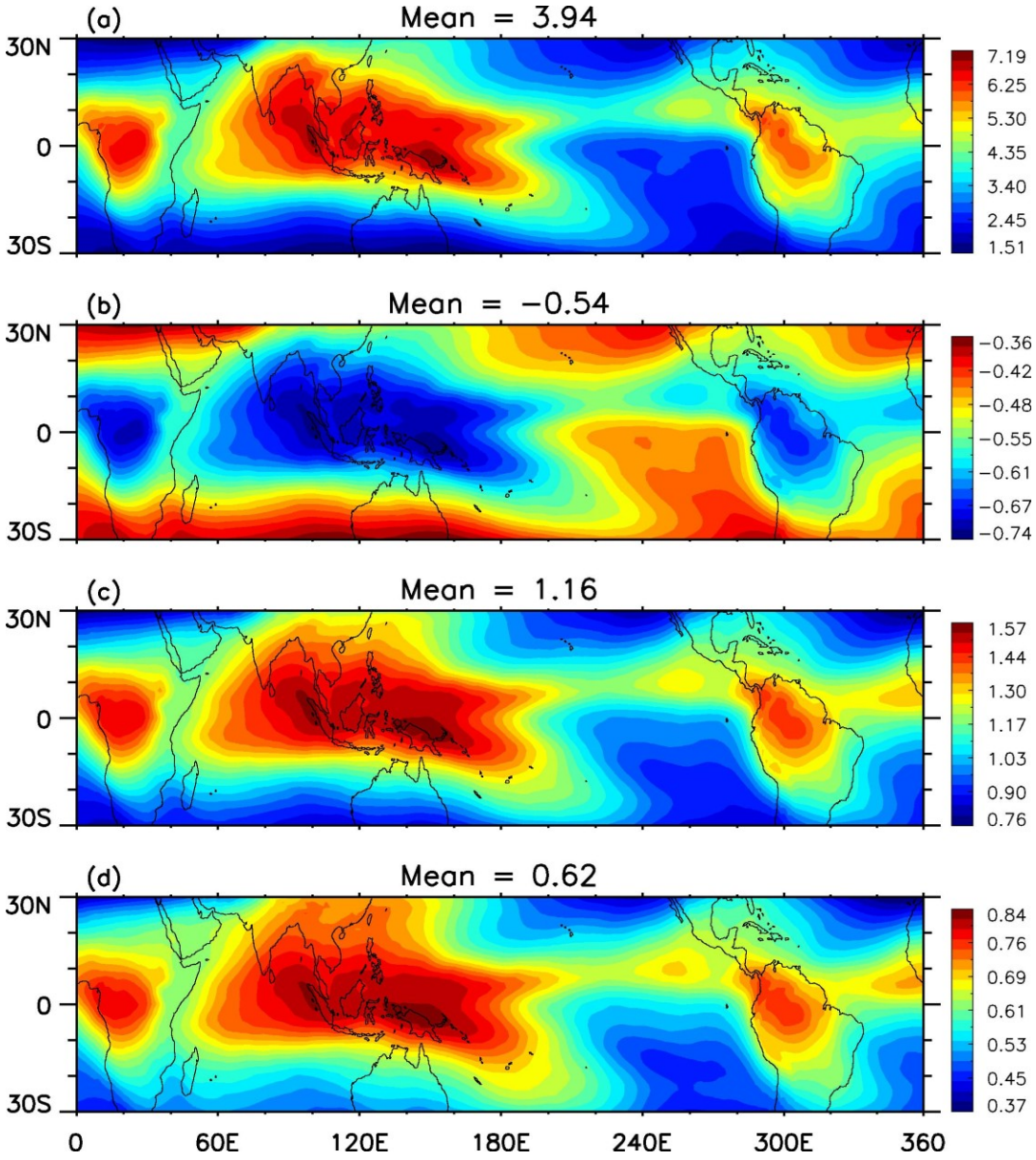

Fig. 3.4 Temporal mean spatial distributions of (a) specific humidity, (b) clear-sky SW, (c) LW, and (d) net cooling rates at 200 hPa. Specific humidity and temperature profiles used in the calculation for cooling rates are from ECMWF interim reanalysis. Units for specific humidity and cooling rates are kg/kg and K/day, respectively. Note the values for specific humidity have been multiplied by 10^5 for better plotting.

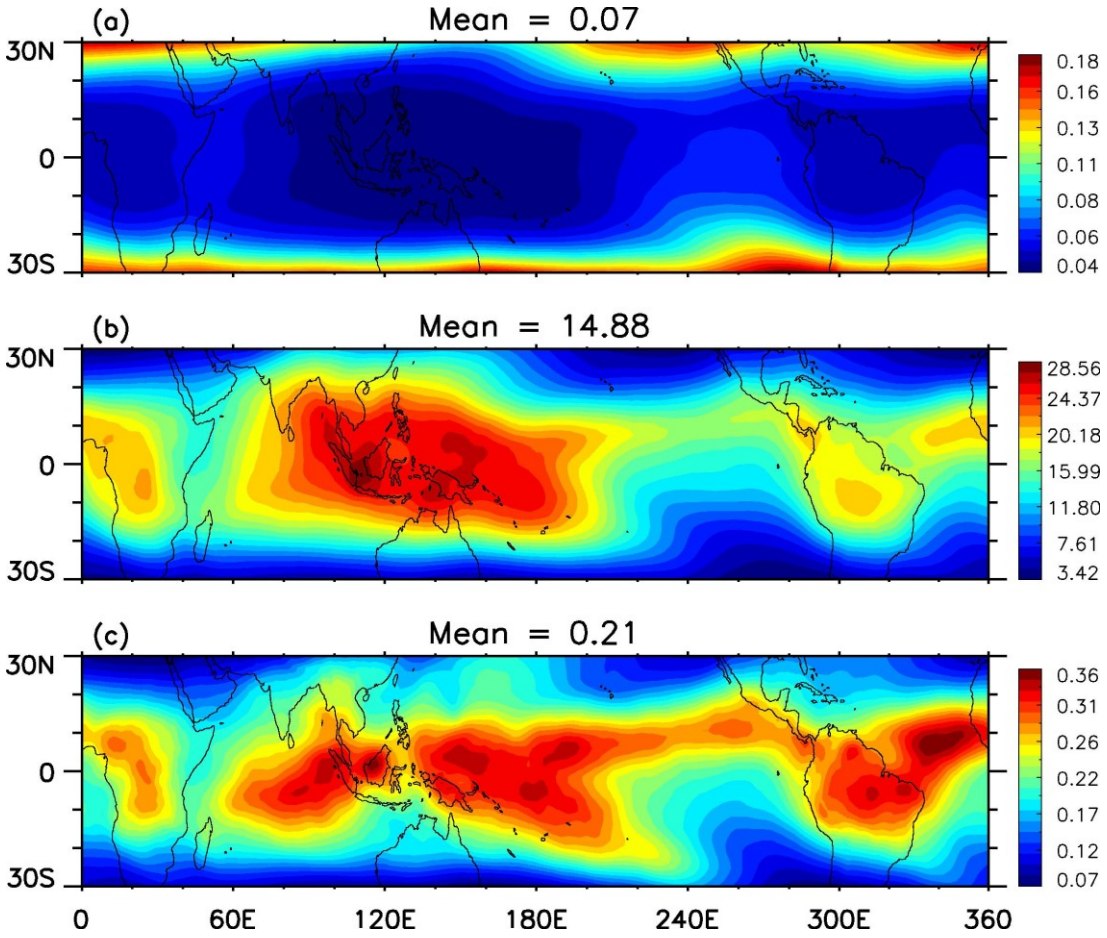

Fig. 3.5 Temporal mean spatial distributions of clear-sky (a) static stability, (b) diabatic subsidence, and (c) convergence at 200 hPa. Units are K/hPa, hPa, and 1/day, separately.

According to the physical mechanism of the FAT hypothesis, the level at which clear-sky diabatic *conv* is greatest is the convective anvil cloud detrainment level. Fig. 3.6a demonstrates the tropical mean vertical cloud fraction profile binned into each cloud top pressure range, with 50 hPa spacing between 1000 hPa and 200 hPa, and 25 hPa above. The sum of all observations from the surface to the top of the atmosphere is divided to obtain the cloud fraction in each bin. Consistent with Kubar et al. (2007) and ZH10, the peak level agrees well with that of the vertical maximum diabatic *conv* at around 200 hPa. The spatial distributions of cloud fractions from two nearby pressure bins are averaged to obtain the result for 200 hPa shown in Fig. 3.6b. The large values concentrate over the intertropical convergence zone (ITCZ), Africa, tropical Indian Ocean, western Pacific, the South Pacific convergence zone (SPCZ), and southern America. The overall patterns are similar at 300 hPa except with generally smaller magnitude. The consistency of the spatial patterns illustrates the fact that in different tropical regions, both cloudy (convective) and clear (subsidence) domains are present in different proportions. A region that shows the strongest radiative cooling in the clear-sky domain has to be accompanied by the greatest diabatic subsidence warming, which is compensated by convergence, thus being associated with the highest cloud fractions in the cloudy domain.

3.4.2 Convective CTT variations in response to SST

The sensitivity of direct CTT measurements to SST variations is a useful test of the FAT and PHAT hypotheses. To be comparable with previous studies (Xu et al. 2005,

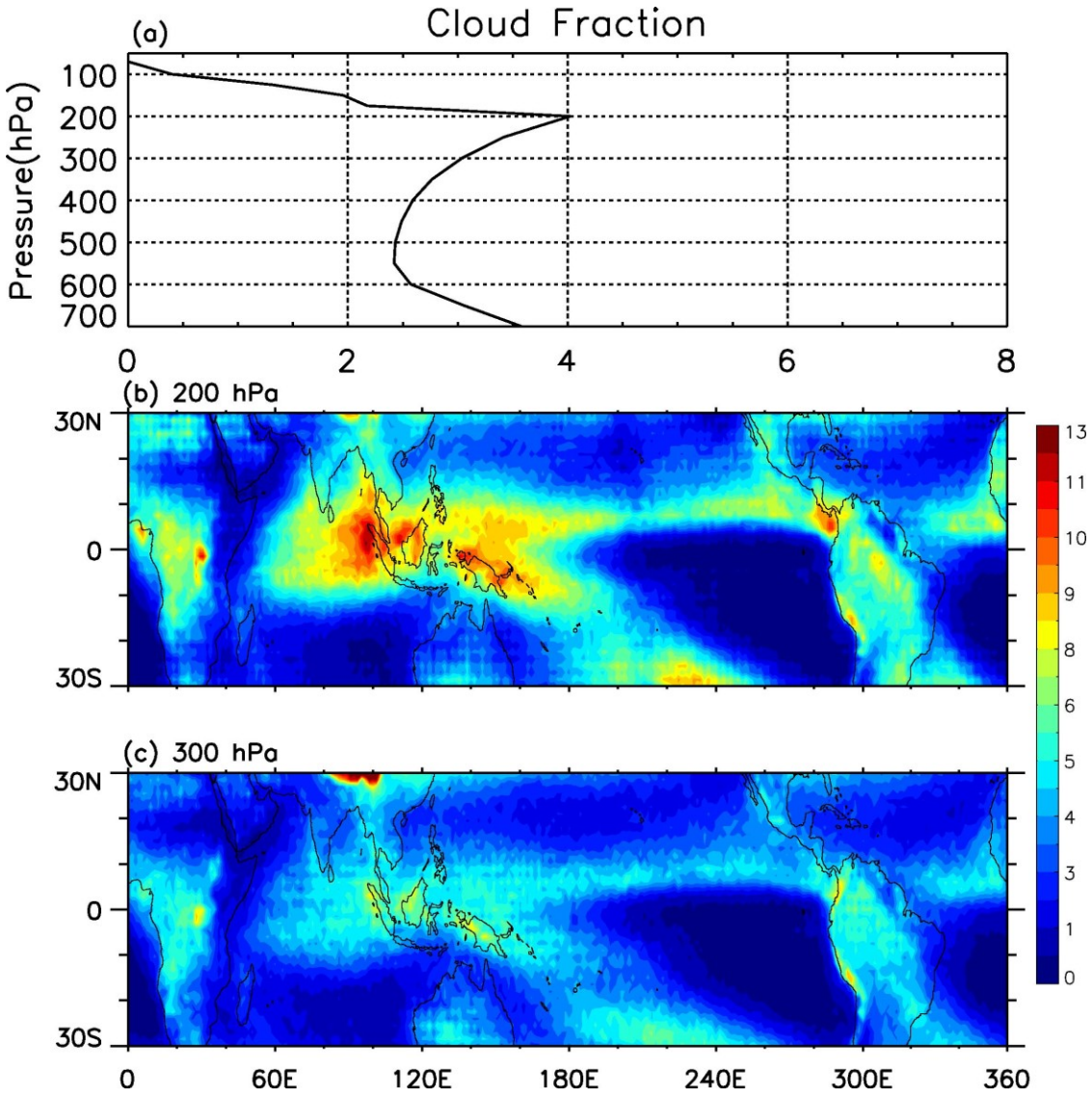

Fig. 3.6 Tropical mean (a) vertical cloud profiles averaged based on cloud top pressure bins, (b) spatial distributions of cloud fraction at 200 hPa, and (c) spatial distributions of cloud fraction at 300 hPa.

2007; Chae and Sherwood 2010), we will investigate the SST and CTT variations with seasons for individual tropical regions and for the tropics as a whole. Fig. 3.7 shows the frequency distributions of SST for the entire tropics (30ºN-30ºS), the tropical eastern Pacific (EP; 0-20ºN, 150º-100ºW), the southern Pacific (SP; 0-20ºS, 120ºE-100ºW), and the western Pacific (WP; 0-20ºN, 120º-160ºE). The bin size for the SST frequency distributions is 1 K. The shapes are negatively skewed in both seasons for the whole tropics, and the peak is shifted toward warmer SST by about 1 K in boreal summer compared to winter (Fig. 3.7a).

The interannual variations are small for the tropical average, but can be substantial for the individual regions (Fig. 3.7b-d). The differences in SST distributions on the north and south sides of the equator are consistent with the seasonal cycle. The seasonal variations are more uniform in the warm pool WP. An apparent shift of peak SST of approximately 1 K from boreal winter to summer is observed. Note a strong La Niña signal is observed for the year of 2008, particularly for the EP and the SP.

The CTT distribution histogram for deep convection with a bin size of 2 K is displayed in Fig. 3.8. The same bin size resolution is used in the following analyses for other clouds. We have conducted sensitivity tests using bin sizes from 1-6 K, and the resultant patterns are generally unchanged except that high frequency noise is introduced for the smallest bin size. The histograms for the whole tropics indicate the proportions of lower and higher CTTs are slightly lower in boreal summer and are compensated by larger frequencies in the middle, around 210 K. The patterns for the EP and SP in Fig. 3.8b and 3.8c are in contrast to the results in Fig. 3.7b and 3.7c, with lower CTT peaks in

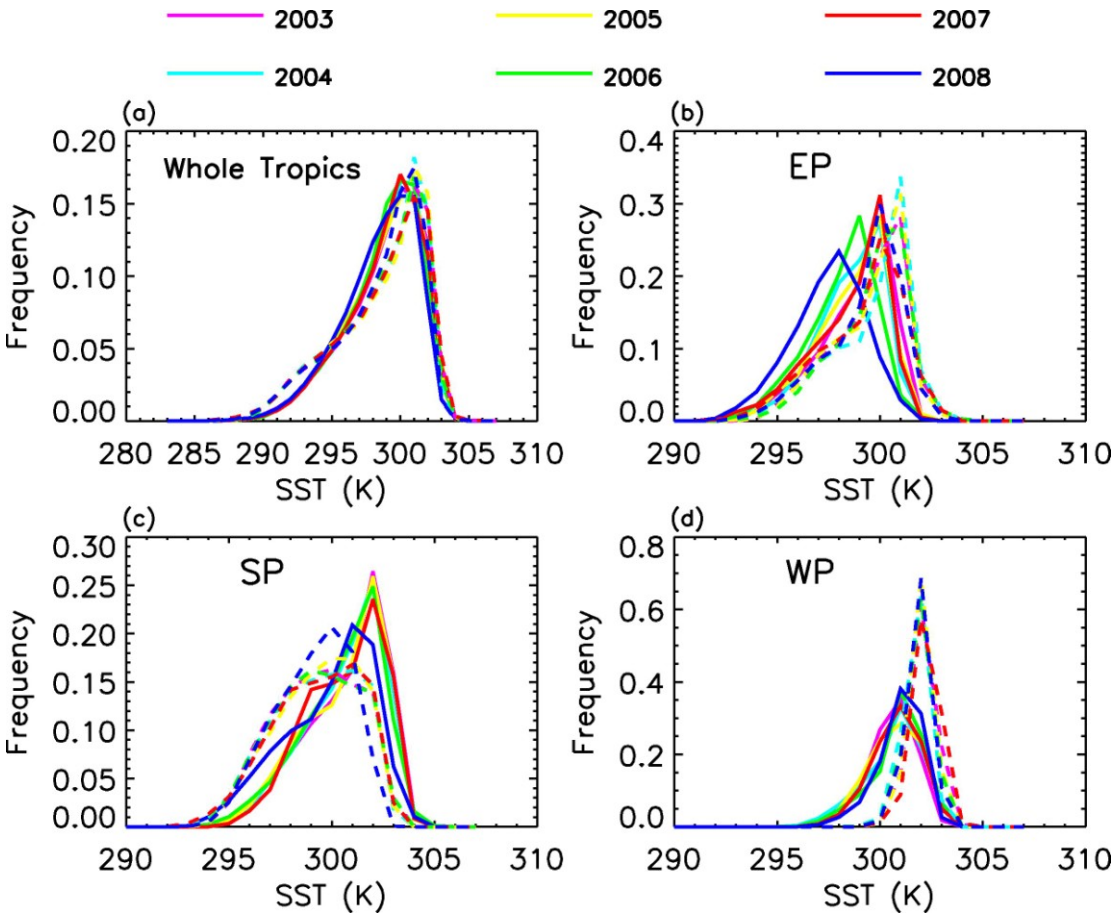

Fig. 3.7 Distributions of relative occurrence frequencies of DJF (solid) and JJA (dash) SST for (a) the entire tropics (30ºN-30ºS); (b) the EP (0-20ºN, 150º-100ºW); (c) the SP (0-20ºS, 120ºE-100ºW); and, (d) the WP (0-20ºN, 120º-160ºE).

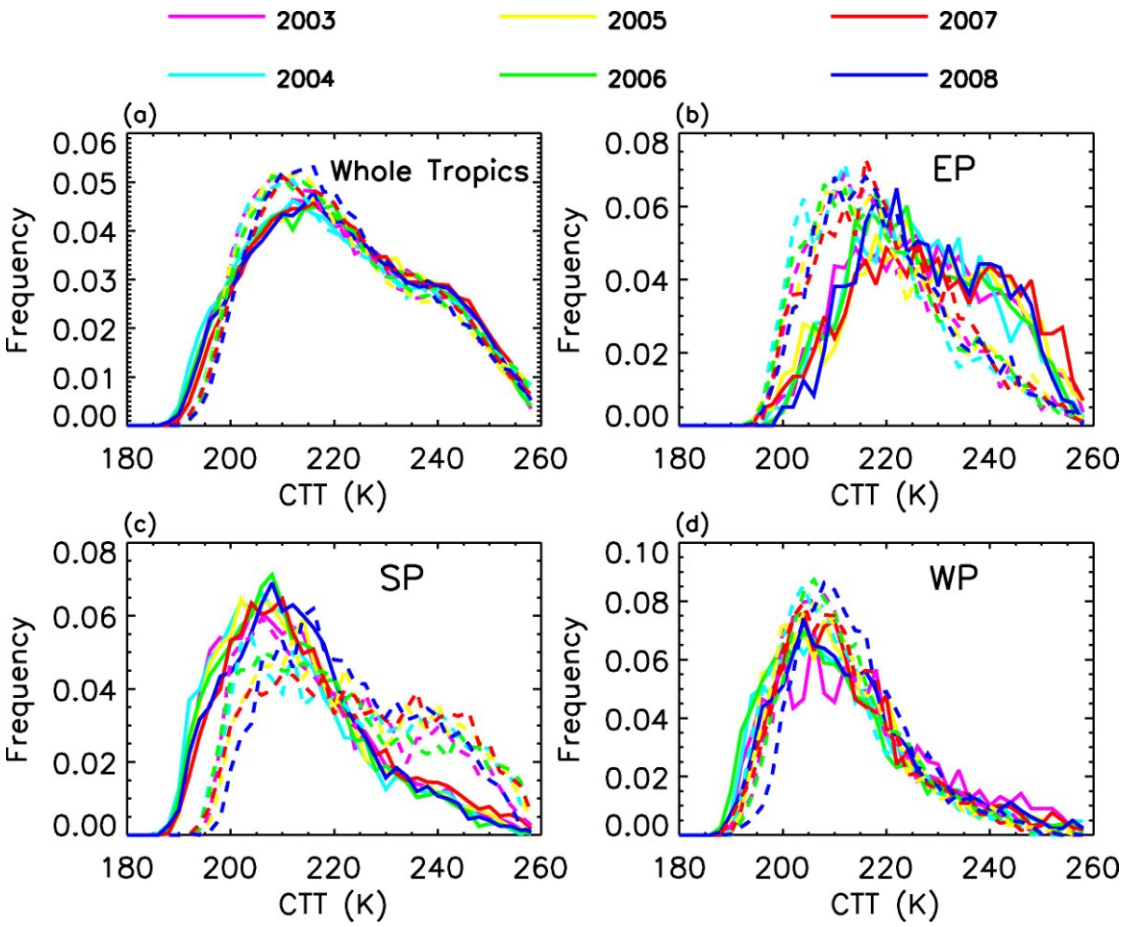

Fig. 3.8 Same as Fig. 3.7 except for the CTT associated with deep convection.

boreal summer and winter. The seasonal shift for the WP is similar to the SP; however, the distributions for the WP are not well separated with respect to seasons, as is seen in the EP and SP. The modes show pronounced peaks between 200 and 210 K, which are significantly colder than in the EP.

Fig. 3.9 shows the statistical variations of the CTT distributions for upper-level cirrus, are not as large as those for deep convection, particularly in the EP, but compared to Fig. 3.8, the fluctuations are more pronounced. The CTT in the EP are skewed toward lower values, whereas multi-modal distributions are seen in the SP and WP. A larger proportion of colder thin cirrus is observed in the WP compared to the EP due to stronger deep convections in the WP, which can penetrate into higher altitudes and generate cold cirrus through convective blow off.

Fig. 3.10 shows the distribution patterns of cirrostratus, and the overall patterns are similar to Fig. 3.9 except with smoother fluctuations. The similarities between the distributions of high clouds (Fig. 3.11), which include deep convection, cirrostratus, and thin cirrus, and that of cirrostratus indicate the high clouds contain a large proportion of cirrostratus. The CTT variations demonstrated in Figs. 3.8-3.11 are generally consistent, and the CTT response to El Niño – Southern Oscillation (ENSO), especially the 2008 La Niña, can be clearly identified.

We have calculated anomalies by subtracting the average seasonal cycle from the CTT and SST data. A least-squares linear regression is then used to determine the response of CTT anomalies to SST anomalies for the regions discussed above as well as the central Pacific (CP; 0-20ºN, 120ºE-150ºW). Fig. 3.12 shows the slopes for different

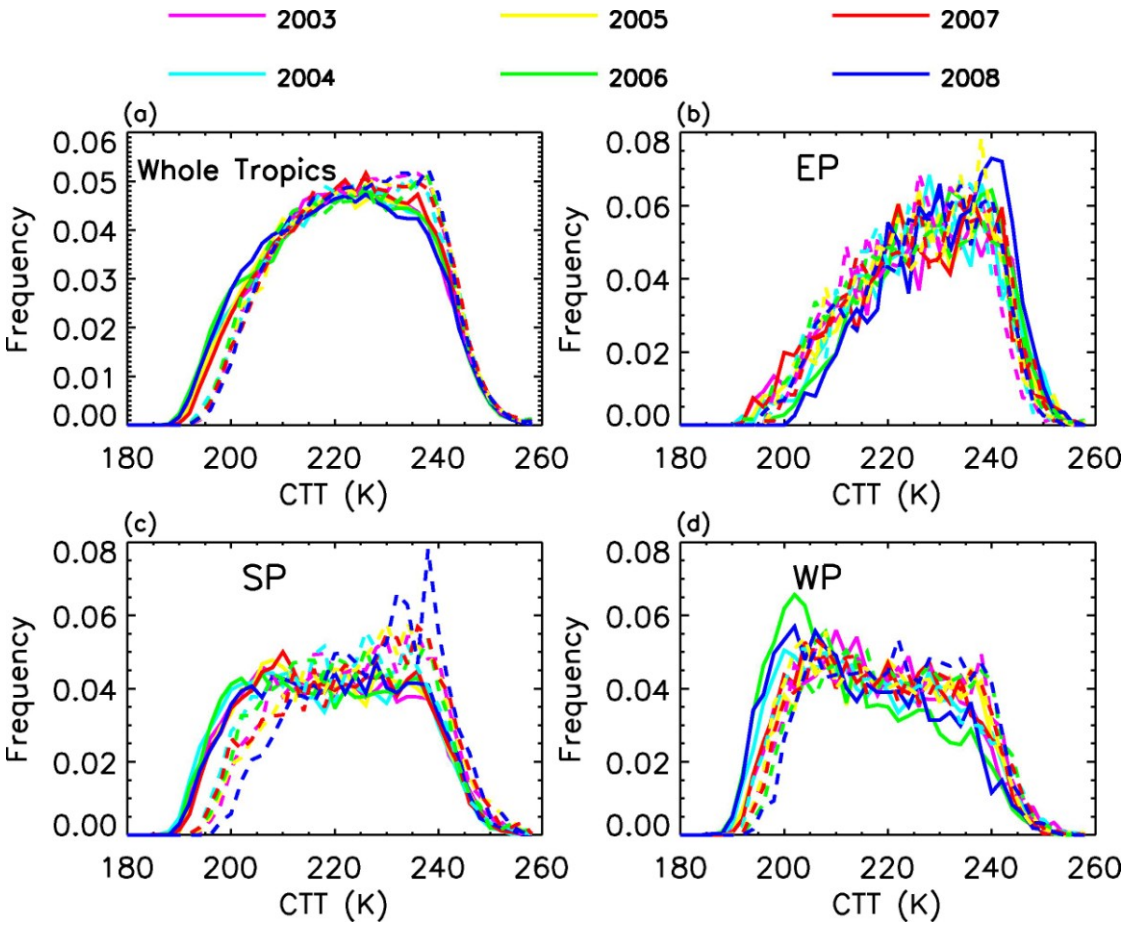

Fig. 3.9 Same as Fig. 3.7 except for the CTT associated with cirrus.

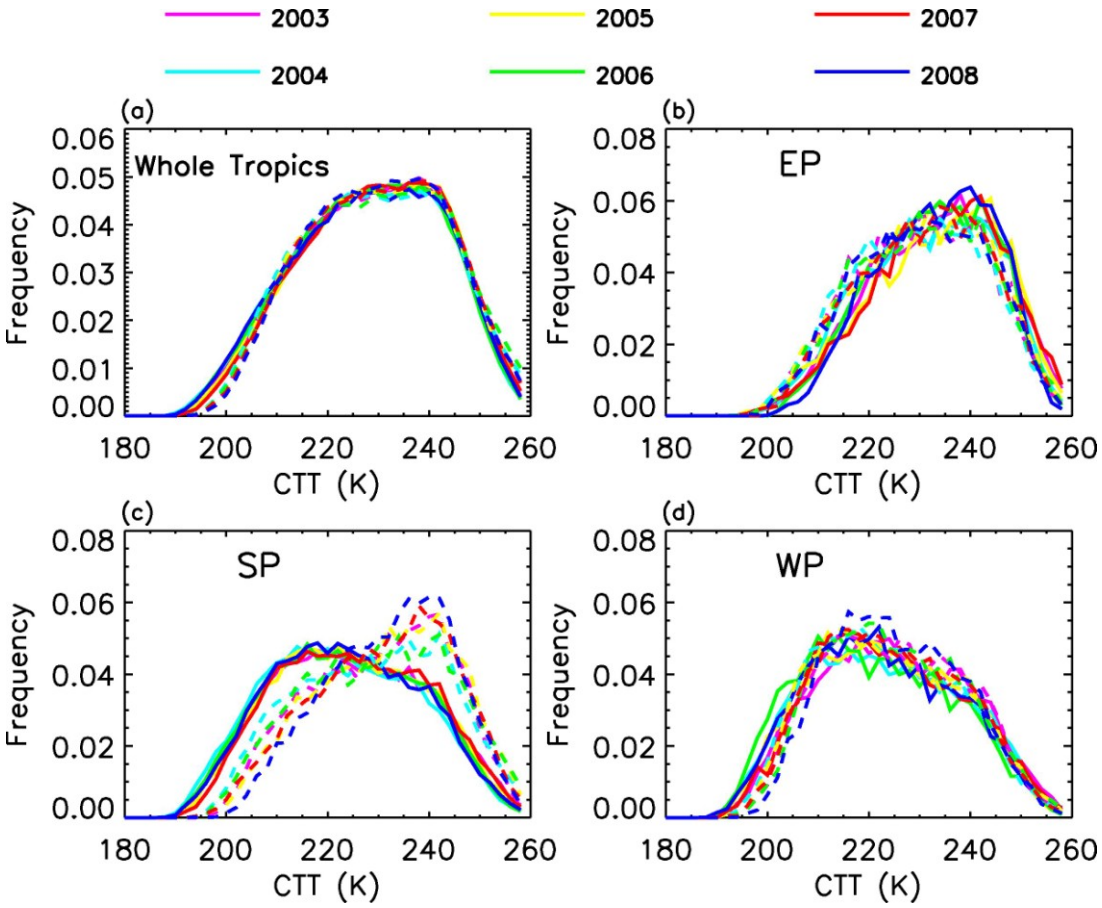

Fig. 3.10 Same as Fig. 3.7 except for the CTT associated with cirrostratus.

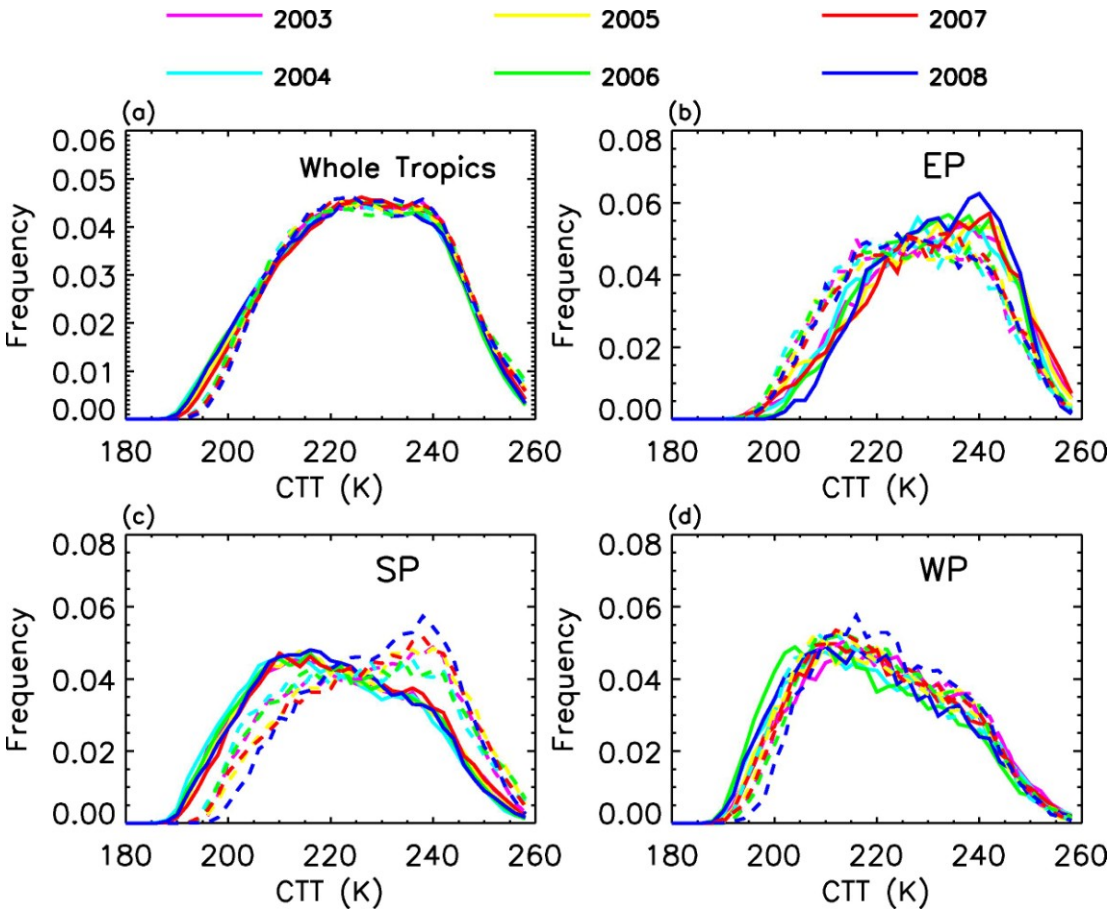

Fig. 3.11 Same as Fig. 3.7 except for the CTT associated with high clouds, which include cirrus, cirrostratus, and deep convective clouds.

regions and cloud types. The total number of degrees of freedom is 70; hence, we choose the statistical uncertainty to be 2σ, which approximately corresponds to the 95% confidence level. The slopes are all negative, although in 4 of the 16 cases we cannot rule out a positive slope at the 2s level. Overall, our results suggest a decrease of CTT with an increase in SST.

Fig. 3.13 is analogous to Fig. 3.12 except that the linear regression is performed over the tropical mean SST anomaly. The major differences are found in the WP, where the values all tend to be above 0 (Fig. 3.13c). A similar approach is performed to obtain the slopes when both CTT and SST anomalies are averaged over the entire tropics (Fig. 3.13e). In general the values are negative except for cirrus, whose slope is approximately 0. However, the uncertainties are roughly the same magnitude as the slopes, resulting in the upper ranges close to or slightly above 0.

To explore the reason that accounts for the differences for the WP between Fig. 3.12 and Fig. 3.13, we plot time series of SST anomalies over different regions (Fig. 3.14). Apparent differences are observed for the WP compared to other regions. While similarities of patterns are observed in other regions from neutral oscillations before 2007 to a strong La Niña in 2008, the oscillations in the WP are in greater magnitude, which masks the La Nina signal.

Fig. 3.15 shows the spatial distributions of the same quantity by regressing a monthly mean CTT anomaly at an individual location over the tropical mean SST. Only values greater than $\sigma/2$ are plotted taking into account significantly less pairs of values for each individual grid. We would like to emphasize the choice of this uncertainty is not

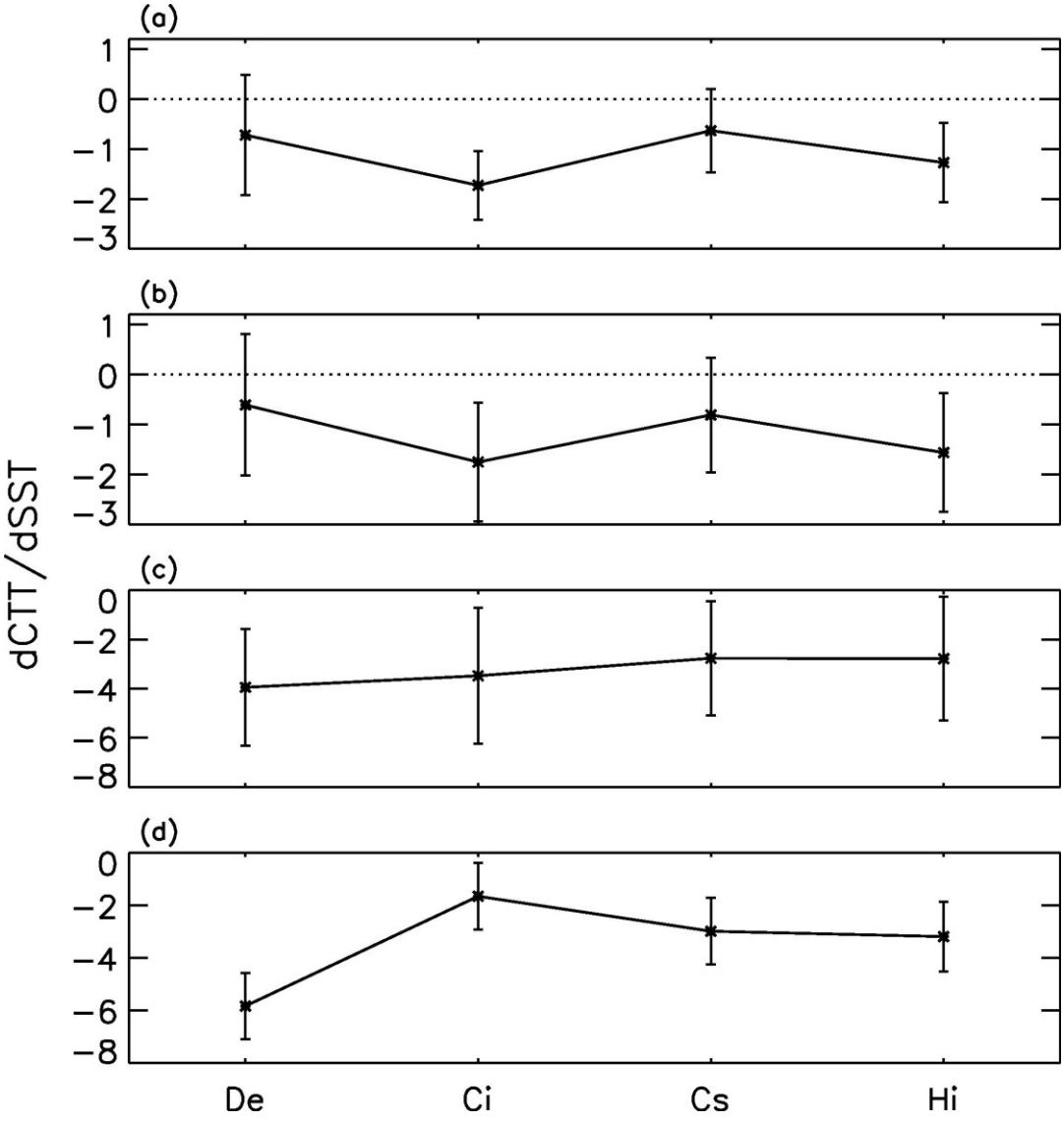

Fig. 3.12 Slopes for regional averaged monthly CTT anomalies linearly regressed over regional mean SST anomalies with uncertainties for (a) the EP, (b) the SP, (c) the WP, and (d) the CP. De, Ci, Cs, and Hi represent deep convection, high thin cirrus, cirrostratus and high cloud. The uncertainties are computed as 2σ, where σ is the standard error.

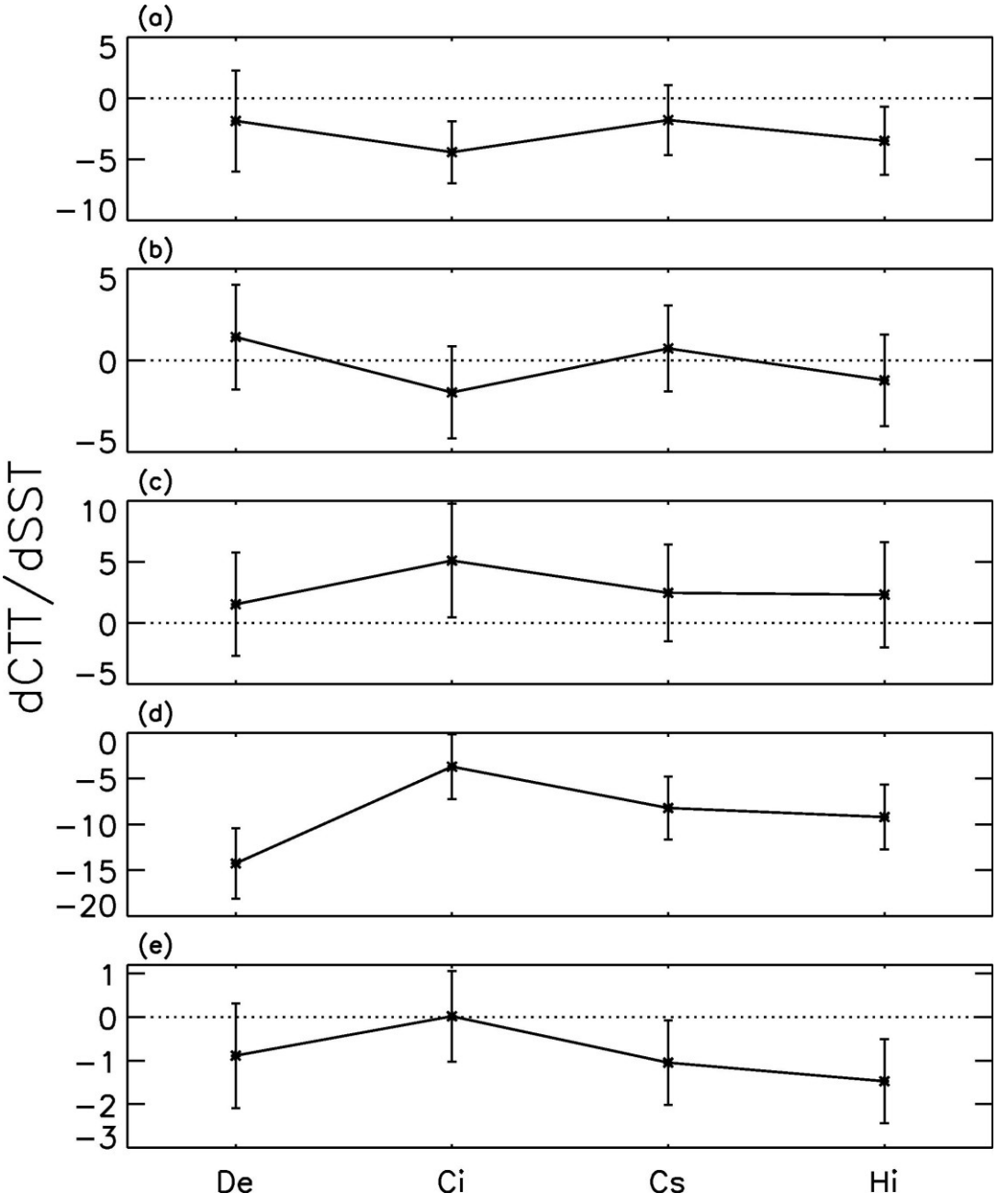

Fig. 3.13 Similar to Fig. 3.12 except for regional mean CTT anomaly linearly regressed over tropical mean SST anomalies for (a) the EP, (b) the SP, (c) the WP, (d) the CP, and (e) the entire tropics.

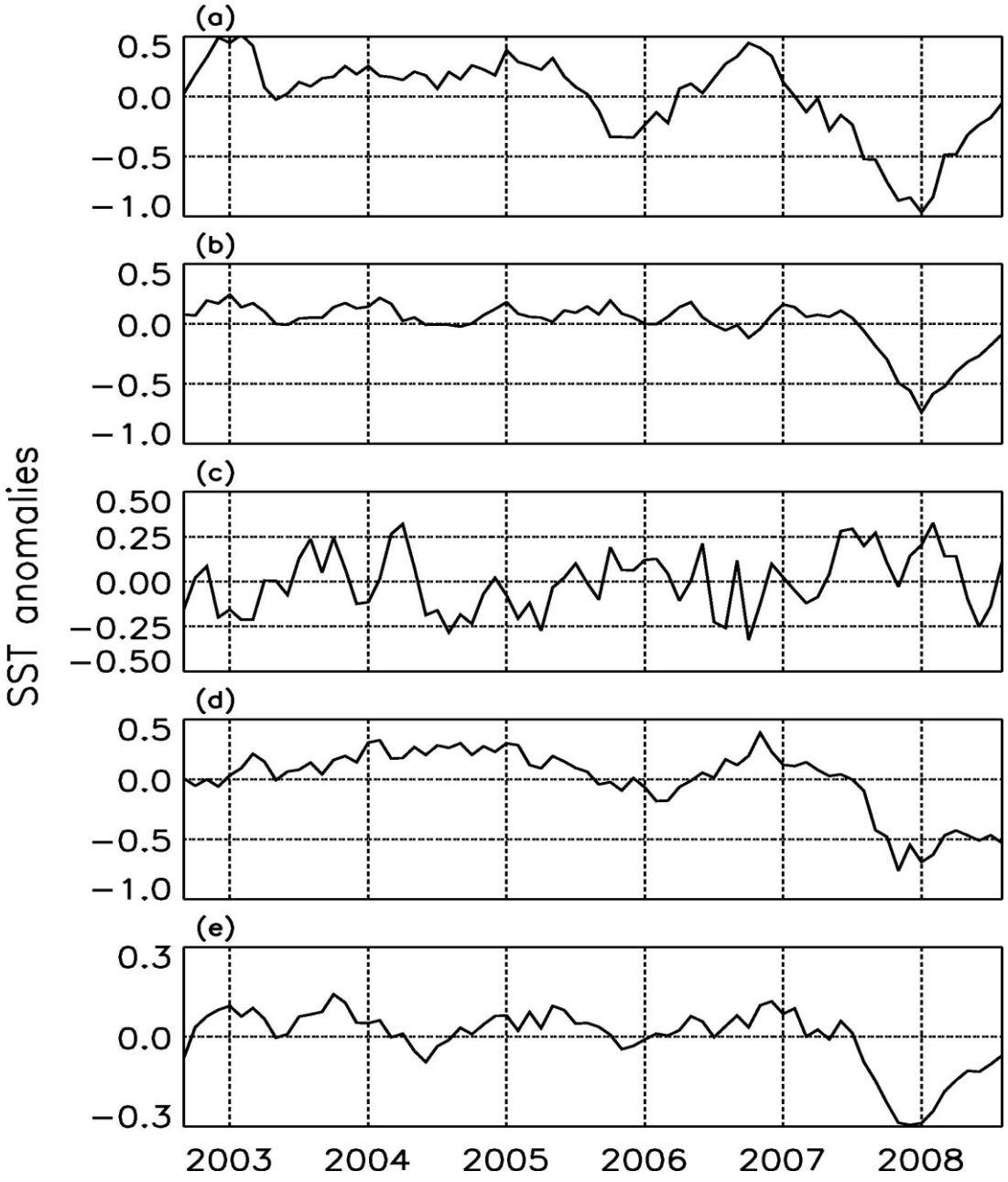

Fig. 3.14 Tropical SST monthly anomalies derived by subtracting seasonal mean for (a) the EP, (b) the SP, (c) the WP, (d) the CP, and (e) the entire tropics. Units are in K.

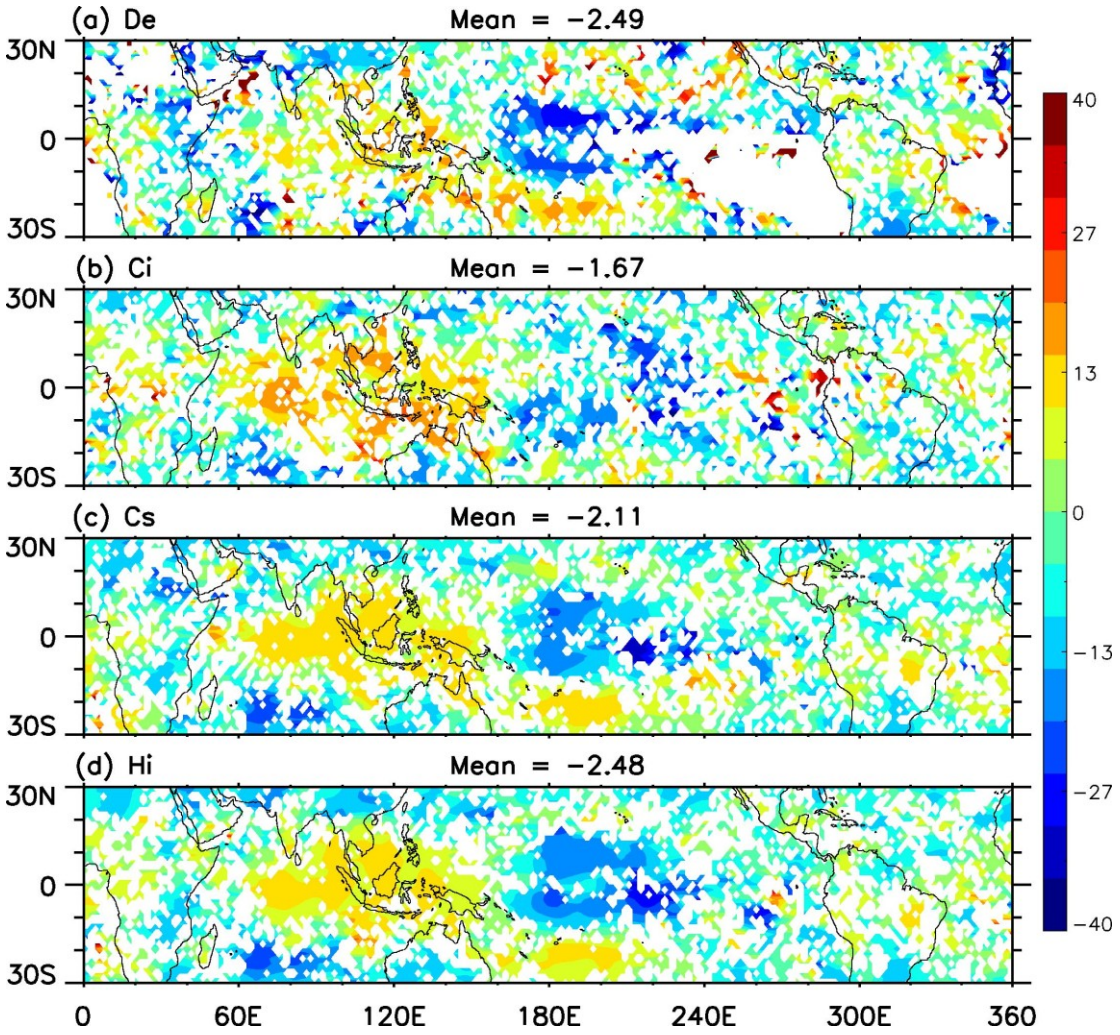

Fig. 3.15 Spatial distributions of slopes for CTT anomaly at individual location linearly regressed over tropical mean SST for (a) deep convection, (b) thin cirrus, (c) cirrostratus, and (d) high cloud. Only values with magnitudes greater than $\sigma/2$ are plotted. Each figure is smoothed by a 1-2-1 filter 10 times in both longitude and latitude.

meant to be used as a statistical constraint; rather, we attempt to show the spatial patterns of the correlation. Two robust features observed are a positive peak located at the tropical west Pacific through the Indian Ocean and a negative peak in the central Pacific. Few values are observed over the eastern Pacific due to relatively weak convective activity (Hartmann et al. 2001b). This appears to be consistent with a dominant ENSO response: as the tropics warm during ENSO, high clouds move eastward into the central and eastern Pacific. This produces the dipole pattern.

3.5 Summary and discussion

The present study suggests that clear-sky diabatic convergence peaks are well correlated with peak cloud fraction profiles at around 200 hPa. The geographical maximum regions for water vapor concentration agree well with clear-sky cooling rates, diabatic subsidence, diabatic convergence, and cloud fraction in tropical Africa, tropical western Pacific and Indian Oceans, and southern America.

We show variations of CTT in boreal summer and winter for individual ocean basins. The peaks of CTT shift to lower values as SST increases in the EP and SP. Conversely, the WP region indicates a uniform shift of SST toward higher values in boreal summer with a small increase of CTT. When considering the tropics as a whole, variations in both the SST and CTT are small, primarily due to the fluctuations from individual regions cancelling each other.

Analysis of the response of regionally averaged monthly CTT anomalies to the SST reveals the relationship to be misleading when not properly accounting for the effects of

ENSO. The FAT hypothesis is based on radiative-convective equilibrium; hence, is more applicable to the tropics as a whole because the entire regional dynamic effects can be substantial. Unlike the finding, reported by ZH10, of a modest increase in the temperature at the peak cloud detrainment level as the climate warms, our analysis indicates the likelihood that a negative relationship exists between the CTT and the SST. We speculate the reason is that the FAT hypothesis is commonly misinterpreted using the cloud top temperature; it should, rather, reflect the temperature at the peak cloud detrainment level. Bear in mind that a non-negligible amount of cloud exists above the peak detrainment level, and the satellite sensor may recognize this as the cloud top. Our findings are not meant to suggest that the FAT hypothesis is wrong. Rather, we have demonstrated the difficulty of testing and interpreting the FAT hypothesis using satellite-retrieved CTT. Instead, it is more appropriate to denote the temperature at the peak cloud detrainment level, which can be obtained by aligning vertical cloud profile against atmospheric temperature.

The negative relationship indicates a stronger positive longwave cloud feedback in comparison to the FAT and PHAT hypotheses. However, we wish to stress that a long-term global warming is unlike the SST variations caused by seasonal shifts and the ENSO. Further investigation using more accurate observations of cloud top properties, such as those measured by the Cloud-Aerosol Lidar and Infrared Pathfinder Satellite Observations (CALIPSO), is necessary to better quantify the SST-CTT relationship.

CHAPTER IV

INTERCOMPARISON OF HIGH CLOUDS AND THEIR RADIATIVE PROPERTIES BETWEEN THE NCAR CAM MODELS AND SATELLITE OBSERVATIONS

4.1 Background

Despite advances in satellite remote sensing techniques and climate model development, large uncertainties exist in accurately describing high cloud radiative, optical, macrophysical and microphysical properties (Liou 1986; Minnis et al. 1993; Liu and Curry 1999; Dessler and Yang 2003; Zhang et al. 2005). Depending on the optical properties, high clouds exert significantly different radiative impacts on the earth-atmosphere system (Yang et al. 2007). For instance, even though clouds generally cool the earth, thin contrails demonstrate a net warming effect (Minnis et al. 1999; Ponater et al. 2002; Meyer et al, 2002). Therefore, a pressing need is to quantify the radiative effect of high clouds, i.e., the global distribution of cloud radiative forcing (CRF) related to cirrus, cirrostratus, and deep convection, and to improve the parameterization scheme in climate models. The total cloud radiative effect can be attributed to CRF and cloud fraction related to individual cloud types. Hence, it is crucial to investigate the geographical distribution and seasonal variation of these clouds.

Validation studies of cloud fraction and CRFs simulated by global circulation models (GCMs) are numerous. Examples include the studies of Kiehl et al. (1998), Lin and Zhang (2004), and the 10-model intercomparison of Zhang et al. (2005), which

examined the simulation of clouds with different top heights and optical properties. Despite reasonable agreement on total cloud properties, the basic high cloud climatologies simulated by GCMs are substantially different from those inferred from satellite observations. Moreover, variations of simulated high clouds across models are pronounced.

The MODIS instrument utilizes 36 spectral bands ranging from visible to infrared bands and provides unprecedented high-resolution cloud property retrievals, including cloud fraction, cloud top information and optical properties. The availability of these retrievals makes it possible to establish a reliable high cloud climatology. Evaluation of the capability of current GCMs in simulating high clouds using MODIS is necessary. The purpose of this chapter is to compare cloud fraction and CRF simulated by two versions of the National Center for Atmospheric Research (NCAR) community atmosphere model (CAM) with MODIS and a reanalysis dataset. We also attempt to identify biases related to various types of high clouds.

4.2 Data

4.2.1. MODIS

Cloud fraction data from daily Aqua MODIS Collection 5 gridded Level 3 product are used. The time span is from January 2003 to December 2006. Addition, cloud optical thickness (τ) and cloud top pressure (P_c) are also utilized to specify each cloud type according to the ISCCP classification scheme.

4.2.2. MERRA

The radiation fields from the latest NASA reanalysis, the Modern Era Retrospective-analysis for Research and Applications (MERRA), are used as observational constraint for the CRFs. The Goddard Earth Observing System, version 5 (GEOS-5) data assimilation system is used in MERRA. A detailed description of MERRA/GEOS-5 numerical model is in Rienecker et al. (2010). The radiation fields have a spatial resolution of 2/3° longitude by 1/2° latitude with 1-hour interval. We utilize both clear and cloudy-sky flux data at the top of the atmosphere (TOA) between January 2003 and December 2004. Daily average is first obtained at the original spatial resolution, and SW CRF and LW CRF are computed. Then CRFs binned at a reduced horizontal resolution same as MODIS cloud data (1° × 1°) are obtained.

4.3 Models

4.3.1 The CAM models

The first model involved is the NCAR CAM Model, version 3 (CAM3) (Collins et al. 2004). In CAM3, the parameterization scheme for deep convection follows Zhang and McFarlane (1995). Shallow convection scheme is described by Hack (1994). The cloud fractions for three cloud types corresponding to layered cloud, low-level marine stratus and convective cloud and are determined diagnostically based on relative humidity, static stability, and convective properties. A prognostic scheme to predict cloud water was introduced in the microphysical package by Rasch and Kristjansson (1998) and revised with the macrophysical formulation of Zhang et al. (2003). For SW

radiation, the water cloud optical properties follow Slingo (1989). The parameterization scheme for ice cloud radiative properties is based on Ebert and Curry (1992), who parameterized the broadband optical properties as a function of both effective particle size and cloud water path. The cloud droplet effective radii for water clouds are specified to be 14 μm over both ocean and sea ice surface. Over land, the values are parameterized as a function of temperature. For ice clouds, the effective radius is a function of temperature only.

The CAM5 model used here forms the atmospheric component of the Community Earth System Model (CESM), version 1.0.2. CAM5 is the latest version of CAM series. Major changes include enhancements to the Zhang and McFarlane (1995) deep convection parameterization, a new shallow convection scheme (Park and Bretherton 2009) and cloud microphysical scheme (Morrison and Gettelman 2008, Gettelman et al. 2008), a revised cloud macrophysical scheme, and an updated radiative transfer model. Computation of cloud fraction is treated separately as cumulus and stratus. The treatment of deep cumulus fraction uses the empirical formula similar as in CAM3, while shallow cumulus convection is directly computed using the convective updraft mass flux following Park and Bretherton (2009). In addition, CAM5 diagnoses separate liquid and ice stratus fractions as a function of relative humidity (Gettelman et al. 2010), respectively. Ice cloud optics is updated to a lookup table linking optical properties to effective diameter calculated based on the modified anomalous diffraction approximation (MADA; Mitchell 2000, 2002; Mitchell et al. 2006). The liquid cloud optical properties are stored in a lookup table computed by the Mie code (Wiscombe

1996).

4.3.2 RRTMG

RRTMG (Iacono et al. 2008, Mlawer et al. 1997), which uses the correlated k-distribution method and a two-stream approximation, is incorporated to CAM5 as the radiative transfer solver for both longwave (LW) and shortwave (SW) radiation. RRTMG is a reformatted version of RRTM to enhance the calculation efficiency in climate models. Solar spectrum is divided into 14 SW bands from 0.2 μm to 12.2 μm, and the infrared spectrum has 16 LW bands from 3.1 μm to 1000 μm. The Monte-Carlo Independent Column Approximation (McICA; Pincus et al. 2003) is used in both LW and SW spectrum to represent sub-grid scale cloud variability. RRTMG utilizes gas absorption coefficient data for the k-distributions from the line-by-line radiation model.

4.3.3 The ISCCP simulator

To facilitate the comparison between observations and model results, the ISCCP simulator (Klein and Jacob 1999; Webb et al. 2001) embedded to CAM models is turned on. Version 3.4 of the ISCCP simulator is adopted in the CAM3 run, whereas an updated version (3.8) is used in the CAM5 run.

The ISCCP simulator attempts to emulate the ISCCP algorithm by downscaling the clouds at each layer to top-viewed cloud-free and cloudy subcolumns, as well as cloud water contents. τ of each subcolumn is computed. Cloud overlapping assumptions are utilized to align the subcolumns vertically. Then the cloud top at each subcolumn is

adjusted using emissivity to mimic satellite observations. The clouds of the thinnest optical interval may be below the minimum range detectable by satellite sensors. Therefore, a major issue related to the simulator is the cutoff value of τ (Jin et al. 1996; Zhang et al. 2005). In this study, the default cut-off value of 0.3 is adopted.

Some major changes in version 3.8 are noted, including new diagnostic cloud top variables, improved consistency between output variables, replacement of the albedo-τ conversion tables with analytic functions, and the "lightweight diagnostics" — restriction of calculation to clouds in subcolumns with τ greater than the cutoff value. The lightweight diagnostics tend to increase grid mean optical thickness if a grid column has large number of subcolumns with τ less than the cutoff value.

In this study, CAM3 was configured to run at T85 spectral resolution (1.4° × 1.4° grid) using 26 vertical levels. The CAM5 run is performed using the finite volume dynamical scheme with a spatial resolution of 2.5° longitude by 1.875° latitude and 30 levels in the vertical. Observed monthly mean sea surface temperature (Hurrell et al. 2008) is used as external forcing for both model runs.

4.4 Methodology

To make comparisons for specific cloud types, in particular high clouds, the ISCCP cloud classification schemes are used. P_c and τ are used as constraints to obtain monthly mean cloud fraction and CRFs for each cloud type. Monthly mean cloud fraction at a grid is calculated by the sum of fraction for each specific cloud type divided by the total number of observations in a month. Daily mean CRF at reduced resolution are

collocated with MODIS to compute CRFs for individual cloud types. Additionally, cloud fraction and CRFs for total cloud are calculated. The retrieval of P_c and τ are not required for the computation of total cloud properties.

Similarly, monthly mean cloud fraction and CRFs for CAM3 and CAM5 simulations are computed. Because satellite retrievals of cloud properties in high latitudes are more uncertain, we focus on latitude ranges between 60ºN and 60ºS.

Note that our method of computing fractional coverages of each specific cloud differs from that of Zhang et al. (2005), who obtained cloud fraction for each type in a grid column. However, the statistical mean should be approximately the same. Our method ensures that the computation is consistent across models and observations, since no subcolumn information can be derived from MODIS gridded data. In the following context, we use DJF and JJA to refer boreal winter and summer, respectively.

4.5 Results

4.5.1 Zonal variations

Fig. 4.1 shows the annual zonal mean cloud fraction and CRFs for total clouds at boreal summer and winter seasons, separately. Overall, both models are capable of capturing major zonal variations, such as the tropical peak and subtropical minima. However, some apparent differences are noted. CAM3 in general underestimates cloud fraction, while overestimates the magnitudes of CRFs. Simulated subtropical minima in cloud fraction are more poleward. Compared to CAM3, consistency in cloud fraction between CAM5 and MODIS improves considerably. CAM5 also tends to simulate better

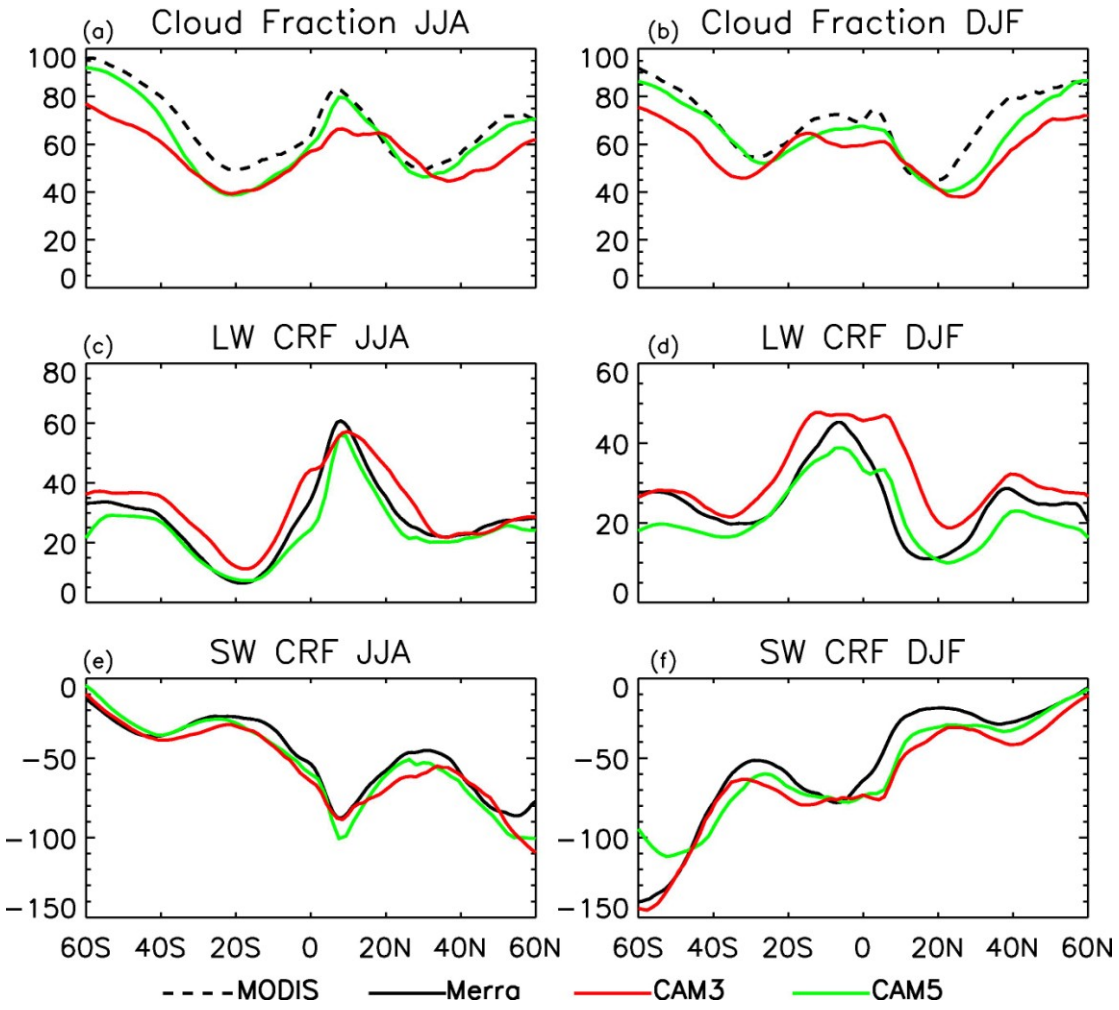

Fig. 4.1 (a), (b) Zonally averaged total cloud fraction in MODIS, CAM3 and CAM5 for JJA and DJF; (c), (d) Zonally averaged total cloud LW CRF in MERRA, CAM3 and CAM5 for JJA and DJF; (e), (f) Zonally averaged total cloud SW CRF in MERRA, CAM3 and CAM5 for JJA and DJF. CRF units are W m^{-2}.

CRFs, especially in the subtropics. However, a bias poleward of 40ºS in DJF is apparent in CRFs, in particular for SW CRF by as much 50 W m^{-2}.

Fig. 4.2 shows cloud fraction and CRFs for high cloud. Midlatitude peaks in cloud fraction diminish, suggesting that more middle and low top clouds dominate in these regions. In contrast to total cloud, CAM series generally overestimate high cloud. Although the same cutoff values of τ (0.3) are used, CAM5 estimates considerably larger values than CAM3, especially in the tropics. Conversely, CAM5 demonstrates an appreciable underestimation of LW CRF, whereas CAM3 agrees better with MERRA. Both models do well in the SW CRF between 20ºS and 20ºN. Further poleward, CAM5 is biased high (less negative). In particular, the difference with MERRA is by as much 130 W m^{-2} in southern hemisphere DJF, which partially accounts for the SW CRF bias in Fig. 4.1(f).

We have also computed the zonal means for middle and low top clouds to explore potential compensation errors (Fig. 4.3 and 4.4). Fig. 4.3 shows that for middle cloud (440 hPa < Pc < 680 hPa), there is no systematic model error in estimating cloud fraction as seen for high cloud. Fractional coverage shows a small bump in the tropics and reaches maxima in the midlatitude. Whereas both models slightly underestimate fraction in the tropics, CAM3 and CAM5 tend to underestimate and overestimate values poleward, respectively. The exception is observed in JJA when each model shows very good agreement with MODIS for one branch. Simulation of LW CRF is reasonably well poleward of 20º and 40º in local hemisphere winter and summer, respectively. The values in the tropics, however, differ greatly that MERRA is twice more than

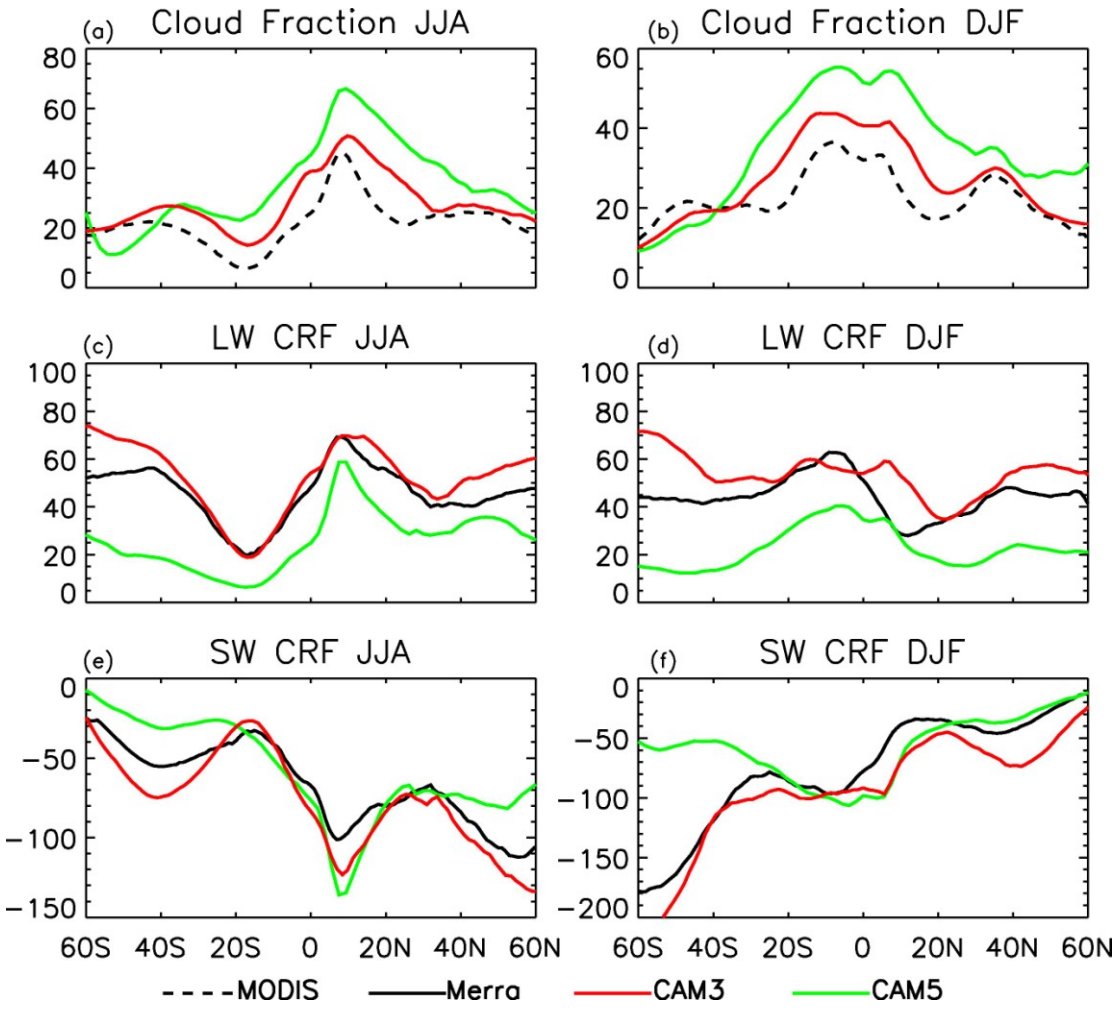

Fig. 4.2 Same as Fig. 4.1 except for high cloud only.

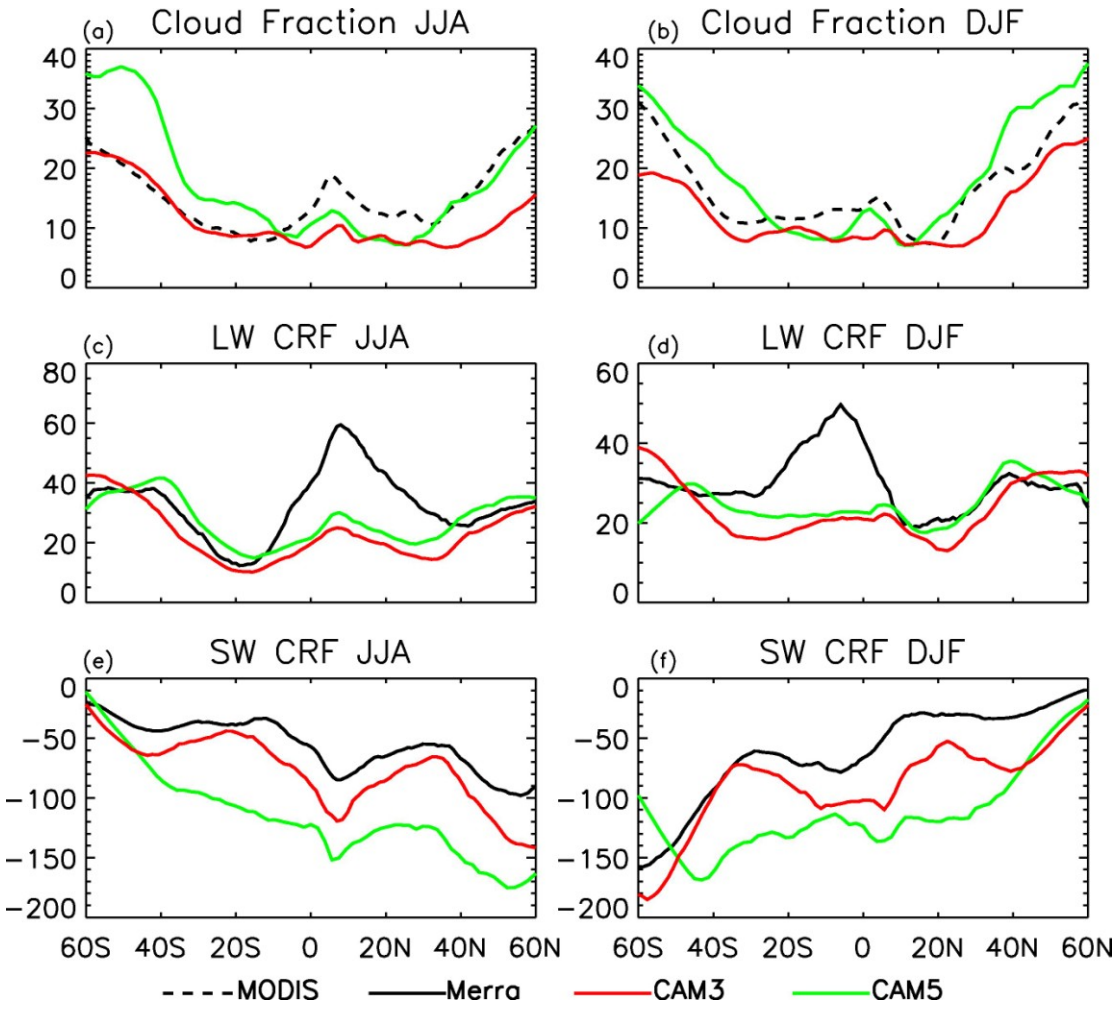

Fig. 4.3 Same as Fig. 4.1 except for middle cloud only.

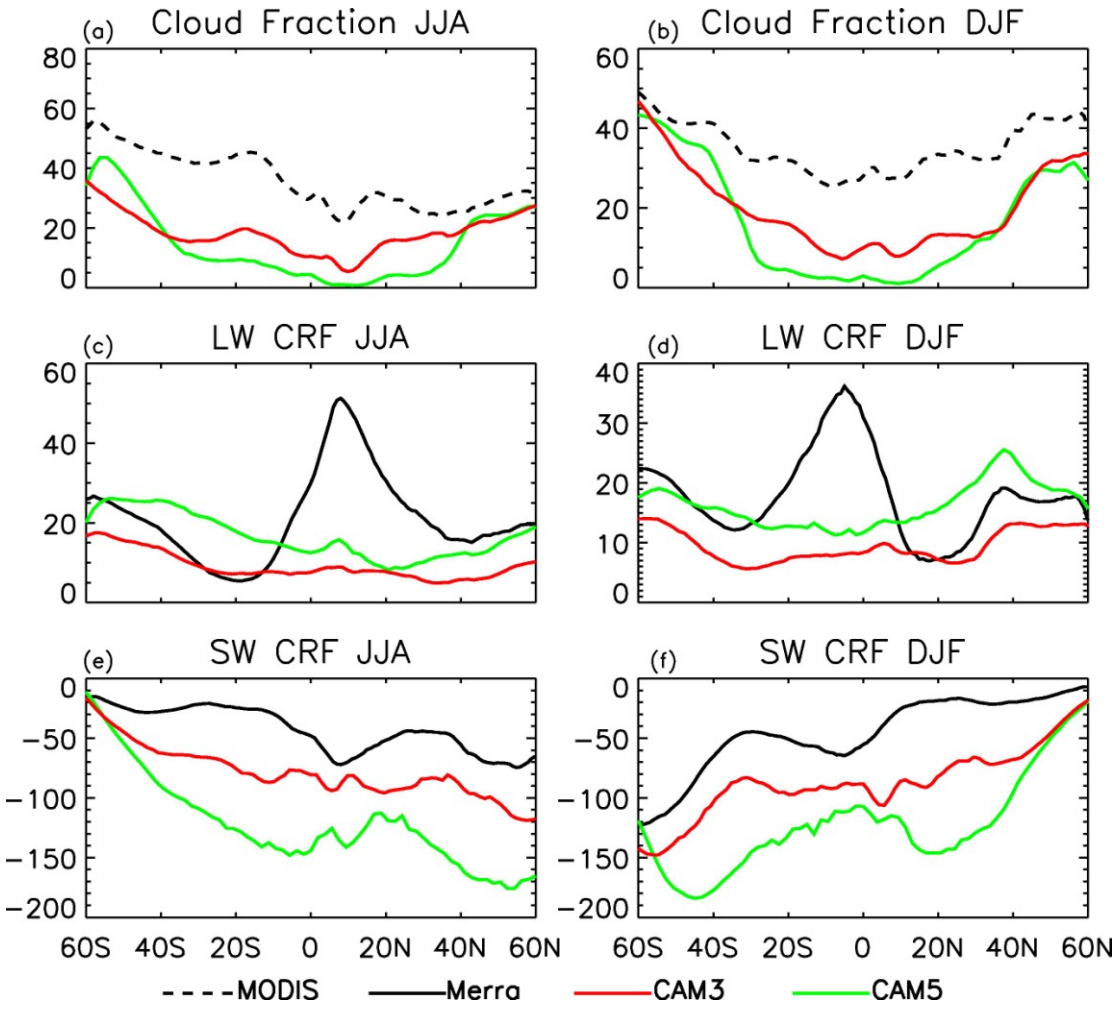

Fig. 4.4 Same as Fig. 4.1 except for low cloud only.

simulations. Systematic overestimations of the SW CRF magnitude are observed for both models, but CAM5 transitions from the largest to smallest magnitude sharply poleward of southern 40º in DJF. Taking into account larger cloud fraction in middle clouds, the contribution to the southern midlatitude SW CRF bias in DJF is comparable to that of high cloud.

Compensations of cloud fraction are seen in low cloud (Fig. 4.4). While CAM5 simulates the largest amount of high cloud, it shows the smallest amount of low clouds. The grand mean of JJA low clouds is 18% and 14% in CAM3 and CAM5, respectively, and the MODIS measurement is 36%. The underestimation of low cloud fraction may either due to shielding of excessive high clouds, or due to intrinsic model biases. The zonally averaged patterns of CRFs are analogous to that of middle clouds. Again a sharp decrease in SW magnitude is observed in CAM5 DJF simulation for southern midlatitude, but apparently it is not responsible for the total error.

We next examine the cloud fraction and CRFs for each individual high cloud type stratified against τ. Cirrus fraction in MODIS shows a bell shape with peak in northern tropics, and decreases poleward gradually (Fig. 4.5 (a), (b)). Cirrus fraction poleward of 40º is very small. CAM3 demonstrates a similar pattern but with nearly twice magnitude in the tropics. The overestimation by CAM5 is more obvious. Anomalous midlatitude maxima are observed in local winter accompanied by exaggerated fluctuations. Both models are able to represent the variations of CRFs, but tend to underestimate the magnitudes, except at the northern tropics in DJF. SW CRF in MERRA shows abnormally strong minima at southern midlatitude in DJF. This is very likely to be

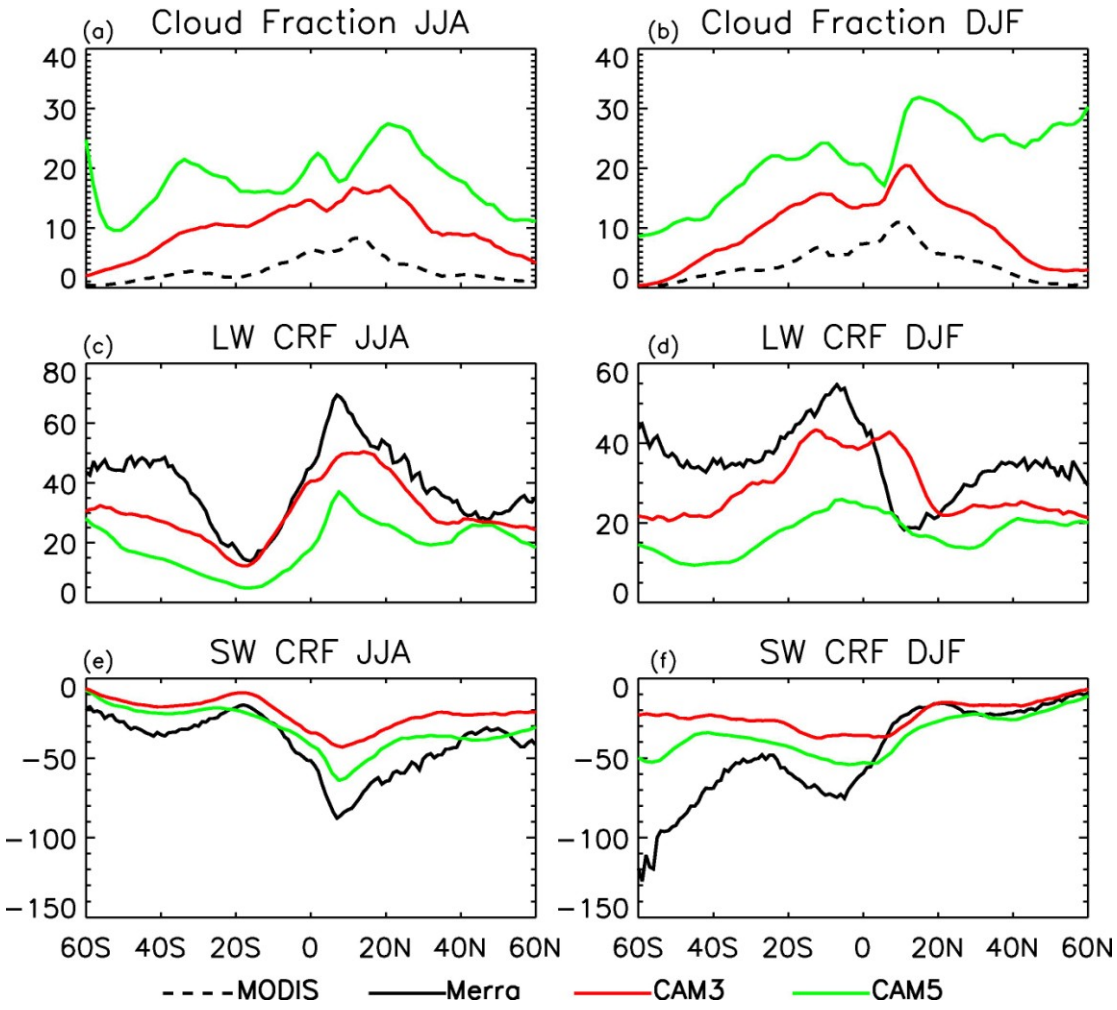

Fig. 4.5 Same as Fig. 4.1 except for cirrus cloud only.

biased due to both collocation problems between the two datasets and low occurrence of cirrus clouds, though we do not expect significant inherited bias to that of high cloud.

Cirrus frequently lies above lower clouds, and thin cirrus with τ less than 1 are often not detectable by MODIS instruments (Dessler and Yang 2003). Therefore, we perform a sensitivity study with cutoff value of 0.9 in the ISCCP simulator. Fig. 4.6 indicates that with a larger cutoff value, a general decrease of cirrus fraction is observed, as large as 11.9% around northern subtropics in DJF. However, visual inspection indicates that changing this factor alone is not sufficient to account for differences compared to MODIS. Zhang et al. (2005) investigated the frequency differences of high thin clouds with varying cutoff values and reported that the sensitivity is large when the value is below 0.1. An examination of total cloud properties indicates negligible impact with the variations of the cutoff value.

Fig. 4.7 compares model cirrostratus with satellite observations. In the tropics from 20ºS to 20ºN, CAM3 agrees well with MODIS. Poleward of 20º, CAM3 tends to underestimate cirrostratus fraction. CAM5 indicates an overestimation in the tropics and underestimation poleward of 20º. LW CRF in CAM3 and CAM5 indicates an overestimation and underestimation with respect to reanalysis by about 10 Wm^{-2} on averaged, respectively.

Fraction of deep convective clouds in CAM3 corresponds well with MODIS, but it is poorly simulated by CAM5 (Fig. 4.8). Poleward of 40º, fractional coverage in CAM5 is extremely small except in JJA northern midlatitude. While overall both models overestimate the magnitudes of CRFs, CAM5 tends to show a better agreement in LW

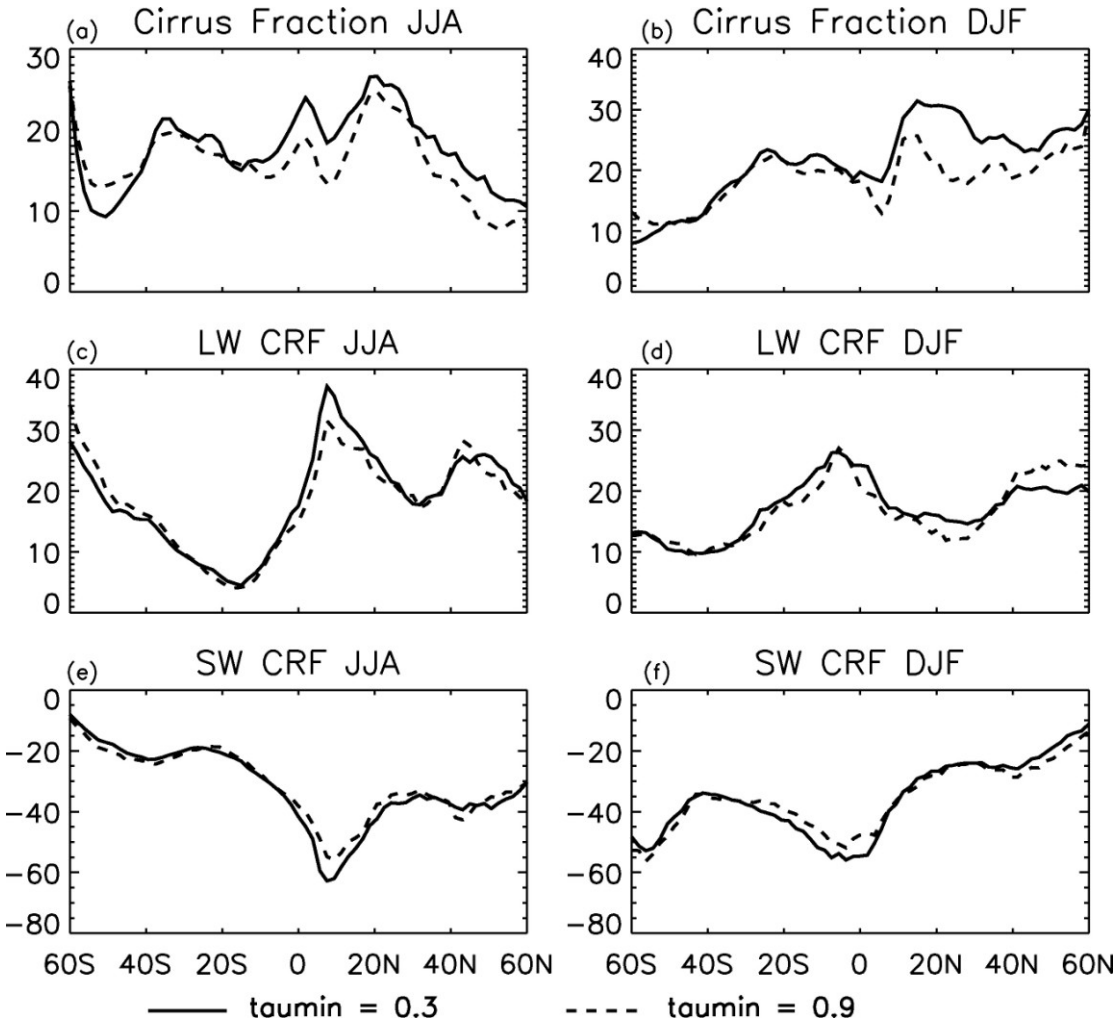

Fig. 4.6 Zonal mean of cirrus cloud fraction and CRFs computed from one year (2003) CAM5 run with two different cutoff values of optical thickness in the ISCCP simulator. Solid line corresponds to value of 0.3, and dash line corresponds to 0.9.

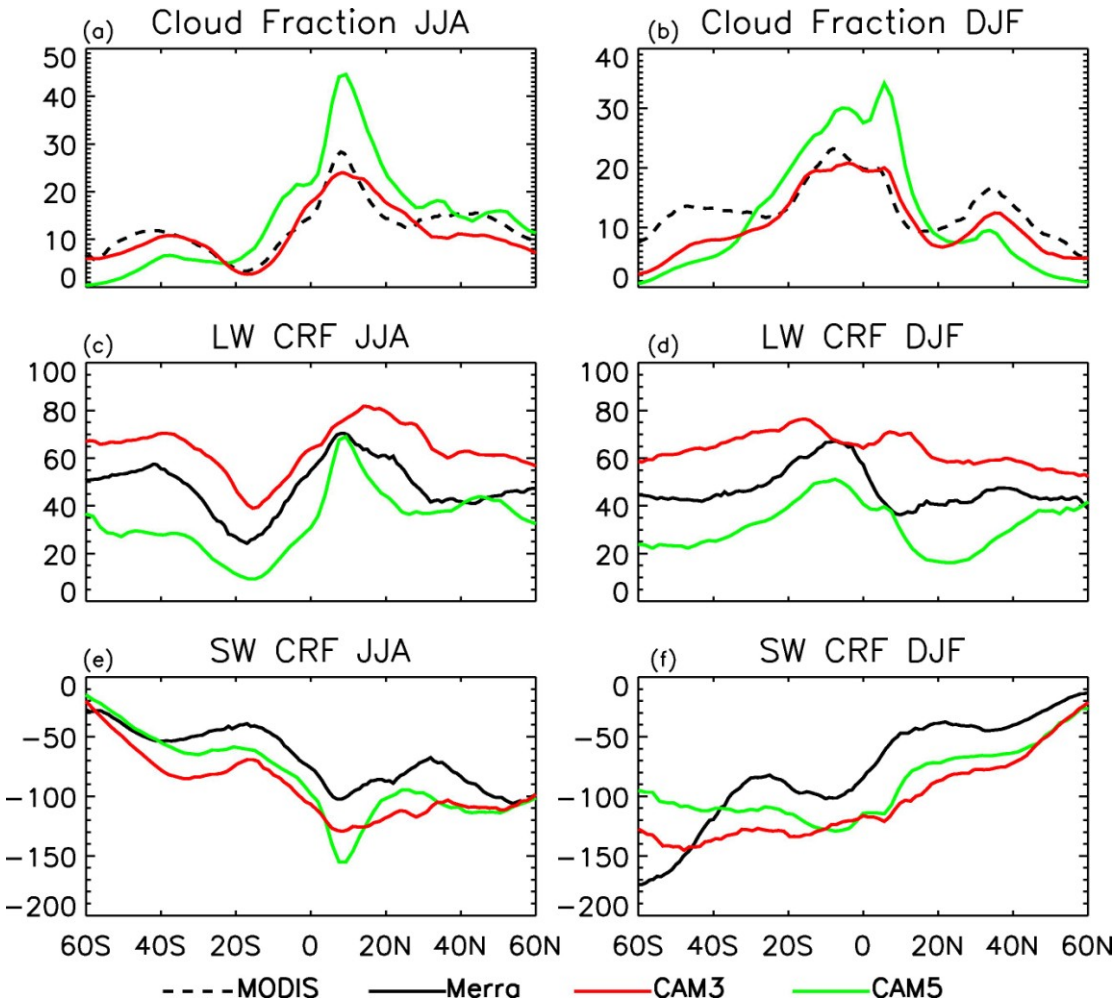

Fig. 4.7 Same as Fig. 4.1 except for cirrostratus only.

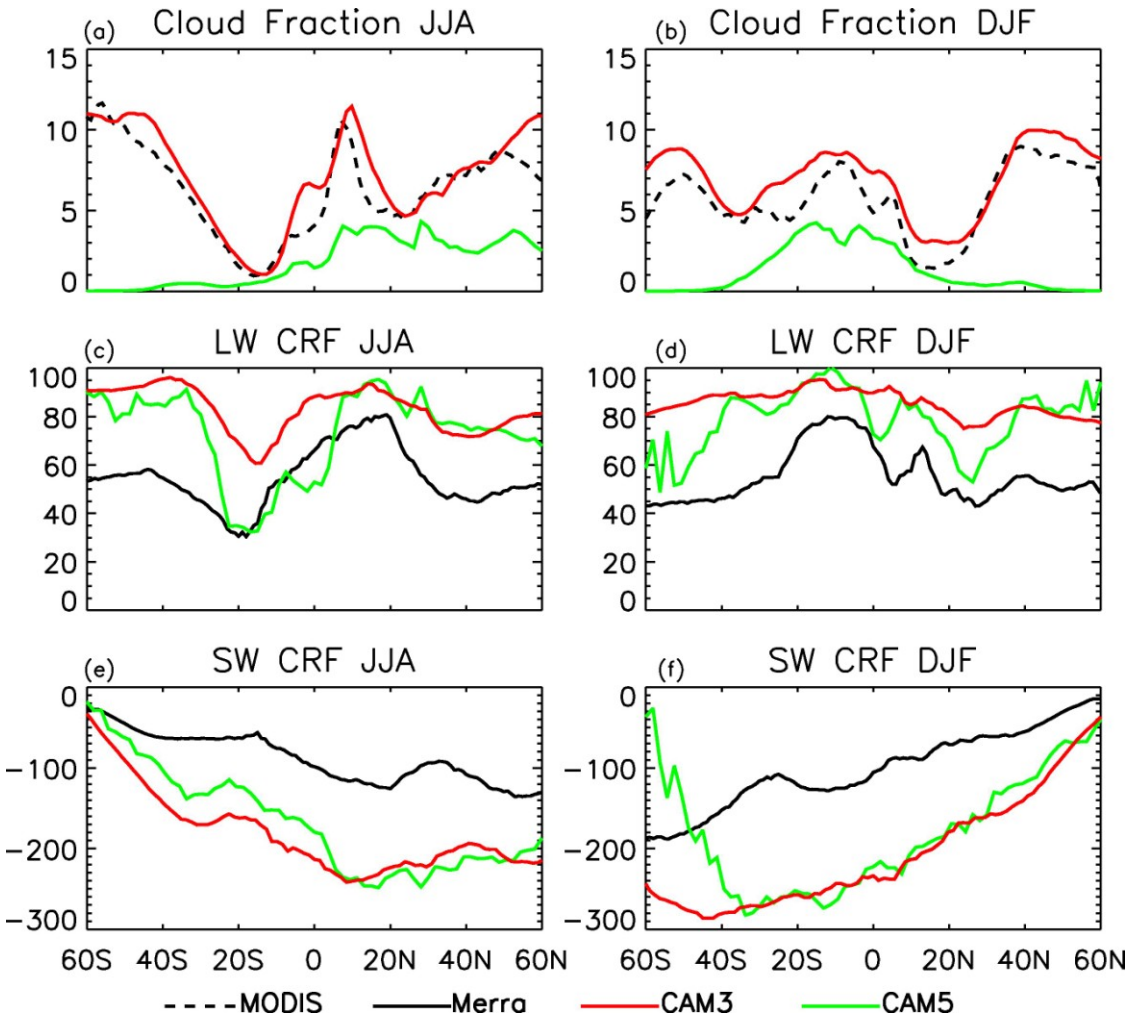

Fig. 4.8 Same as Fig. 4.1 except for deep convective cloud only.

CRF. Note that due to extremely rare occurrence, SW CRF magnitude poleward of 40ºS in CAM5 is significantly biased.

In summary, models simulate excessive high clouds, primarily due to overestimation of cirrus clouds. Although CAM5 shows a better agreement in total cloud properties, except the SW CRF bias in DJF, the compensation error are more pronounced. In general, CAM3 does better for subtype clouds. CAM5 predicts the greatest amount of high thin clouds, which contributes a proportion of SW CRF related to high clouds. However, the significant southern midlatitude SW bias in DJF essentially due to underestimation of the magnitudes of both cirrostratus and deep convective cloud fraction-weighted SW CRFs.

4.5.2 Spatial distributions

We next examine the spatial distributions of cloud properties to investigate whether biases in models are caused by a widespread poor estimation or biases in specific regions. Fig. 4.9 shows the observed and simulated total cloud fraction and CRFs in DJF. While both models capture the maximum cloud bands in the tropics and in the midlatitude storm tracks, CAM3 differs substantially in the total amount from MODIS. Simulation by CAM5 indicates a general improvement in estimating the magnitude of cloud fraction. The features of the LW CRF distribution in MERRA are closely represented by both models (Fig. 4.9(d)-(f)). However, the tropical Indian-west Pacific peak is exaggerated in CAM3. Fig. 4.9(i) shows that the SW CRF bias in CAM5 is due to a widespread underestimation of the magnitude in the southern midlatitude.

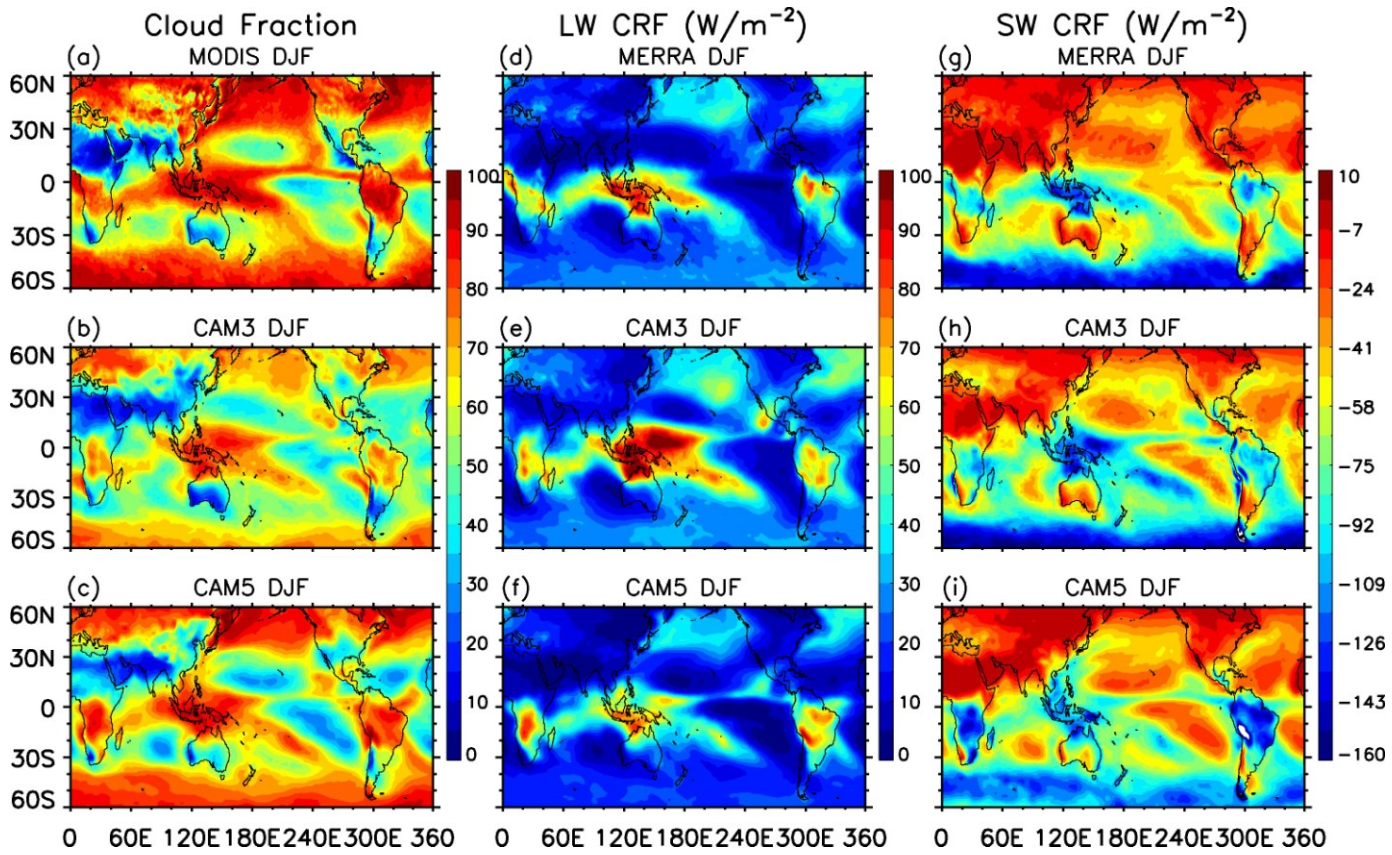

Fig. 4.9 Geographical distributions of cloud fraction and CRFs for total cloud in DJF.

Additional feature include overestimation of the magnitude over the tropical South Africa and South America.

Some major discrepancies noted for high cloud (Fig. 4.10) include overestimation of cloud fraction over Africa and South America by CAM5, an overall exaggeration of LW CRF and sporadic magnification of southern midlatitude SW CRF minima in CAM3. CAM5 are nearly unable to capture midlatitude LW CRF maxima and southern midlatitude SW CRF minima.

The differences observed for high cloud are amplified for individual subtypes, in particular cirrus and deep convective clouds (Fig. 4.11-4.13). Whereas cirrus in MODIS concentrates over the north Africa, the western Pacific and tropical North America, a broader distribution of larger values is seen from CAM3 (Fig. 4.11(a) and (b)). A worse estimation is observed in CAM5, where significant biases are observed over the north Africa, southeast China, North America and east of South America (Fig. 4.11(c)). Apparent compensation errors are seen for deep convective clouds (Fig. 4.13 (a)-(c)). CAM5 is unable to capture midlatitude maxima and peaks over the tropical oceans, while CAM3 does well with the distribution but an overall overestimation in magnitude. Comparatively, a better simulation in both spatial distribution and magnitude is shown for cirrostratus (Fig. 4.12).

In JJA season, tropical cloud systems shift northward (Fig. 4.14(a)-(c)). Unlike widespread minima in DJF SW CRF over southern midlatitude (Fig. 4.9(g)), minima in JJA are concentrated in the north Pacific and north Atlantic (Fig. 4.14(g)). It also appears that an exaggerated spatial coverage of minima by CAM5 compensates for the

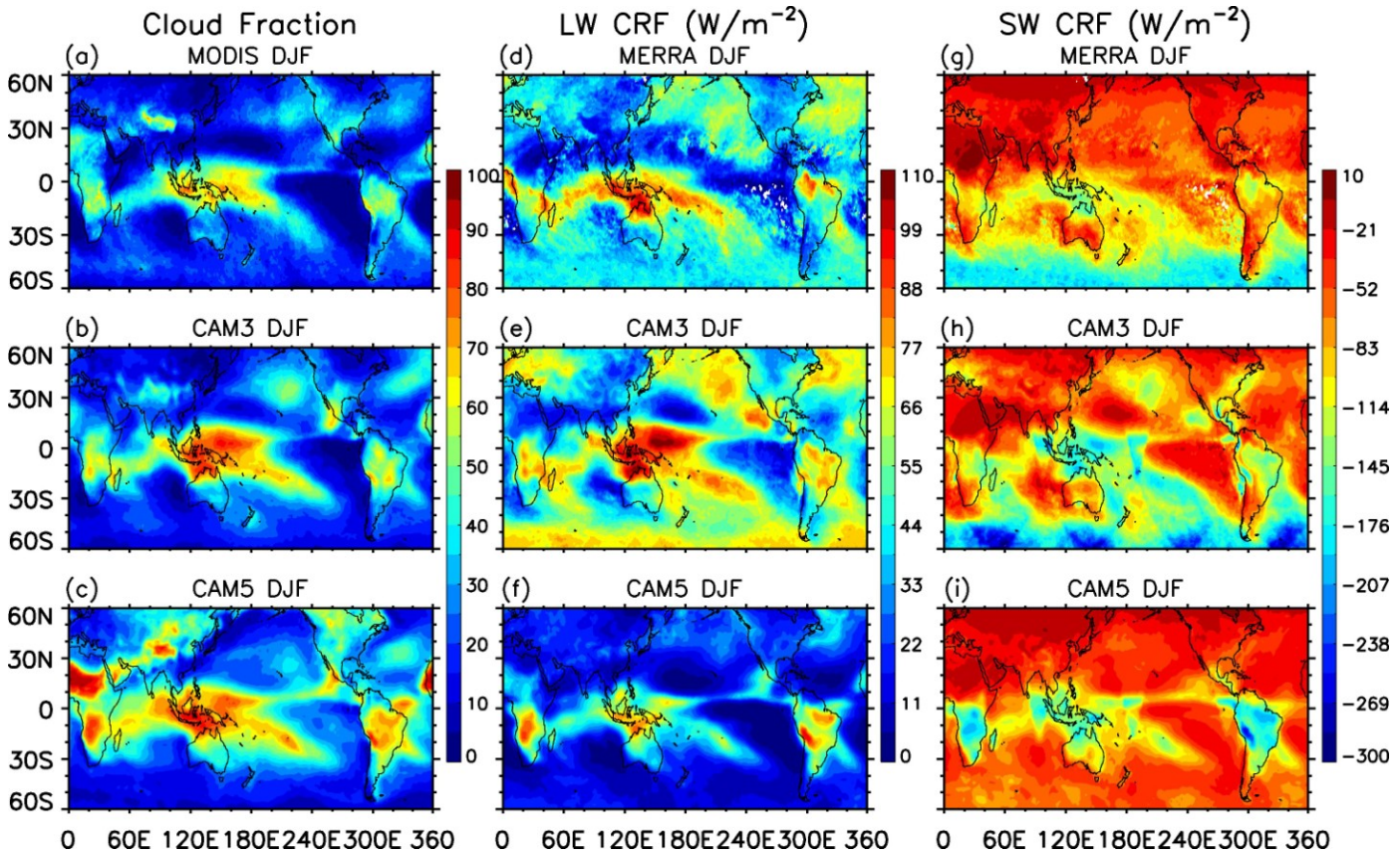

Fig. 4.10 Same as Fig. 4.9 except for high cloud only.

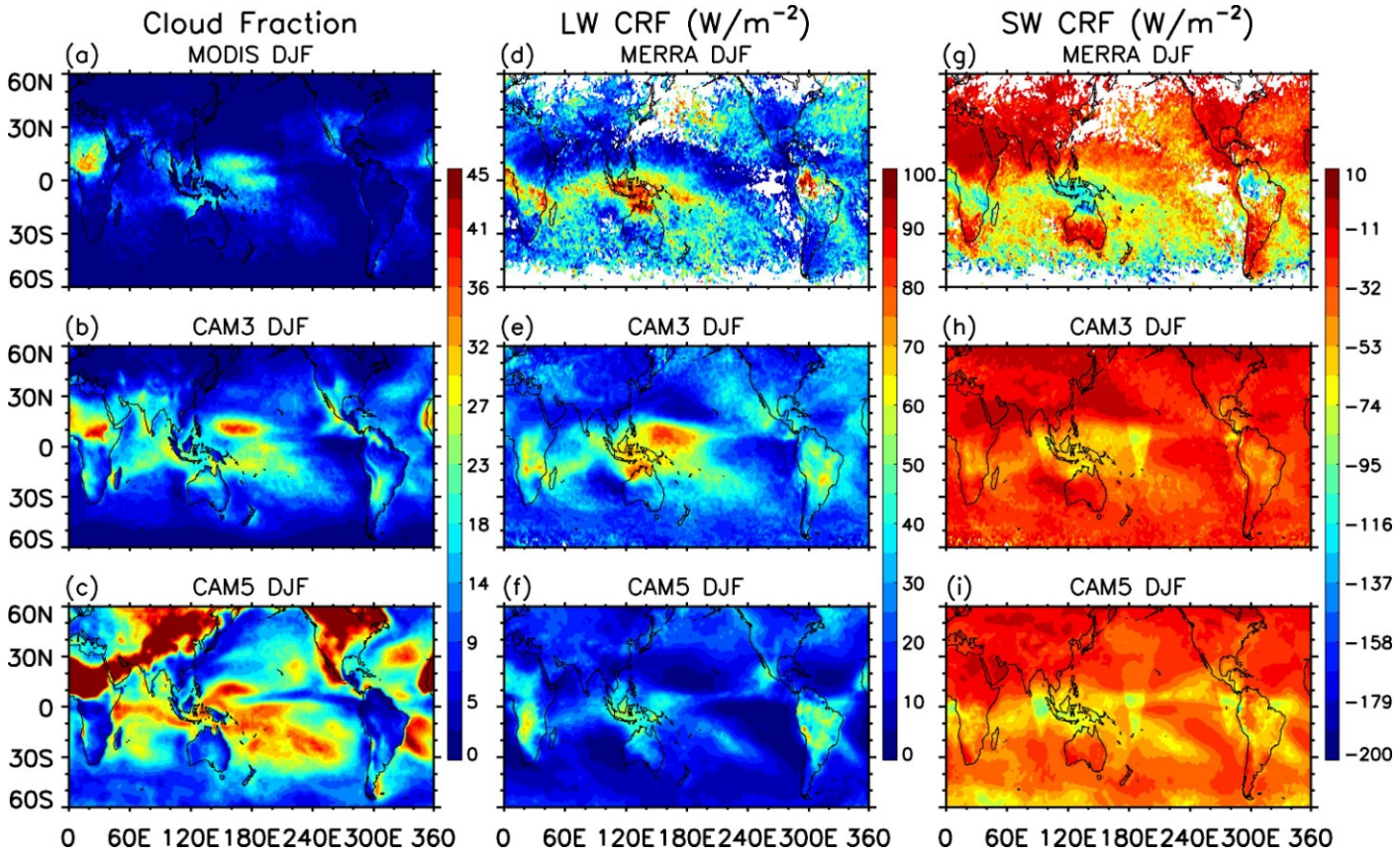

Fig. 4.11 Same as Fig. 4.9 except for cirrus cloud only.

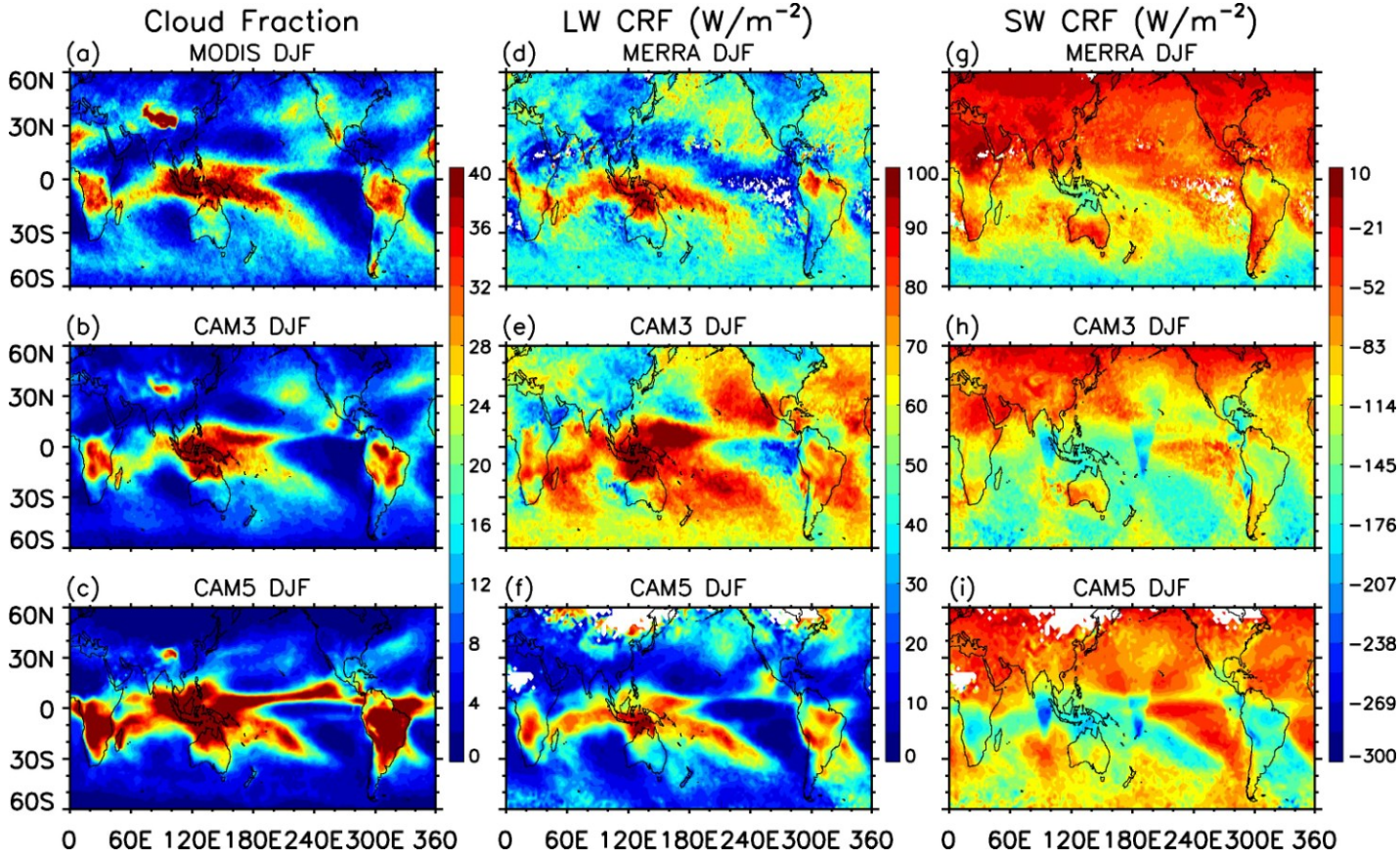

Fig. 4.12 Same as Fig. 4.9 except for cirrostratus only.

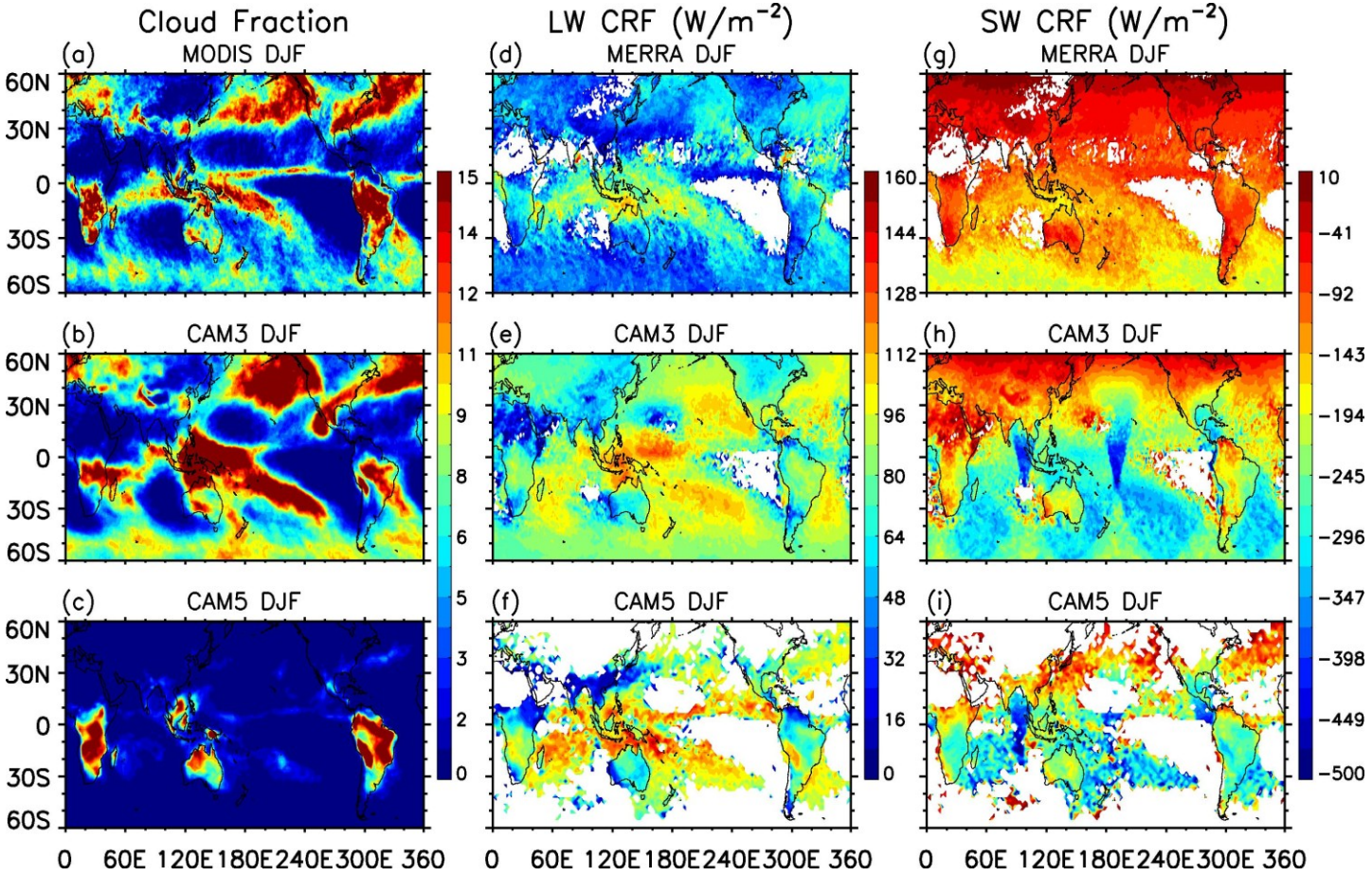

Fig. 4.13 Same as Fig. 4.9 except for deep convective cloud only.

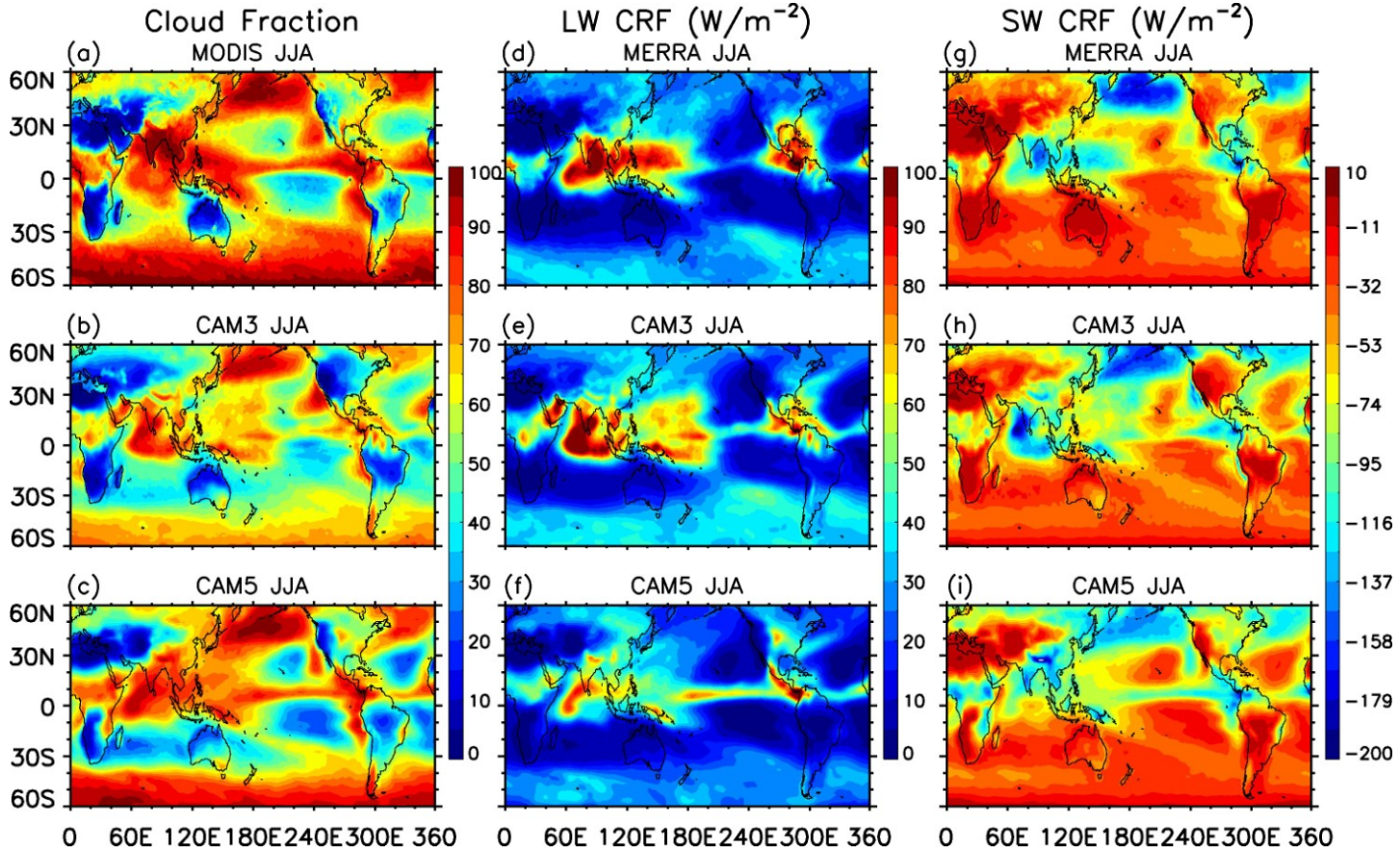

Fig. 4.14 Geographical distributions of total cloud fraction and CRFs in JJA.

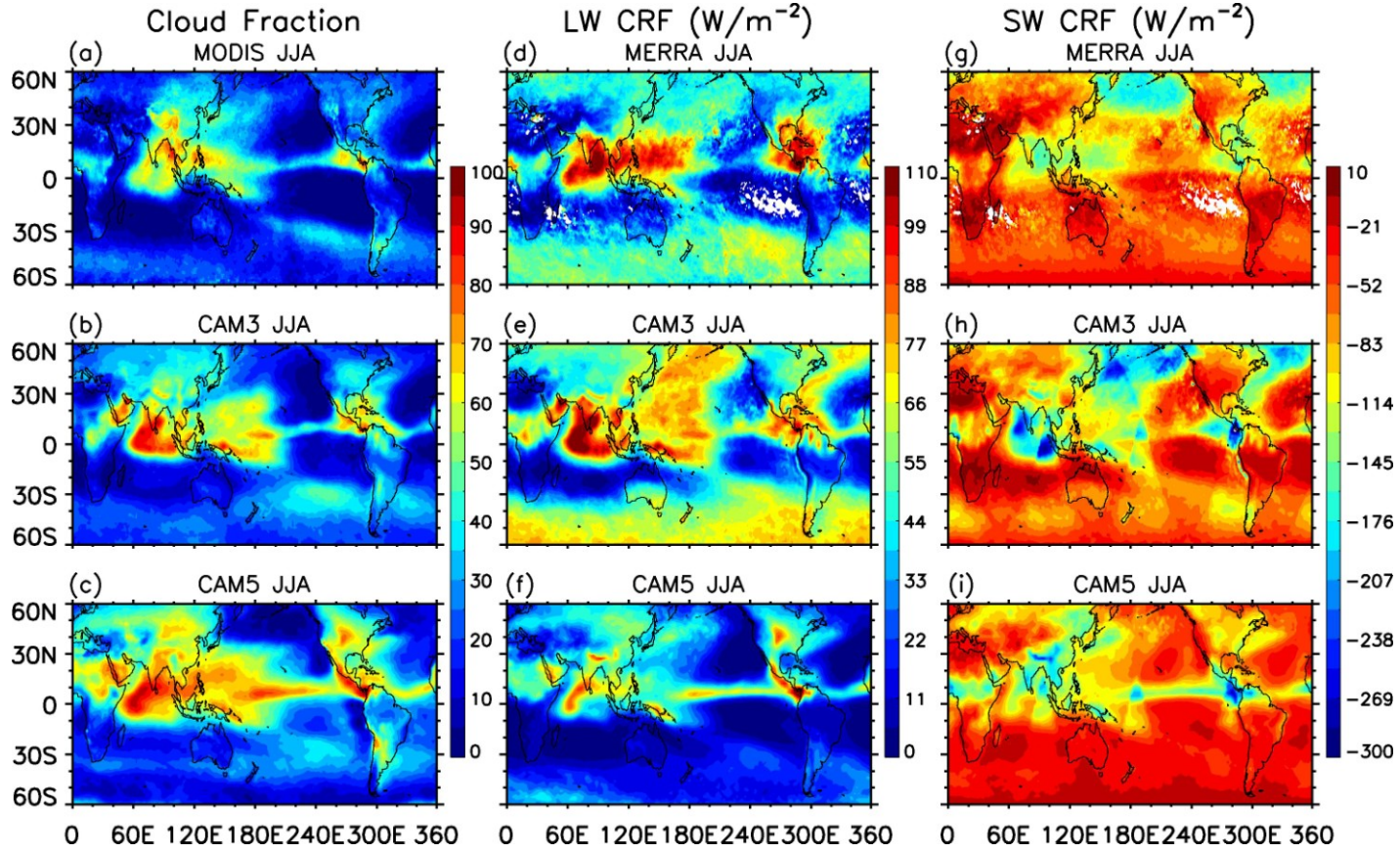

Fig. 4.15 Same as Fig. 4.14 except for high cloud only.

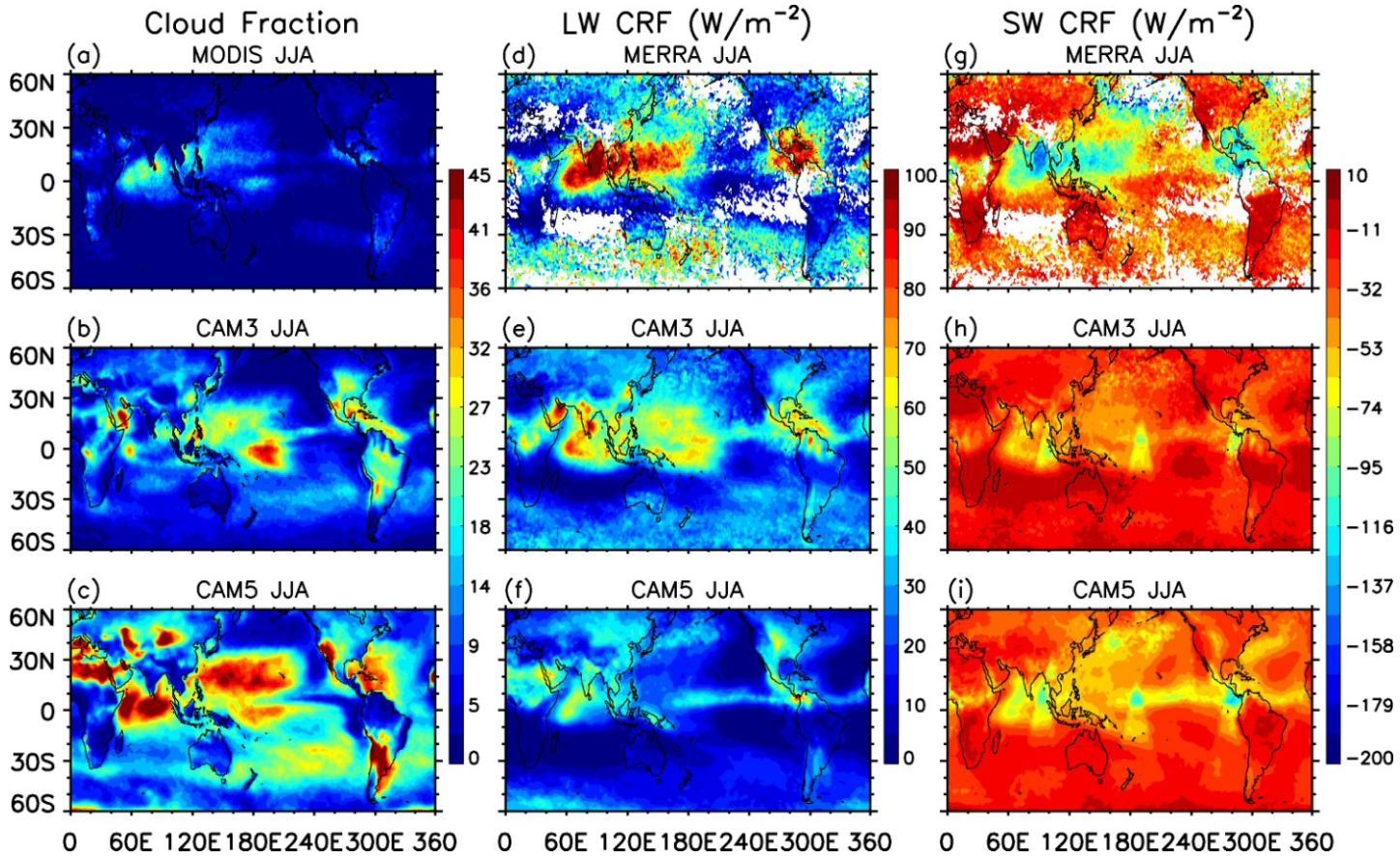

Fig. 4.16 Same as Fig. 4.14 except for cirrus only.

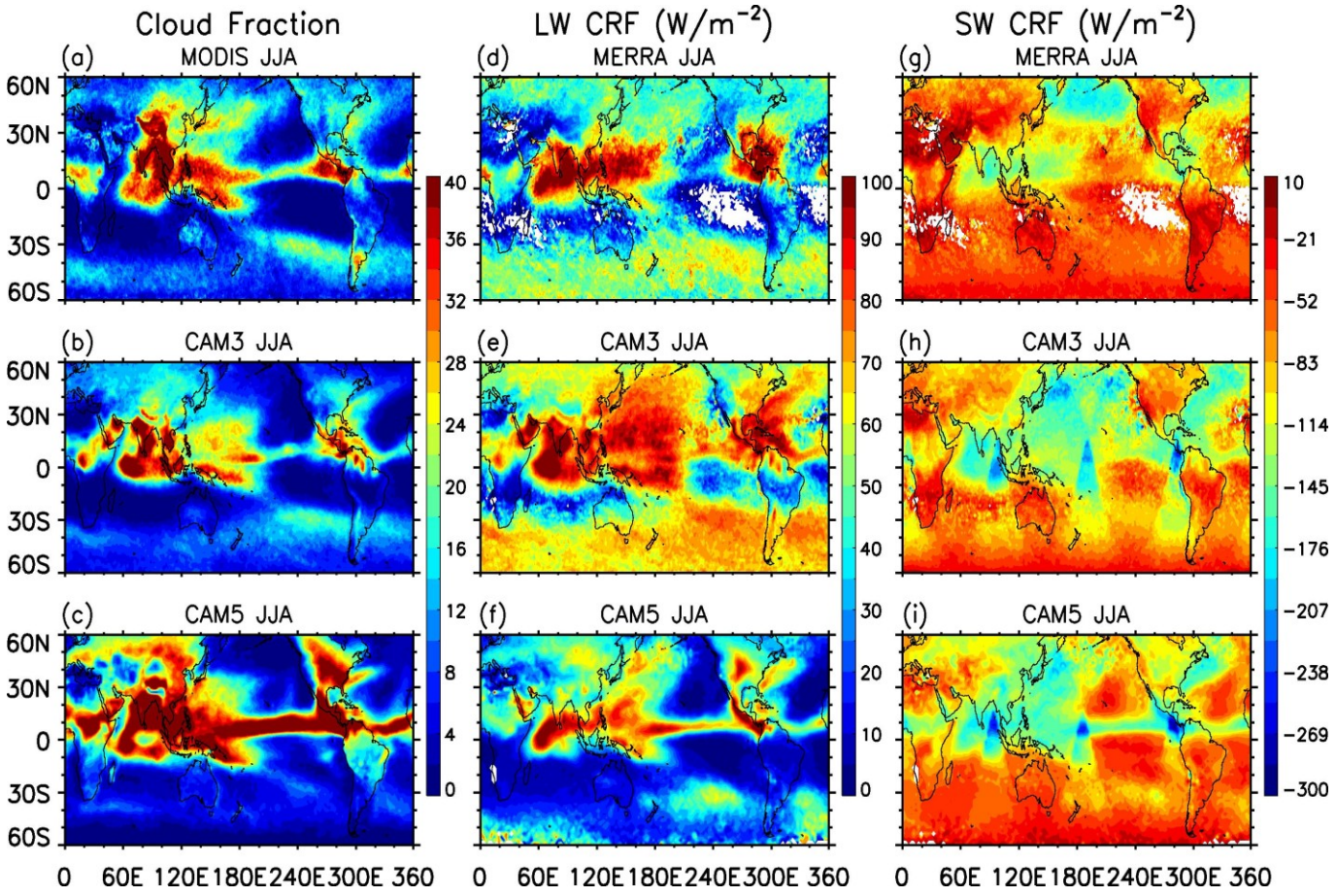

Fig. 4.17 Same as Fig. 4.14 except for cirrostratus only.

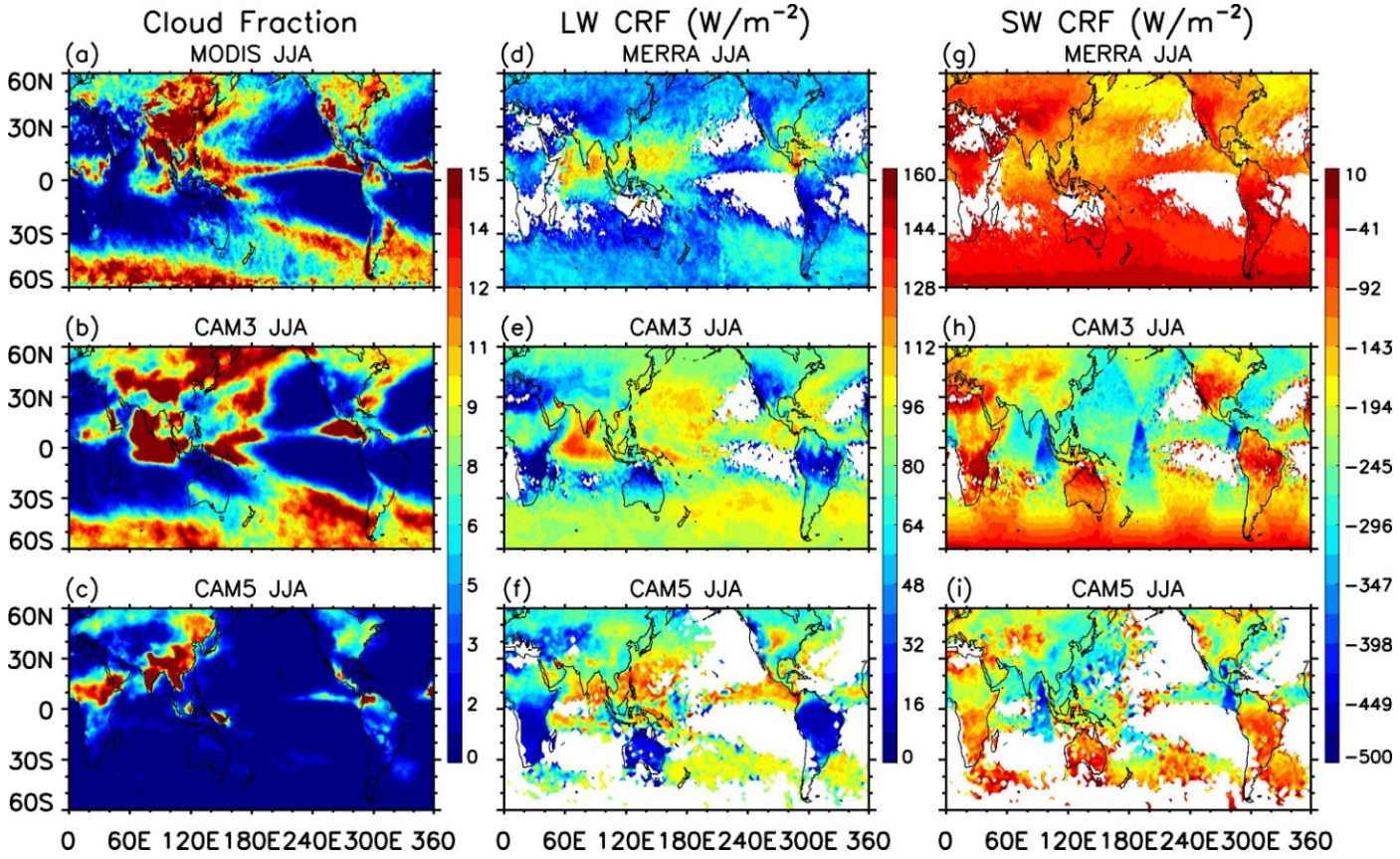

Fig. 4.18 Same as Fig. 4.14 except for deep convective cloud only.

underestimation of SW CRF magnitude (Fig. 4.14(i)). CAM5 captures the general distribution of northern midlatitude LW CRF associated with high cloud but not the southern counterpart (Fig. 4.15(f)). Analogous to DJF, major discrepancies and compensations errors are observed for cirrus and deep convective clouds (Fig. 4.16, 4.18), whereas the model estimated cirrostratus is apparently better (Fig. 4.17).

4.6 Summary and discussion

This study highlights that despite the decades-long research after the AMIP I project, great uncertainties still exist in the parameterization of clouds in GCMs. In this chapter, we compared cloud fraction and radiative properties from two versions of the NCAR CAM models against MODIS cloud observations and MERRA radiation budget. CAM5 in general demonstrates better consistency in estimating total cloud fraction and CRFs than CAM3. However, a significant underestimation of DJF SW CRF poleward of 40ºS is observed in CAM5 by as much 50 W m^{-2}, whereas CAM3 simulation agrees well with MERRA. Investigation of three types of clouds with different top heights indicates that high and middle top clouds are nearly equally responsible for the bias. Further separation of high clouds into optically thin, intermediate and thick clouds shows that the underestimation of the magnitude of fraction-weighted SW CRF associated with cirrostratus and deep convective clouds primarily accounts for the DJF SW bias in CAM5. Examination of the spatial distribution shows that the DJF SW bias poleward of 40ºS is caused by a widespread underestimation of the magnitude.

Various compensation errors are found in both models, which appear to be more pronounced in CAM5. High cloud related compensation errors are more apparent in thin and thick clouds than medium thick clouds. CAM5 overestimates cirrus fraction, but significantly underestimate deep convective clouds, especially in midlatitudes. CAM3 does better in estimating cirrus and deep convective cloud fraction, in particular the latter.

We wish to raise several uncertainties in the interpretation of the results. First, it is a known problem for satellite observations to retrieve cloud tops when a thin high cloud is overlapped with thicker lower clouds. Therefore we have less confidence in optically thin high clouds in inferring models biases. Second, the collocation between MODIS and MERRA may affect the results in the classification of individual cloud types, since these two are essentially independent products in terms of clouds. Third, models runs with different resolutions, and changes to the ISCCP simulator may also cause changes in the simulations. However, we believe that none of these alters the nature of the model biases relative to MODIS and MERRA. In particular, we speculate that the overall improvement in estimating total cloud properties, SW bias in DJF over southern midlatitude, and more pronounced compensation errors by CAM5 are primarily due to the changes to the model, including but not limited to the cloud-related physical schemes, compared to the aforementioned uncertainties.

While it is beyond the scope of this study to investigate the fundamental reasons accounting for model biases, we will pursue it in further studies. For example, we will compare absorbed solar radiation in both clear and cloud-sky conditions between

observations and simulations. We will also investigate the deep and shallow convection schemes in CAM3 and CAM5 to explore the mechanism that accounts for the significant reduction of deep convective clouds in the latter.

CHAPTER V

SUMMARY

Representation of high clouds in climate models is subject to substantial uncertainties associated with both lack of accurate observational constraints and primitive parameterization schemes. A proper understanding of high clouds requires understanding of their dynamical, optical, radiative, macrophysical and microphysical properties. This dissertation utilizes satellite observed cloud properties to investigate equatorial wave signals, examine the fixed anvil temperature (FAT) hypothesis, and evaluate the capability of two climate models in simulating high clouds.

In Chapter II, we have attempted to isolate convectively coupled equatorial wave (CCEW) signals from MODIS cloud-top properties. Unlike previous studies (Wheeler and Kiladis 1999; Cho et al. 2002), which used OLR or precipitation to indirectly approximate tropical convection, we utilize more than six years of cloud top temperature (CTT) retrievals from the MODIS instrument onboard EOS Aqua satellite. Consistent with previous studies, various equatorial wave modes are identified, such as Kelvin wave, $n = 1$ equatorial Rossby and MRG waves, $n = 0$ EIG and $n = 1$ IG waves, and the MJO. Signals related to tropical depressions (easterly waves), which play an important role in the genesis and formation of tropical cyclones, are also uncovered. Additionally, the successful isolation of equatorial wave modes from cirrus optical thickness, retrieved from cirrus reflectance, indicates that robust convection signals exist in cirrus clouds. This confirms previous studies showing that convective blowoff is one of the major

generating mechanisms for cirrus clouds in the upper troposphere. Hence, the study on the interactions between cirrus clouds and CCEWs provides insights to better represent upper thin clouds in climate models.

To test the FAT hypothesis, we have examined the vertical profiles and spatial distributions of water vapor, clear-sky cooling rates, static stability and diabatic subsidence and convergence in Chapter III. The peak clear-sky diabatic subsidence, convergence and cloud fraction profiles are located at roughly the same level (200 hPa). We also show that the maxima in the geographical distributions of tropospheric water vapor agree well with that of clear-sky radiative cooling rates, diabatic subsidence, convergence, and cloud fraction at 200 hPa, consistent with the physical mechanism of the FAT hypothesis.

A common interpretation of this hypothesis is that tropical convective CTT should remain approximately constant as climate warms (Xu et al. 2005, 2007; Eitzen et al. 2009; Zelinka and Hartmann 2010). To compare with previous studies, we utilize CTT retrievals related to high cloud to investigate the variations of CTT in response to ENSO in different regions. Linear square regression is also employed to test the sensitivity of CTT to sea surface temperature (SST). The relationship varies with regions, primarily due to the dynamic effect. Over tropical Indian ocean and west Pacific, the relationship is positive, whereas over other regions it is primarily negative. Averaged over the entire tropics, an overall negative relationship is discovered. We conclude that the FAT hypothesis is more applicable to the tropics as a whole so that the dynamic effects can be suppressed. We suggest interpreting the FAT hypothesis, and the more recent

proportionately higher anvil temperature (PHAT) hypothesis proposed by Zelinka and Hartmann (2010), by using the temperature at the maximum cloud detrainment level instead of the CTT, because satellite sensors attempt to locate the cloud top, which may be higher and colder due to a non-negligible amount of clouds above the maximum detrainment level.

In Chapter IV, we have evaluated cloud fraction and radiative properties from two versions of the NCAR CAM models against MODIS cloud properties and MERRA reanalysis product. An overall improvement in total cloud properties is observed in CAM5 compared to CAM3. However, an apparent underestimation of the magnitude of shortwave (SW) cloud radiative forcing (CRF) in CAM5 is observed in boreal winter southern midlatitude, which is captured well by CAM3. Examination of clouds with different top heights indicates that both high and middle-top clouds account for the bias. Further investigation of three types of high clouds stratified against cloud optical thickness demonstrates that fraction-weighted SW CRFs related to both intermediate and thick high clouds are responsible for the bias. Additionally, appreciable compensation errors are observed in both models, particularly in CAM5. Both models overestimate high cloud fraction, primarily due to overestimation of high thin cloud. While CAM3 agrees well with satellite observations in deep convective cloud fraction, underestimation in CAM5 is significant. To understand the fundamental reasons that account for the biases and compensation errors, further studies are needed to investigate the cloud convection and radiative parameterization schemes in models.

REFERENCES

Baldwin, M. P, L. J. Gray, T. J. Dunkerton, K. Hamilton, P. H. Haynes, and Coauthors, 2001: The quasi-biennial oscillation. *Rev. Geophys.*, **39**, 179-229.

Bony, S., J.-L. Dufresne, H. Le Treut, J.-J. Morcrette, and C. Senior, 2004: On dynamic and thermodynamic components of cloud changes, *Climate. Dyn.*, **22**, 71–86.

Cess, R. D., G. L. Potter, J. P. Blanchet, G. J. Boer, A. D. Del Genio, and Coauthors, 1990: Intercomparison and interpretation of climate feedback processes in 19 atmospheric general circulation models. *J. Geophys. Res.*, **95**, 16,601–16,615.

——, M. H. Zhang, W. J. Ingram, G. L. Potter, V. Alekseev, and Coauthors, 1996: Cloud feedback in atmospheric general circulation models: An update, *J. Geophys. Res.*, **101**, 12,791–12,794, doi:10.1029/96JD00822.

Chae, J. H., S. C. Sherwood, 2010: Insights into cloud-top height and dynamics from the seasonal cycle of cloud-top heights observed by MISR in the west Pacific region. *J. Atmos. Sci.*, **67**, 248–261.

Chang, C. P., 1970: Westward propagating cloud patterns in the tropical Pacific as seen from time composite satellite photographs. *J. Atmos. Sci.*, **27**, 133-138.

Chepfer, H., V. Noel, P. Minnis, D. Baumgardner, L. Nguyen, G. Raga, M. J. McGill, and P. Yang, 2005: Particle habit in tropical ice clouds during CRYSTAL-FACE: Comparison of two remote sensing techniques with in situ observations, *J. Geophys. Res.*,**110**, D16204, doi:16210.11029/12004JD005455.

Cho, H. K., K. P. Bowman, and G. R. North, 2004: Equatorial waves including the Madden-Julian Oscillation in TRMM rainfall and OLR data. *J. Climate*, **17**, 4387-4406.

Collins, W., P. J. Rasch, B. A. Boville, J. J. Hack, J. R. McCaa, and Coauthors, 2004: Description of the NCAR Community Atmospheric Model (CAM3). [Available online at http://www.ccsm.ucar.edu/models/atm-cam/docs/cam2.0/description.pdf.]

Del Genio, A. D., M.-S. Yao, W. Kovari, and K. K.-W. Lo, 1996: A prognostic cloud water parameterization for global climate models. *J. Climate*, **9**, 270–304.

Derber, J. C., D. F. Parrish, and S. J. Lord, 1991: The new global operational analysis system at the National Meteorological Center. *Wea. Forecasting*, **6**, 538-547.

Dessler, A. E., and P. Yang, 2003: The distribution of tropical thin cirrus clouds inferred from Terra MODIS data. *J. Climate*, **16**, 1241–1247.

——, 2010: A determination of the cloud feedback from climate variations over the past decade, *Science*, **330**, 1523-1527, doi: 10.1126/science.1192546.

Dunn, G. E., 1940: Cyclogenesis in the tropical Atlantic. *Bull. Amer. Meteor. Soc*., **21**, 215-229.

Ebert, E. E., and J. A. Curry, 1992: A parameterization of ice cloud optical properties for climate models, *J. Geophys. Res*., **97**, 3831–3836.

Eguchi, N., and M. Shiotani, 2004: Intraseasonal variations of water vapor and cirrus clouds in the tropical upper troposphere, *J. Geophys. Res.*, **109**, D12106, doi:10.1029/2003JD004314.

Eitzen, Z. A., K.-M. Xu, and T. Wong, 2009: Cloud and radiative characteristics of tropical deep convective systems in extended cloud objects from CERES observations. *J. Climate*, **22**, 5983–6000.

Folkins, I., K. K. Kelly, and E. M. Weinstock, 2002: A simple explanation for the 11 to 15 km increase in tropical relative humidity, *J. Geophys. Res*., **107**, 4736, doi: 10.1029/2002JD002185.

Fu, Q., and K. N. Liou, 1992: On the correlated k-distribution method for radiative-transfer in nonhomogeneous atmospheres, *J. Atmos. Sci*., **49**, 2139 – 2156.

——, and ——, 1993: Parameterization of the radiative properties of cirrus clouds, *J. Atmos. Sci*., **50**, 2008– 2025.

Fujiwara, M., S. Iwasaki, A. Shimizu, Y. Inai, M. Shiotani, and Coauthors, 2009: Cirrus observations in the tropical tropopause layer over the western Pacific, *J. Geophys. Res.*, **114**, D09304, doi:10.1029/2008JD011040.

Gao, B.-C., K. Meyer, and P. Yang, 2004: A new concept on remote sensing of cirrus optical depth and effective ice particle size using strong water vapor absorption channels near 1.38 and 1.88 um. *IEEE Trans. Geosci. Remote Sens.* **42**, 1891-1899.

Gettelman, A., H. Morrison, and S. J. Ghan, 2008: A new two-moment bulk stratiform cloud microphysics scheme in the NCAR Community Atmosphere Model (CAM3), Part II: Single-columnand global results*, J. Climate*., **21**, 3660–3679.

——, A. X. Liu, S. J. Ghan, H. Morrison, S. Park, A. J. Conley, S. A. Klein, J. Boyle, D. L. Mitchell, and J. L. F. Li, 2010: Global simulations of ice nucleation and ice

supersaturation with an improved cloud scheme in the community atmosphere model, *J. Geophys. Res*., **115**, D18216, doi:10.1029/2009JD013797.

Hack, J. J., 1994: Parameterization of moist convection in the National Center for Atmospheric Research Community Climate Model (CCM2). *J. Geophys. Res*., **99**, 5541–5568.

Hannachi, A., I. T. Jolliffe, and D. B. Stephenson, 2007: Empirical orthogonal functions and related techniques in atmospheric science: A review. *Int. J. Climatol.*, **27**, 1119-1152.

Harrison, E. F., P. Minnis, B. R. Barkstrom, V. Ramanathan, R. D. Cess, and G. G. Gibson, 1990: Seasonal variation of cloud radiative forcing derived from the Earth Radiation Budget Experiment. *J. Geophys. Res*., **95**, 18,687–18,703.

Hartmann, D. L., J. R. Holton, and Q. Fu, 2001a: The heat balance of the tropical tropopause, cirrus, and stratospheric dehydration, *Geophys. Res. Lett.*, **28**, 1969–1972, doi:10.1029/2000GL012833.

——, L. A. Moy, Q. Fu, 2001b: Tropical convection and the energy balance at the top of the atmosphere. *J. Climate*, **14**, 4495–4511.

——, and K. Larson, 2002: An important constraint on tropical cloud–climate feedback. *Geophys. Res. Lett.*, **29,** 1951, doi:10.1029/2002GL015835.

Heidinger, A. K., M. J. Pavolonis, 2009: Gazing at cirrus clouds for 25 years through a split window. Part I: Methodology. *J. Appl. Meteor. Climatol.*, **48**, 1100–1116.

Heymsfield, A. J., K. M. Miller, and J. D. Spinhirne, 1990: The 27-28 October 1986 FIRE IFO cirrus case study: Cloud microstructure, *Mon. Wea. Rev*., **118**, 2313-2328.

——, A. Bansemer, P. R. Field, S. L. Durden, J. L. Stith, J. E. Dye, W. Hall, and C. A. Grainger, 2002: Observations and parameterizations of particle size distributions in deep tropical cirrus and stratiform precipitating clouds: Results from in situ observations in TRMM field campaigns, *J. Atmos. Sci*., **59**, 3457-3491.

Hong, G., P. Yang, B.-C. Gao, B.A. Baum, Y.X. Hu, M.D. King, and S. Platnick, 2007: High cloud properties from three years of MODIS *Terra* and *Aqua* Collection-4 data over the tropics. *J. Appl. Meteor. Climatol.*, **46**, 1840–1856.

Hurrell, J. W., J. J. Hack, D. Shea, J. M. Caron, and J. Rosinski, 2008: A new sea surface temperature and sea ice boundary data set for the Community Atmosphere Model. *J. Climate*, **21**, 5145–5153.

Iacono, M., J. Delamere, E. Mlawer, M. Shephard, S. Clough, and W. Collins, 2008:

Radiative forcing by long-lived greenhouse gases: Calculations with the aer radiative transfer models, *J. Geophys. Res*. **113**, doi:10.1029/2008JD009944.

Jensen, E. J., Owen. B. Toon, H. B. Selkirk, J. D. Spinhirne, and M. R. Schoeberl, 1996: On the formation and persistence of subvisible cirrus clouds near the tropical tropopause, *J. Geophys. Res.*, **101**, 21,361–21,375.

Jin, Y., W. B. Rossow, and D. P. Wylie, 1996: Comparison of the climatologies of high-level clouds from HIRS and ISCCP, *J. Climate*, **9**, 2850–2879.

Kiehl, J. T., J. J. Hack, J. W. Hurrell, 1998: The energy budget of the NCAR Community Climate Model: CCM3. *J. Climate*, **11**, 1151–1178.

Kiladis, G. N., M. C. Wheeler, P. T. Haertel, K. H. Straub, and P. E. Roundy, 2009: Convectively coupled equatorial waves, *Rev. Geophys.*, **47**, RG2003, doi:10.1029/2008RG000266.

King, M. D., Y. J. Kaufman, W. P. Menzel, and D. Tanre, 1992: Remote sensing of cloud, aerosol, and water vapor properties from the Moderate Resolution Imaging Spectrometer (MODIS). *IEEE Trans. Geosci. Remote Sens*., **30**, 2-27.

——, S.-C. Tsay, S. E. Platnick, M. Wang, and K. N. Liou, Cloud retrieval algorithms for MODIS, 1997: Optical thickness, effective particle radius, and thermodynamic phase, MODIS Algorithm Theoretical Basis Document, No. ATBD-MOD-05[at http:Neospso.gsfc.nasa.gov/atbd/modistables.html].

——, W. P. Menzel, Y. J. Kaufman, D. Tanre, B.-C. Gao, S. Platnick, S. A. Ackerman, L. A. Remer, R. Pincus and P. A. Hubanks, 2003: Cloud and aerosol properties, precipitable water, and profiles of temperature and water vapor from MODIS. *IEEE Trans. Geosci. Remote Sens.*, **41**, 442-458.

——, S. Platnick, P. A. Hubanks, G. T. Arnold, E. G. Moody, G. Wind, and B. Wind, 2006: Collection 005 change summary for the MODIS cloud optical property (06_OD) algorithm. [Available online at modis-atmos.gsfc.nasa.gov/C005_ Changes/C005_CloudOpticalProperties_ver311.pdf.]

Klein, S. A. and C. Jakob, 1999: Validation and sensitivities of frontal clouds simulated by the ECMWF model. *Mon. Wea. Rev*., **127**, 2514–2531.

Knutson, T. R., and K. M. Weickmann, 1987: 30-60 day atmospheric oscillation: composite life cycles of convection and circulation anomalies. *Mon. Wea. Rev*., **115**, 1407-1436.

Kuang, Z., D. L. Hartmann, 2007: Testing the fixed anvil temperature hypothesis in a cloud-resolving model. *J. Climate*, **20**, 2051–2057.

Kubar, T. L., D. L. Hartmann, R. Wood, 2007: Radiative and convective driving of tropical high Clouds. *J. Climate*, **20**, 5510–5526.

Li, Y., G. R. North, P. Yang, and B. A. Baum, 2010: Exploration of the MODIS cloud-top property products for the investigation of equatorial wave systems, *J. Appl. Meteor. Climatol.*, ***49***, 2050-2057.

Liebmann, B., and C. A. Smith, 1996: Description of a complete (interpolated) outgoing longwave radiation dataset. *Bull. Amer. Meteor. Soc.*, **77**, 1275-1277.

Lin, J.-L., G. N. Kiladis, B. E. Mapes, K. M. Weickmann, K. R. Sperber, and Coauthors, 2006: Tropical intraseasonal variability in 14 IPCC AR4 climate models. Part I: Convective signals. *J. Climate*, **19**, 2665–2690.

Lin, W. Y., and M. H. Zhang, 2004: Evaluation of clouds and their radiative effects simulated by the NCAR Community Atmospheric Model against satellite observation. *J. Climate*, **17**, 3302-3318.

Liou, K. N. and K. L. Gebhart, 1982: Numerical experiments on the thermal equilibrium temperature in cirrus cloudy atmospheres. *J. Meteor. Soc. Japan*., **60**, 570–582.

——, 1986: Influence of cirrus clouds on weather and climate processes: A global perspective. *Mon. Wea. Rev*., **114**, 1167–1199.

Liu, G., and J. A. Curry, 1999: Tropical ice water amount and its relations to other atmospheric hydrological parameters as inferred from satellite data. *J. Appl. Meteor*., **38**, 1182–1194.

Madden, R., and P. Julian, 1971: Detection of a 40 –50 day oscillation in the zonal wind in the tropical Pacific, *J. Atmos. Sci*., **28**, 702–708.

——, and ——, 1972: Description of global scale circulation cells in the tropics with a 40–50 day period, *J. Atmos. Sci*., **29**, 1109 – 1123.

——, and ——, 1994: Observation of the 40-50 day tropical oscillation-a review. *Mon. Wea. Rev.*, **12**, 814-837.

Matsuno, T., 1966: Quasi-geostrophic motions in the equatorial area. *J. Meteor. Soc. Japan*, **44**, 25-43.

Menzel, W. P., R. Frey, H. Zhang, D. Wylie, C. Moeller, R. Holz, B. Maddux, B. A. Baum, K. Strabala, and L. Gumley, 2008: MODIS global cloud-top pressure and amount estimation: algorithm description and results. *J. Appl. Meteor. Climatol.*, **47**, 1175-1198.

Meyer, K., P. Yang, and B.-C. Gao, 2007: Ice cloud optical depth from MODIS cirrus reflectance. *IEEE Trans. Geosci. Remote Sens*., **4**, 471-474.

Meyer, R., H. Mannstein, R. Meerkötter, U. Schumann, and P. Wendling, 2002: Regional radiative forcing by line-shaped contrails derived from satellite data, *J. Geophys. Res*., **107**, 4104, doi: 10.1029/2001JD000426.

Minnis, P., P. W. Heck, and D. Y. Young, 1993: Inference of cirrus cloud properties using satellite-observed visible and infrared radiances. Part II: Verification of theoretical cirrus radiative properties. *J. Atmos. Sci*., **50**, 1305-1322.

——, D. P. Kratz, J. A. Coakley Jr., M. D. King, D. P. Garber, and Coauthors, 1995: Cloud optical property retrieval (Subsystem 4.3). In Clouds and the Earth's Radiant Energy System (CERES) Algorithm Theoretical Basis Document, volume III: Cloud analyses and radiance inversions (Subsystem 4), NASA RP 1376 vol. 3, edited by CERES Science Team, 135-176.

——, D. P. Garber, D. F. Young, R. F. Arduini, and Y. Takano, 1998: Parameterizations of reflectance and effective emittance for satellite remote sensing of cloud properties. *J. Atmos. Sci*., **55**, 3313–3339.

——, U. Schumann, D. R. Doelling, K. Gierens, and D. W. Fahey, 1999: Global distribution of contrail radiative forcing. *Geophys. Res. Lett*., **26**, 1853-1856.

Minschwaner, K., and A. E. Dessler, 2004: Water vapor feedback in the tropical upper troposphere: Model results and observations, *J. Climate*, **17**, 1272-1282.

Mitchell, D. L., 2000: Parameterization of the Mie extinction and absorption coefficients for water clouds, *J. Atmos. Sci*., **57**, 1311–1326.

——, 2002: Effective diameter in radiation transfer: General definition, applications and limitations, *J. Atmos. Sci*., **59**, 2330–2346.

——, A. J. Baran, W. P. Arnott, and C. Schmitt, 2006: Testing and comparing the modified anomalous diffraction approximation, *J. Atmos. Sci*., **59**, 2330–2346.

Mlawer, E., S. Taubman, P. Brown, M. Iacono, and S. Clough, 1997: Radiative transfer for inhomogeneous atmospheres: RRTM, a validated correlated-k model for the longwave, *J. Geophys. Res*., **102**, 16,663–16,682.

Morrison, H., and A. Gettelman, 2008: A new two-moment bulk stratiform cloud microphysics scheme in the NCAR Community Atmosphere Model (CAM3), Part I: Description and numerical tests, *J. Climate*, **21**, 3642–3659.

Nakajima, T., and M. D. King, 1990: Determination of the optical thickness and effective particle radius of clouds from reflected solar radiation measurements, Part I: Theory, *J. Atmos. Sci*., **47**, 1878-1893.

Nasiri, S. L., B. A. Baum, A. J. Heymsfield, P. Yang, M. R. Poellot, D. P. Kratz, and Y. X. Hu, 2002: The development of midlatitude cirrus models for MODIS using FIRE-I, FIRE-II, and ARM in situ data, *J. Appl. Meteor*., **41**, 197-217.

Norris, J. R., and C. P. Weaver, 2001: Improved techniques for evaluating GCM cloudiness applied to the NCAR CCM3. *J. Climate*, **14**, 2540–2550.

Park, S., and C. S. Bretherton, 2009: The university of washington shallow convection and moist turbulence schemes and their impact on climate simulations with the community atmosphere model, *J. Climate*, **22**, 3449–3469.

Pincus, R., H. W. Barker, and J.-J. Morcrette, 2003: A fast, flexible, approximate technique for computing radiative transfer in inhomogeneous cloud fields. *J. Geophys. Res*., **108**, 4376, doi:10.1029/2002JD003322.

Platnick, S., M. D. King, S. A. Ackerman, W. P. Menzel, B. A. Baum, J. C. Riedi, and R. A. Frey, 2003: The MODIS cloud products: Algorithms and examples from Terra. *IEEE Trans. Geosci. Remote Sens*., **41**, 459-473.

Ponater, M., S. Marquart, and R. Sausen, 2002: Contrails in a comprehensive global climate model: Parameterization and radiative forcing results, *J. Geophys. Res.*, **107**, 4164, doi: 10.1029/2001JD000429.

Ramanathan, V., R. D. Cess, E. F. Harrison, P. Minnis, B. R. Barkstrom, E. Ahmad, and D. Hartmann, 1989: Cloud-radiative forcing and climate: Results from the Earth Radiation Budget Experiment. *Science*, **243**, 57–63.

Randall, D. A., S. Krueger, C. Bretherton, J. Curry, P. Duynkerke, and Coauthors, 2003: Confronting models with data: The GEWEX cloud systems study. *Bull. Amer. Meteor. Soc.*, **84**, 455–469.

——, R. A. Wood, S. Bony, R. Colman, T. Fichefet, and Coauthors, 2007: Climate models and their evaluation, in *Climate Change 2007: The Physical Science Basis. Contribution of Working Group I to the Fourth Assessment Report of the Intergovernmental Panel on Climate Change*, 589-662, edited by S. Solomon, D. Qin, M. Manning, Z. Chen, M. Marquis, and Coauthors. Cambridge Univ. Press, New York.

Rasch, P. J., and J. E. Kristja´nsson, 1998: A comparison of the CCM3 model climate using diagnosed and predicted condensate parameterizations. *J. Climate*, **11**, 1587–1614.

Reed, R. J., and E. E. Recker, 1971: Structure and properties of synoptic-scale wave disturbances in the equatorial western Pacific. *J. Atmos. Sci*., **28**, 1117-1133.

Riehl, H., 1948: On the formation of typhoons. *J. Atmos. Sci*., **5**, 247-265.

Rienecker, M. M., M. J. Suarez, R. Gelaro, R. Todling, J. Bacmeister, and Coauthors, 2011: MERRA: NASA's modern-era retrospective analysis for research and applications. *J. Climate*, **24**, 3624–3648.

Rossow, W. B., and R. A. Schiffer, 1991: ISCCP cloud data products. *Bull. Amer. Meteor. Soc*., **72**, 2-20.

——, and ——, 1999: Advances in understanding clouds from ISCCP. *Bull. Amer. Meteor. Soc.,* **80**, 2261-2287.

Roundy, P. E., and W. M. Frank, 2004: A climatology of waves in the equatorial region. *J. Atmos. Sci.*, **61**, 2105–2132.

——, C. J. Schreck III, 2009: A combined wave-number-frequency and time-extended EOF approach for tracking the progress of modes of large-scale organized tropical convection. *Quart. J. Roy. Meteor. Soc*., **135**, 161-173.

Schiffer, R. A., and W. B. Rossow, 1983: The International Satellite Cloud Climatology Project (ISCCP): The first project of the World Climate Research Programme. *Bull. Amer. Meteor. Soc*., **64**, 779-784.

Slingo, A., 1989: A GCM parameterization for the shortwave radiative properties of clouds, *J. Atmos. Sci*., **46**, 1419–1427.

Soden, B. J., and I. M. Held, 2006: An assessment of climate feedbacks in coupled ocean-atmosphere models, *J. Climate*, **19**, 3354–3360.

Takano, Y., and K. N. Liou, 1995: Radiative transfer in cirrus clouds. Part III: Lightscattering by irregular ice crystals, *J. Atmos. Sci*., **52**, 818-837.

Takayabu, Y. N., 1994: Large-scale cloud disturbances associated with equatorial waves. Part I: Spectral features of the cloud disturbances. *J. Meteor. Soc. Japan*, **72**, 433-448.

Tompkins, A. M., and G. C. Craig, 1999: Sensitivity of tropical convection to sea surface temperature in the absence of large-scale flow. *J. Climate*, **12,** 462–476.

Wallace, J. M., and V. E. Kousky, 1968: Observational evidence of Kelvin waves in the tropical stratosphere. *J. Atmos. Sci*., **25**, 280–292.

——, and L. A. Chang, 1972: On the application of satellite data on the cloud brightness to the study of tropical wave disturbances. *J. Atmos. Sci*., **29**, 1400-1403.

Weare, B. C, and J. S. Nasstrom, 1982: Examples of extended empirical orthogonal function analysis. *Mon. Wea. Rev.*, **110**, 481-485.

——, and AMIP Modeling Groups, 1996: Evaluation of the vertical structure of zonally averaged cloudiness and its variability in the Atmospheric Model intercomparison Project, *J. Climate*, **9**, 3419 –3431.

——, 2004: A comparison of AMIP II model cloud layer properties with ISCCP D2 estimates, *Climate Dyn*., **22**, 281– 292.

Webb, M., C. Senior, S. Bony, and J. J. Morcrette, 2001: Combining ERBE and ISCCP data to assess clouds in the Hadley Centre, ECMWF and LMD atmospheric climate models. *Climate Dyn*., **17**, 905–922.

Wendisch, M., P. Yang, and P. Pilewskie, 2007: Effects of ice crystal habit on thermal infrared radiative properties and forcing of cirrus, *J. Geophys. Res*., **112**, D08201, doi:08210.01029/02006JD007899.

Wheeler, M. C., and G. N. Kiladis, 1999: Convectively coupled equatorial waves: Analysis of cloud and temperature in the wavenumber-frequency domain. *J. Atmos. Sci*., **56**, 374-399.

Wiscombe, W. J., 1996: Mie scattering calculations: Advances in technique and fast, vector-speed computer codes., Technical Report Tech. Note. NCAR/TN-140+STR, NCAR.

Wylie, D. P., and W. P. Menzel, 1999: Eight years of high cloud statistics using HIRS. *J. Climate*, **12**, 170-184.

——, D. L. Jackson, W. P. Menzel, and J. J. Bates, 2005: Trends in global cloud cover in two decades of HIRS observations. *J. Climate*, **18**, 3021–3031.

Xu, K-M., T. Wong, B. A. Wielicki, L. Parker, Z. A. Eitzen, 2005: Statistical analyses of satellite cloud object data from CERES. Part I: Methodology and preliminary results of the 1998 El Niño/2000 La Niña. *J. Climate*, **18**, 2497–2514.

——, ——, ——, ——, B. Lin, Z. A. Eitzen, M. Branson, 2007: Statistical analyses of satellite cloud object data from CERES. Part II: Tropical convective cloud objects during

1998 El Niño and evidence for supporting the fixed anvil temperature hypothesis. *J. Climate*, **20**, 819–842.

Yanai, M., and T. Maruyama, 1966: Stratospheric wave disturbances propagating over the equatorial Pacific. *J. Meteor. Soc. Japan*, **44**, 291–294.

——, and M. Murakami, 1970: A further study of tropical wave disturbances by the use of spectrum analysis. *J. Meteor. Soc. Japan*, **48**, 185-197.

Yang, P., and K. N. Liou, 1998: Single scattering properties of complex ice crystals in terrestrial atmosphere, *Contrib. Atmos. Phys*., **71**, 223-248.

——, L. Zhang, G. Hong, S. L. Nasiri, B. A. Baum, H.-L. Huang, M. D. King and S. Platnick, 2007, Differences between Collection 004 and 005 MODIS ice cloud optical/microphysical products and their impact on radiative forcing simulations, *IEEE Trans. Geosci. Remote Sens*., **45**, 2886-2899.

——, and Q. Fu, 2009: Dependence of ice crystal optical properties on particle aspect ratio, *J. Quant. Spectrosc. Radiat. Transfer*, **110**, 1604-1614.

Zangvil, A., and M. Yanai, 1980: Upper tropospheric waves in the tropics. Part I: Dynamical analysis in the wavenumber-frequency domain, *J. Atmos. Sci*., **37**, 283-298.

Zelinka, M. D., and D. L. Hartmann, 2009: Response of humidity and clouds to tropical deep convection. *J. Climate*, **22**, 2389–2404.

——, and ——, 2010: Why is longwave cloud feedback positive? *J. Geophys. Res.*, **115**, D16117, doi:10.1029/2010JD013817.

Zhang, C., 2005: Madden–Julian oscillation. *Rev. Geophys.*, **43**, RG2003, doi:10.1029/2004RG000158.

Zhang, G. J., and N. A. McFarlane, 1995: Sensitivity of climate simulations to the parameterization of cumulus convection in the Canadian Climate Centre general circulation model. *Atmos.–Ocean*, **33**, 407–446.

Zhang, M., W. Lin, C. Bretherton, J. J. Hack, and P. J. Rasch, 2003: A modified formulation of fractional stratiform condensation rate in the NCAR Community Atmospheric Model (CAM2). *J. Geophys. Res*., **108**, 4035, doi:10.1029/2002JD002523.

——, ——, S. A. Klein, J. T. Bacmeister, S. Bony, and Coauthors, 2005: Comparing clouds and their seasonal variations in 10 atmospheric general circulation models with satellite measurements, *J. Geophys. Res*., **110**, D15S02, doi:10.1029/2004JD005021.

VITA

Yue Li received his Bachelor of Science degree in atmospheric science from Nanjing University, China in June 2005. He received his Master of Science degree in atmospheric science from Stony Brook University in August 2007. Yue Li entered the Ph.D. program in the Department of Atmospheric Sciences at Texas A&M University in September 2007, and received a Ph.D. degree in December 2011.

Yue Li may be reached at the Department of Atmospheric Sciences, Texas A&M University, 3150 TAMU, College Station, TX 77843-3150. His email address is yue.li@tamu.edu.

Peer-Reviewed Publications

Li, Y., G. R. North, P. Yang, and B. A. Baum, 2010: Exploration of the MODIS cloud-top property products for the investigation of equatorial wave system, *J. Appl. Meteor. Climatol.* **49**, 2050-2057.

Li, Y., P. Yang, G. R. North, and A. E. Dessler: Test of the fixed anvil temperature hypothesis, *Submitted to J. Atmos. Sci.*